INTEGRATED PARYLENE LC-ESI ON A CHIP

Thesis by

Jun Xie

In Partial Fulfillment of the Requirements

For the Degree of

Doctor of Philosophy

California Institute of Technology

Pasadena, CA 91125

2005

(Defended June 4, 2004)

To my parents and wife

ACKNOWLEDGEMENTS

My deepest gratitude goes to my advisor, Dr. Yu-Chong Tai. Six years ago, he gave me the opportunity to come to Caltech and work on the exciting field of MEMS. Without his constant guidance and valuable advice, I couldn't have accomplished my goals.

I am grateful to many previous members of our group: Fukang Jiang, Xuan-Qi Wang, Charles Grosjean, Shuyun Wu, Amish Desai, Wen Hsieh, Tze-Jung Yao, Ellis Meng. They helped me to start my research and taught me numerous lessons from their own experiences. I want to thank Xing Yang, in particular, for showing me the direction when I was at a crossroad and for being a mentor. Also Yong Xu and Zhigang Han, I enjoyed not only being their companion in the same office, but also the friendship outside work. They and their family made my life at Caltech easier and happier.

Only with the help of Prof. Terry Lee and Yunan Miao from City of Hope, I can fully demonstrate the true value of my work. The interdisciplinary collaboration with them broadened my knowledge and vision that could benefit me for years to come. Also Dr. Chi-Ming Ho and his students offered the key help to successfully complete the DARPA Bioflips program.

I am also thankful to all the current members in our group, especially Matthieu Liger, Justin Boland, Qing He, Ted Harder, Chi-Yuan Shih. Their assistance is highly appreciated. Qing He, his wife, and their cute daughters shared their happiness with me while, at same time, reminded me that it is about the time to start my own happy family.

The magic hands of Jason Shih made our devices come alive. His knowledge and skills proved to be critical for the success of all the projects we have been working together.

My work can not be completed without the help of our technician, Trevor Roper. The hands-on experience I learned from him is as important as the knowledge I got from books and courses. Thanks to Tanya Owen for keeping me away from the harassment of paperwork so I could be more focused.

Ever since I was still a young boy, my parents' vision for my life is the constant motivation for me. Over the years and through a lot of sacrifices, they laid the groundwork for me to reach where I am now. I hope I have realized their dream and made them proud. Finally, my wife. No words can describe what her love and support mean to me. She is always there for me.

ABSTRACT

Integrated Parylene LC-ESI on a Chip

Thesis by
Jun Xie

In Partial Fulfillment of the Requirements
For the Degree of
Doctor of Philosophy

In this thesis, several microfluidic devices will be introduced to demonstrate the integration capability of a multilayer parylene surface micromachining technology. Due to its flexibility and versatility, various devices have been developed and integrated onto a single ship. Based on the technology, on-chip LC-ESI was successfully demonstrated.

Based on the technology, an electrostatically actuated micro peristaltic pump has been developed. An AC actuation voltage combined with a peristaltic actuation was used to demonstrate fluid pumping. A reasonable flow rate and pumping pressure were achieved. The pump dynamics and performance were then addressed further by an analysis based on a lumped-parameter model of the system.

Based on the same technology, an entirely surface micromachined electrostatically actuated valve has been demonstrated. A thermal flow sensor was integrated with the valve to be used for feedback control. Two modes, actuation voltage

adjustment and PWM were investigated in characterizing the valve to control air flow. The testing results show that PWM has better linearity and performance.

Three types of capacitive fluidic sensors were demonstrated in several microfluidic applications. These include sensors for fluid pressure, flow rate, volume, and composition measurement. The sensors showed great promise for microfluidic applications because of their high sensitivity and easy integration capabilities. The integration of these sensors with abovementioned devices was achieved.

A novel electrochemical pumping system for on-chip LC gradient generation was demonstrated. This pump was able to deliver significant flow rates under high back pressures that are sufficient for many LC applications. On-chip gradient formation with integrated electrospray ionization was demonstrated.

Finally, a complete LC-ESI system was integrated in a chip format. Typical nano-LC reversed-phase gradient elution was demonstrated using on-chip electrolysis pump. Separated analytes from on-chip column were then sprayed into MS for analysis through an integrated ESI-nozzle. Separation results are comparable to those of commercial system. Peptide identification performance using the LC-ESI chip with MS was also very close to those achieved by the commercial system.

TABLE OF CONTENTS

LIST OF FIGURES

LIST OF TABLES

Chapter 1

Introduction

1.1 LC-ESI-MS FOR PROTEOMICS

1.1.1 Challenges in Proteomics

After Human Genome Project was officially completed in April 2003, the next big challenge is to understand of the structure and function of every protein that an organism can synthesize in its lifetime: its 'proteome'. The study of protein structure and function, known as proteomics, will be the research focus for decades to come and will help elucidate the fundamentals of life and the molecular basis of health and disease. Researchers all over the world already realized that the difficulties and challenges posed by proteomics far exceed those of genomics and could be an order of magnitude more complex. Following are a few reasons that will give some perspectives on the proteomic complexity.

Besides different biological properties, proteins also differ a lot in their physical and chemical properties. Chemical properties that distinguish the 20 different amino acids which are the building blocks for proteins cause the protein chains to fold up into specific three-dimensional structures that define their particular functions in the cell. Most proteins can only function properly when folding at the correct 3D structures. Proteins are

large and complex molecules with a very large range of their molecular weights. Proteins range considerably in size, from a few tens of amino acids (e.g. toxins, < 5 kDa) to several millions MDa (e.g. human titin, 26926 amino acids). They can also differ in the amount of electrical charges they carry under certain conditions. Their Isoelectric Point *pI* can be as low as 3 or as high as 11 [1]. Difference in their hydrophobicity can make some proteins only reside in watery environments such as blood, whereas others hide out in the fatty membranes surrounding cells.

The number of protein-coding genes in human is about 30,000, and each gene gives 5-10 different proteins through differential splicing and Post-Translational Modifications (PTM). Various Post-Translational Modifications (PTM) include phosphorylation, methylation, acylation, sulfation, etc. All these possibilities of PTM result in a constantly changing proteome and make the sequencing even more difficult. Today, the exact number of proteins existing in the human body is not known, although estimations range from ~300,000 to several millions [3].

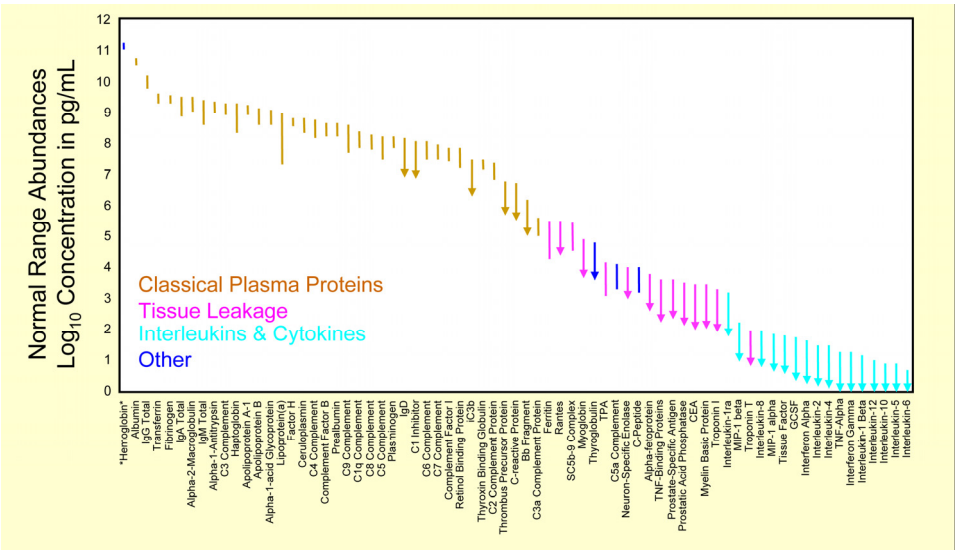

Figure 1-1 Dynamic range of concentrations of clinically measured proteins in plasma is > 10 orders of magnitude. [2]

The analytical instrumentation available can analyze only ~3-4 orders of magnitude of protein concentrations. That is nowhere near the real dynamic range observed in a living organism. For example, cellular proteins cover ~6 orders of magnitude and serum proteins >10 orders of magnitude [4, 5]. Most of the time, low-abundance proteins, which tend to have the most interesting and important functions in a cell, are drowned out by high-abundance proteins which can be present at 10,000 times the concentration [6]. Most challenging of all, while most proteins exist only in extremely small quantities, there is no protein equivalent of PCR, which would allow specific amplification of proteins in a sample This means that proteomic analyses are substrate-limited. Figure 1-1 lists concentrations of 70 clinically measured human plasma proteins. Overall these proteins exhibits a dynamic range > 10 orders of magnitude [2].

1.1.2 LC-ESI-MS for Proteomics

Figure 1-2 gives the popular tools that are currently applied in proteomics [3]. As can be seen in Figure 1-2, with the exception of protein microarray or chip technology,

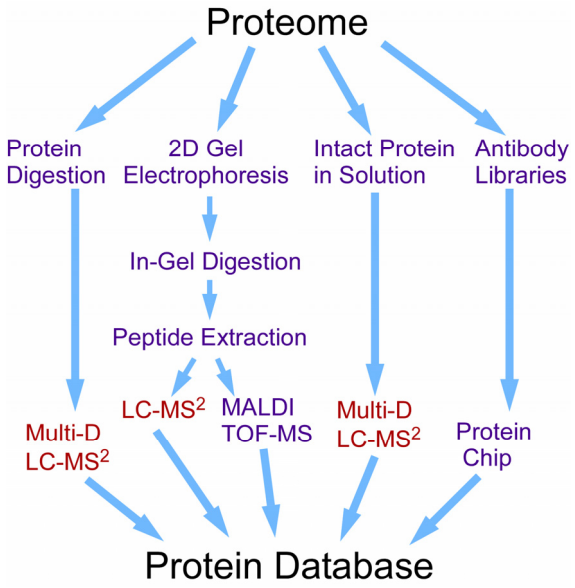

Figure 1-2 The current tools of proteomics [3].

approaches for analyzing complex protein mixtures mainly involve two steps: separation and identification. Sometimes the protein mixtures need to undergo digestion before or after separation as well.

Since the later 1980s, mass spectrometry (MS) has become the method of choice for analysis of complex protein samples [7, 8]. The breakthroughs which made possible MS-based proteomics were the discovery and development of the protein ionization methods: electrospray ionization (ESI) [9] and matrix-assisted laser desorption/ionization (MALDI) [10]. The scientific impact of these discoveries was recognized by the 2002 Nobel Prize in chemistry. Most of the approaches shown in Figure 1-2 utilize MS or MS^n as the final identification or detection instrumentation because it meets the basic requirements of proteomics [11]: wide dynamic-detection range, high resolution and sensitivity, high-throughput and high-confidence protein identification, and the ability to identify post-translational modifications, etc. Tandem MS or MS/MS can provide structural information on the proteins that can be isolated and fragmented through collision-induced dissociation (CID) within the MS instrument.

There are two separation methods that dominate in the proteomic landscape: 2D gel-electrophoresis (2D-GE) and multidimensional high-performance liquid chromatography (HPLC). Both of them have their own advantages and disadvantages, and are suitable for certain applications. The peptides or proteins that are separated by 2D-GE can be analyzed by MS through MALDI or ESI, but the transferring of the analytes is subject to extra intervention, and thus often is inconsistent, inefficient, and cannot provide accurate quantification. On the other hand, one very important advantage of HPLC compared to 2D-GE is the simple coupling to MS through ESI. When combined

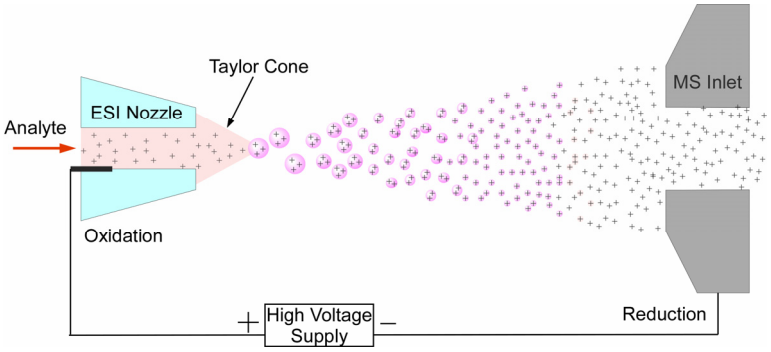

Figure 1-3 Principle of electrospray ionization.

together, LC^n-ESI-MS^n is a very powerful tool for analyzing complex protein/peptide mixtures. The following section will further show that the LC-ESI-MS combination is perfectly suitable for miniaturization.

1.2 MINIATURIZATION OF LC-ESI-MS

1.2.1 NanoESI

Electrospray ionization is an atmospheric pressure ionization source for mass spectrometry. Electrospray ionization refers to the overall process by which an intense electric field disperses a sample liquid into a bath gas as a fine spray of highly charged droplets [12]. Figure 1-3 illustrates the principle of ESI. It comprises a complex number of independent component processes, the two most important of which are electrospray dispersion, the electrostatic dispersion of sample liquid into charged droplets, and ionization, the transformation of solute species in those droplets to free ions in the gas phase.

Usually a high voltage source (1000s V) is applied between a very small nozzle and MS inlet. That will produce an intense electric field between them. Under the influence of the intense field at the nozzle tip, the emerging liquid forms a so-called ‘Taylor cone’.

The intense field induces a charge accumulation at the liquid surface of the Taylor cone. Once the electrostatic force overcomes the liquid surface tension, tiny charged droplets will form at the tip of the Taylor cone and are expelled towards the MS inlet. During the flight path to the MS, the solvent contained in the droplet evaporates. When the droplets shrink to the point where the repelling coulombic forces are larger than their cohesive forces, the so-called coulomb explosion will occur and the droplets will divide. The droplets will undergo a cascade of these divisions, yielding smaller and smaller droplets and eventually individual ions. The exact mechanisms of electrospray ionization are still not well understood.

ESI-MS measurements are concentration sensitive detection. There is almost no loss in S/N ratio when the flow rate is reduced as illustrated in Figure 1-4. The overall efficiency in electrospray mass spectrometry is defined as the total number of analyte ions detected divided by the total number of analyte molecules sprayed. It is a combination of desolvation, ionization, and transfer efficiencies in the vacuum system of MS [13]. The size of the nozzle and the flow rate at which ESI operates are becoming smaller and smaller, and all these three efficiencies are enhanced by these changes.

Nozzles with an inner diameter of around a few microns are commercially available. One of the reasons for that is in general, the smaller the nozzle, the better it can

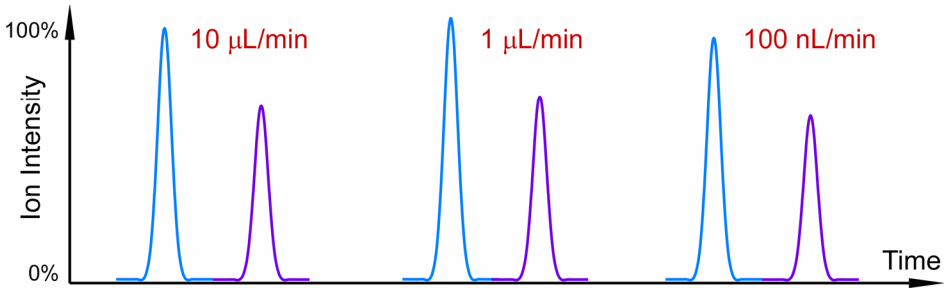

Figure 1-4 Electrospray ionization is concentration sensitive. The intensities of two ion peaks stay almost the same as the flow rate is reduced by 100 times.

concentrate the electric field at tip of the nozzle. Nanoelectrospary has become a well-accepted name for ESI that operates at a flow rate of 1 to 100s nL/min. As the flow rate decreases, the droplets that are emitted from the tip of a stable Taylor cone will be smaller. The model presented in [14] predicts proportionality between the two-thirds power of the flow rate and the size of droplets. When the flow rate goes down to 20 nL/min, the predicted droplet diameter is less than 200 nm. Both the desolvation efficiency and ionization efficiency can benefit from the reduced-diameter and monodisperse droplets. Transfer efficiency is improved by the reduced flow rate because of the close placement of the nozzle to the MS inlet; allowing a higher percentage of ions transferred to the MS analyzer section instead of the vacuum pumping system. There has been a reported 2 orders of magnitude gain in the overall efficiency that mirrors the almost 2 orders of magnitude lower flow rate of nanoelectrospray over conventional sources [13]. Attomole [15, 16] and zeptomole [17] protein analyses have been successfully demonstrated using nanoESI-MS.

Various MEMS technologies have been used to build nanoESI nozzles. For example, silicon-based nozzles that are fabricated by DRIE are commercially available from Advion Biosciences. Polyimide nozzles made by laser ablation have been under development for years at Agilent. Many other materials, such as SU-8 and PDMS, have been used. Nozzles made from parylene technology [18] clearly have many advantages over other materials and technology. First, it is a much more reliable and chemically inert material compared to SU-8 and PDMS. Second, the fabrication technology is suitable for mass production with very precise dimensional control, compared to time-consuming or expensive laser ablation and DRIE.

1.2.2 NanoLC

In recent years, miniaturization of liquid chromatography has drawn a lot of attention. The motivations behind this development are low sample consumption, fast analysis time, high-throughput, and high performance [19]. Small sample volume is often desirable because of the cost of chemicals or the limited clinical sampling. Fast analysis time is very important in high-throughput screening or point-of-care diagnosis, and can be achieved in miniaturized systems because of the reduction in diffusion time and parallel processing (e.g. microarray or CD-like platform). One of the most important measures of performance of a liquid chromatography system is the sensitivity or limit of detection (LOD). Many works have shown that miniaturization of LC system can result in a great increase of both mass and concentration sensitivity.

Table 1-1 gives a classification of LC columns by column internal diameter [20]. Capillary LC with column diameters of around 100 μm has gained more acceptance as routine analytical tools in many applications, especially protein/peptide separations. Nano-LC with column diameters less than 100 μm and flow rates less than 1 μL/min, when coupled with ESI-MS, theoretically allows a great increase of the mass and concentration sensitivity [21].

Compared with conventional LC techniques, in nano-LC, all volumes mush be

Table 1-1 LC Classifications

Name	Column Diameter	Typical Flow Rate
Conventional:		
Wide-bore (preparative)	> 4.6 mm	> 3 mL/min
Normal-bore (analytical)	3-4.6 mm	0.5-3 mL/min
Narrow Bore	1-2 mm	0.02-0.3 mL/min
Capillary:		
Microbore	150-800 μm	2-20 μL/min
Nanobore	20-100 μm	0.1-1 μL/min

down-scaled by a scaling factor f which is defined as

$$f = \frac{d_{conv}^2}{d_{nano}^2} \tag{1.1}$$

where d_{conv} and d_{nano} are the diameters of the conventional and nanoscale HPLC columns. The volumetric flow rate F is given by

$$F = u\pi d_c^2 \varepsilon / 4 \tag{1.2}$$

where u is the linear velocity of the mobile phase, d_c the column diameter, and ε the column porosity. Typically, ε is around 0.7, and the optimal linear flow velocity of the mobile phase in the column u can be determined by van Deemter curve, and it is usually around 1 mm/s. For a 50-µm i.d. column, the optimal flow rate is around 85 nL/min.

If all the other parameters (e.g. column length, packing, etc.) are the same, for a given injected sample mass, the sample concentration of a peak eluted from the column is inversely proportional to the flow rate:

$$\frac{C_{nano}^2}{C_{conv}^2} = \frac{F_{conv}^2}{d_{nano}^2} = \frac{d_{conv}^2}{d_{nano}^2} = f \tag{1.3}$$

Based on Equation (1.3), it can be seen that when the column diameter is reduced from 4.6 mm to 50 µm, there is corresponding concentration increase of 8464 times. Figure 1-5 illustrates the relationship between the flow rate and the eluted sample concentration.

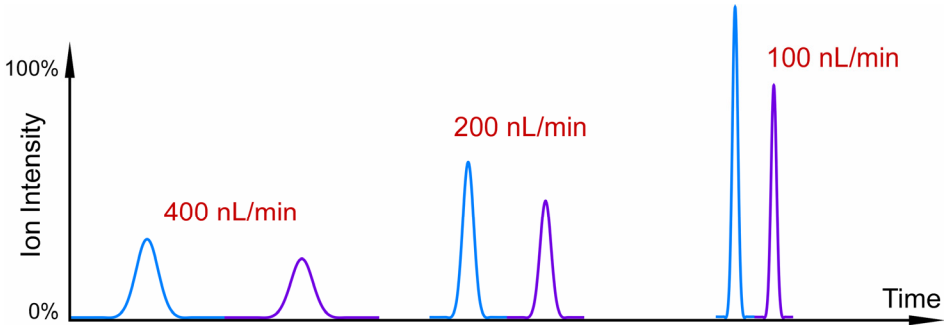

Figure 1-5 The relationship between the flow rate and the eluted sample concentration.

Higher sample peaks eluted from the column mean higher sensitivity, but only if the detector can take the advantage of this concentration increase. Many works have shown that LC-ESI-MS configuration can really benefit from the reduced flow rate and this is one of the fundamental reasons that why doing nanoLC-nanoESI is a popular trend in analytical chemistry, especially in protein/peptide profiling or sequencing.

1.3 INTEGRATION IN MICROFLUIDICS

More than a decade has passed since the establishment of the micro total analysis systems (μTAS) field. Many devices and systems have been developed and demonstrated using a variety of technology. However, people gradually realized that total integration or large-scale integration (LSI) is an unavoidable trend in μTAS. μTAS can have integrated multi-functions in the system, achieve high-throughput and automation, reduce the cost of operation and packaging, and ultimately fulfill the original goals or motivations that gave the birth to the field in the first place.

One of the biggest challenges for total integration and large-scale integration is the incompatibility among different fabrication technologies. Most of the time, multi-chip packaging and complex interconnection, whether from chip-to-chip or chip-to-world, are required. These will drive up the cost and the scale of integration, because the packaging and interconnection are often labor intensive, low yield and not suitable for mass production.

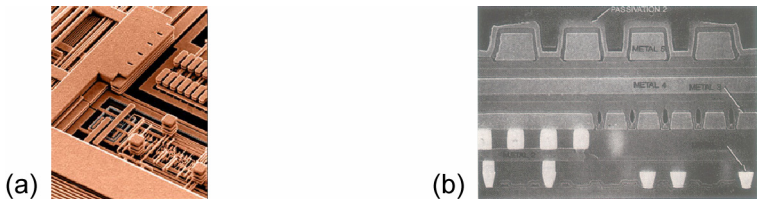

Figure 1-6 Multilayer interconnection technology in the IBM microprocessor.

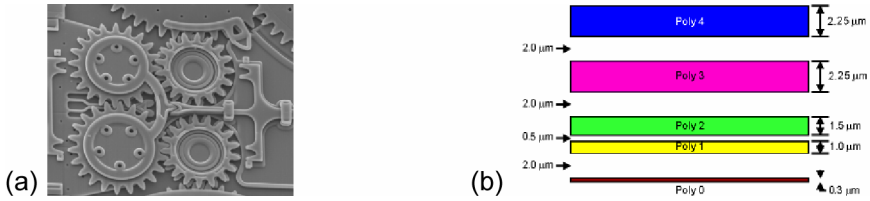

Figure 1-7 Sandia national lab's multilayer surface micromachined polysilicon technology (SUMMIT™). (a) A gear box example. (b) Schematic of the process.

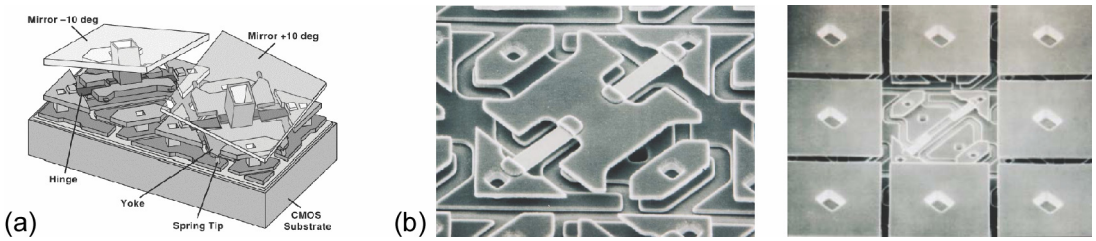

Figure 1-8 TI's surface micromachined multilayer DMD. (a) Schematic of the device. (b) SEM picture of the fabricated devices.

One approach that was the key in the success of VLSI in the IC industry was the development of a multilayer technology. Shown in Figure 1-6, the multilayer copper interconnection technology from IBM is a good example. Similar approaches for integration have also been explored in the MEMS field. The Sandia National Lab's ultra-planar, multi-level MEMS technology (SUMMIT™ V) shown in Figure 1-7 utilizes 5 layer of polysilicon as the structural material. Another successful example of surface micromachined multilayer device, as shown in Figure 1-8 is TI's Digital Mirror Device (DMD) that has been used in millions of projection systems. In TI's DMD system, the multilayer surface micromachining technology enables the integration of millions of tiny

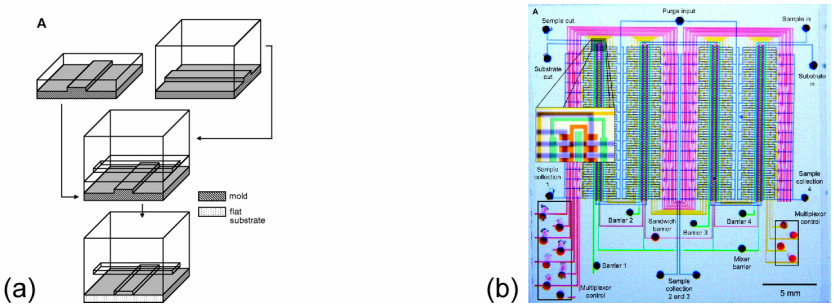

Figure 1-9 Large-scale integration by multilayer soft lithography. (a) MSL fabrication process [22]. (b) An integrated chip with 256 individually addressable reaction chambers [23].

mirrors that can be addressed like RAM on a single chip. Clearly, similar multilayer approaches should be considered as a promising candidate for total integration or LSI in microfluidics.

The most prominent technology for microfluidic integration is the multilayer soft lithography technology (MSL) that has been developed based on PDMS molding and packaging [22]. This technology has demonstrated a tremendous capability for large-scale integration [23] that can be seen in Figure 1-9. However, the technology has some limitations. Fluidic sensors, such as flow sensor and pressure sensor, have not been developed using the same fabrication process. Also, actuation of the on-chip valves and pumps still relies on off-chip pneumatic control which requires complex pneumatic connections to the chip. The structural material, PDMS, is not chemical resistant enough for chemical analysis systems that have strong organic solvents (e.g. acetone), acids, and bases, although a lot of works have been done to improve the properties of PDMS. The microfluidic devices made by MSL are suitable for certain applications, but alternative technologies definitely need to be developed.

In order to eliminate the need of multi-chip packaging, the alternative technology is preferably surface micromachined, so that various devices can be integrated on the single

chip. On-chip sensors and actuations are also necessary for a complete, autonomous, and standalone system. Off-chip fluidic connections or interfacing should be kept to a minimum since it is generally more difficult to provide fluidic connections to the chip than electrical connections. The technology has to be versatile and flexible so that various microfluidic components can be realized on a single chip using one process.

1.4 MULTILAYER PARYLENE TECHNOLOGY

For the past few years, the Caltech MEMS group has been working a polymeric material called parylene. A lot of MEMS and microfluidic devices have been realized using parylene as a structural material. The developed multilayer parylene surface micromachining technology has gradually increased in complexity and sophistication [24]. The works presented later in this thesis are the latest development of multilayer parylene surface micromachining technology.

Parylene, poly (para-xylylene), is the generic name for a unique family of thermoplastic polymers that are deposited by using the dimmer of para-xylylene. Parylene deposition is basically a room temperature chemical vapor deposition (CVD). Because the deposition pressure is around 10 mtorr, the deposition is conformal which means step coverage is excellent. Since parylene is an organic polymeric material, oxygen plasma is used to etch it using photoresist or metal as the masks. Generally, parylene processes are done at temperatures lower than 120 °C, so this enables the post-CMOS fabrication capability which is very valuable to integrate circuits with microfluidic devices.

Table 1-2 Parylene properties.

Property	Parylene N	Parylene C	Parylene D
Electrical:			
Dielectric Strength (V/μm)	275	220	220
Dielectric Constant (at 60Hz)	2.65	3.15	2.84
Volume Resistivity (Ω·cm)	1.4×10^{17}	8.8×10^{16}	1.2×10^{17}
Mechanical:			
Young's Modulus (GPa)	2.42	2.76	2.62
Yield Strength (MPa)	42	55	62
Density (g/cm^3)	1.1	1.3	1.4
Rockwell Hardness	R85	R80	R80
Optical:			
Index of Refraction	1.66	1.64	1.67
Strong UV Absorption (nm)	280	280	
Thermal:			
Melting Point (°C)	420	290	380
T5 Point (modulus=700MPa)	160	125	125
Linear Coef. of Expan. (ppm/°C)	69	35	30-80
Thermal Conductivity (mW/(cm·K))	1.26	0.84	
Specific Heat (cal/(g·°C))	0.20	0.17	

Details of the properties of parylene can be found on the website of Specialty Coating Systems. Table 1-2 gives some properties of parylene.

Here are some most important properties that make parylene an excellent choice for microfluidic applications. Parylene is a good electrical insulator and 1 μm parylene-C can withstand more than 200 V before breakdown. The Young's modulus of parylene is in between silicon and PDMS which can make it a perfect choice for making flexible structure in microfluidic actuator.

Parylene is transparent in the visible light range. Unfortunately, parylene absorbs for wavelengths below 280 nm. This limits its application in making UV detection cell or channel.

Parylene has a large linear coefficient of thermal expansion compared to silicon and oxide, which can result in a film with tensile stress. This requires special attention during

fabrication since the thermal stress is greatly affected by the thermal history of the film. Thermal conductivity is one order of magnitude smaller than oxide and that makes it a very good thermal isolation materials.

Parylene is an excellent barrier to gas and moisture, so it is frequently used in the electronic packaging. Gas permeability of parylene is at least 4 orders of magnitude smaller than PDMS. Moisture vapor transmission is also 10 times better than silicones.

In biological or chemical analysis or processing systems, chemical resistance is a desired material property. Parylene is stable in most strong acids, bases and organic solvents. It is also a biocompatible material that is qualified as USP Class VI material which means it can be used in implant devices.

1.5 CONCLUSIONS

In the following chapters, several microfluidic devices will be introduced to demonstrate the capability of the multilayer parylene surface micromachining technology. Due to its flexibility, various devices can be integrated onto a single ship. Based partially on the technology, a complete on-chip LC-ESI system is also demonstrated.

REFERENCES:

[1] N. Lion, T. C. Rohner, L. Dayon, I. L. Arnaud, E. Damoc, N. Youhnovski, Z. Y. Wu, C. Roussel, J. Josserand, H. Jensen, J. S. Rossier, M. Przybylski, and H. H. Girault, "Microfluidic systems in proteomics," *Electrophoresis*, vol. 24, pp. 3533-3562, 2003.

[2] N. L. Anderson and N. G. Anderson, "The human plasma proteome - History, character, and diagnostic prospects," *Molecular & Cellular Proteomics*, vol. 1, pp. 845-867, 2002.

[3] T. Laurell and G. Marko-Varga, "Miniaturisation is mandatory unravelling the human proteome," *Proteomics*, vol. 2, pp. 345-351, 2002.

[4] S. D. Patterson, "Data analysis - the Achilles heel of proteomics," *Nature Biotechnology*, vol. 21, pp. 221-222, 2003.

[5] G. L. Corthals, V. C. Wasinger, D. F. Hochstrasser, and J. C. Sanchez, "The dynamic range of protein expression: A challenge for proteomic research," *Electrophoresis*, vol. 21, pp. 1104-1115, 2000.
[6] A. Abbott, "A post-genomic challenge: learning to read patterns of protein synthesis," *Nature*, vol. 402, pp. 715-720, 1999.
[7] R. Aebersold and M. Mann, "Mass spectrometry-based proteomics," *Nature*, vol. 422, pp. 198-207, 2003.
[8] E. d. Hoffmann and V. Stroobant, *Mass spectrometry : principles and applications*, 2nd ed. Chichester ; New York: Wiley, 2001.
[9] J. Fenn, M. Mann, C. Meng, S. Wong, and C. Whitehouse, "Electrospray Ionization for Mass-Spectrometry of Large Biomolecules," in *Science*, vol. 246, 1989, pp. 64-71.
[10] M. Karas and F. Hillenkamp, "Laser Desorption Ionization of Proteins with Molecular Masses Exceeding 10000 Daltons," *Analytical Chemistry*, vol. 60, pp. 2299-2301, 1988.
[11] P. James, *Proteome research : mass spectrometry*. Berlin ; New York: Springer, 2001.
[12] J. F. de la Mora, G. J. Van Berkel, C. G. Enke, R. B. Cole, M. Martinez-Sanchez, and J. B. Fenn, "Electrochemical processes in electrospray ionization mass spectrometry - Discussion," *Journal of Mass Spectrometry*, vol. 35, pp. 939-952, 2000.
[13] M. Wilm and M. Mann, "Analytical properties of the nanoelectrospray ion source," *Analytical Chemistry*, vol. 68, pp. 1-8, 1996.
[14] M. S. Wilm and M. Mann, "Electrospray and Taylor-Cone Theory, Doles Beam of Macromolecules at Last," *International Journal of Mass Spectrometry and Ion Processes*, vol. 136, pp. 167-180, 1994.
[15] G. A. Valaskovic, N. L. Kelleher, D. P. Little, D. J. Aaserud, and F. W. Mclafferty, "Attomole-Sensitivity Electrospray Source for Large-Molecule Mass-Spectrometry," *Analytical Chemistry*, vol. 67, pp. 3802-3805, 1995.
[16] G. A. Valaskovic, N. L. Kelleher, and F. W. McLafferty, "Attomole Protein Characterization by Capillary Electrophoresis-Mass Spectrometry," *Science*, vol. 273, pp. 1199-1202, 1996.
[17] M. E. Belov, M. V. Gorshkov, H. R. Udseth, G. A. Anderson, and R. D. Smith, "Zeptomole-sensitivity electrospray ionization - Fourier transform ion cyclotron resonance mass spectrometry of proteins," *Analytical Chemistry*, vol. 72, pp. 2271-2279, 2000.
[18] L. Licklider, X. Q. Wang, A. Desai, Y. C. Tai, and T. D. Lee, "A micromachined chip-based electrospray source for mass spectrometry," *Analytical Chemistry*, vol. 72, pp. 367-375, 2000.
[19] N. Lion, F. Reymond, H. H. Girault, and J. S. Rossier, "Why the move to microfluidics for protein analysis?," *Current Opinion in Biotechnology*, vol. 15, pp. 31-37, 2004.
[20] J. Abian, A. J. Oosterkamp, and E. Gelpi, "Comparison of conventional, narrow-bore and capillary liquid chromatography mass spectrometry for electrospray ionization mass spectrometry: Practical considerations," *Journal of Mass Spectrometry*, vol. 34, pp. 244-254, 1999.

[21] J. P. Chervet, M. Ursem, and J. B. Salzmann, "Instrumental requirements for nanoscale liquid chromatography," *Analytical Chemistry*, vol. 68, pp. 1507-1512, 1996.
[22] M. A. Unger, H. P. Chou, T. Thorsen, A. Scherer, and S. R. Quake, "Monolithic microfabricated valves and pumps by multilayer soft lithography," *Science*, vol. 288, pp. 113-116, 2000.
[23] T. Thorsen, S. J. Maerkl, and S. R. Quake, "Microfluidic large-scale integration," *Science*, vol. 298, pp. 580-584, 2002.
[24] X.-Q. Wang and Y.-C. Tai, "A normally closed in-channel micro check valve," presented at The 13th Annual International Conference on Micro Electro Mechanical Systems (MEMS 2000), 2000.

.

Chapter 2

Surface-Micromachined Electrostatically Actuated Micro Peristaltic Pump

2.1 INTRODUCTION

Recently there has been an increase of interest in the research and development of microfluidics because of the escalating demands of genomics [1], proteomics [2], drug discovery, and lab automation. The micro pump is at the heart of the micro total analysis system (μTAS). It provides the driving force to mobilize fluid in the system, in order to realize desired functions such as mixing, injection, and separation, etc. Previously, many micro pumps have been demonstrated using several different actuation mechanisms and fabrication technologies [3]. Unfortunately, most of them have inherent limitations that prevent them from achieving the large-scale integration that is essential for μTAS.

Pumps can be divided into two major categories: mechanical pumps and non-mechanical pumps. In general, because non-mechanical pumps are realized using simple structures and no moving parts, they are straightforward in terms of fabrication and well suited for integration, but performance often greatly depends on the properties of the fluid being pumped. For example, electroosmotic pumping can be affected by the electrical properties [4] of the fluid, such as permittivity, zeta potential, etc. Similarly, electrohydrodynamic pumps are directly affected by the conductivity of the fluid [5].

Also, fluid transfer based on principles such as electrowetting, are highly dependent on the fluid's surface tension.

While mechanical pumps offer more flexibility on the fluid that can be pumped, complicated structures are challenging to scale down and fabricate for integration. This issue is especially evident in rotary pumps and pumps that require check valves. Compared to other mechanical pumps, peristaltic pumps have a relatively simple structure and hence scale down favorably.

Among the actuation methods that have been utilized in micro peristaltic pumps, electrostatic actuation presents some advantages over other actuation methods. It consumes much less power than thermopneumatic actuation while still delivering reasonable pumping rates and pressures. Since most microfluidic systems are targeted at biological applications, low power and low temperature have clear advantages. Compared to piezoelectric actuation, electrostatic actuation also gives more displacement without the complicated fabrication associated with processing piezoelectric materials, leading to a higher compression ratio. Instances of electrostatic actuated pumps include an electrostatic mesopump using plastic molding technology has been reported [6] and a surface micromachined electrostatic peristaltic pump has also been reported but without any testing results [7], where no actual testing results were reported. This work is the first entirely surface micromachined electrostatically actuated peristaltic pump. Its realization is enabled by a multilayer parylene surface micromachining technology that we have developed over the last few years [8].

The motivation for the development of this surface micromachining technology was to have a versatile and flexible technology that can be used to build various fluidic

devices on a single chip, using a single technology. Incompatibility between different fabrication technologies can be eliminated with this approach. At the same time, precise alignment and reliable packaging, problems associated with multi-chip solutions can also be avoided. A multilayer PDMS based microfluidic system that allows rapid prototyping [9] and large scale integration [10] has been demonstrated. However, this type of system still requires off-chip pneumatic control, which could potentially limit the miniaturization of the system and its application in portable devices. This problem can be overcome with this demonstrated parylene technology, since electrostatic actuation circuits can be highly miniaturized.

A lumped-parameter model to understand the operation of the surface-micromachined peristaltic pump is also presented here. The dynamics of peristaltic pumping, not addressed by existing micro pump models [11-13], are carefully investigated. The dynamics of individual pumping chambers are considered and account for the interactions of such component dynamics by a system representation of the peristaltic pump. The resulting model can be used to quantitatively determine important pumping characteristics such as the flow rate and pumping pressure. The model reveals the general trend in the experimentally observed pump characteristics.

2.2 DESIGN

A schematic of the mechanical structure and operation principle of the micro pump is given by Figure 2-1. Because the micro pump is based on a surface micromachining technology, its basic design is chosen to be a membrane pump. It has three pumping chambers connected in series. Essential components of each pumping chamber include an actuation chamber, a fluid channel, and a moving membrane that separates them. The

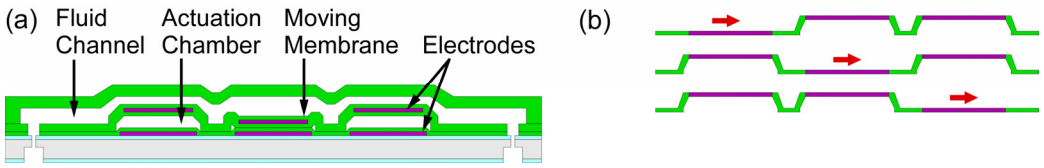

Figure 2-1 Schematic of the design and operation of the micro pump. (a) Structure design of the micro pump. (b) 3-phase peristaltic actuation sequence. Arrow indicates pumping direction.

actuation chamber is vented to the outside ambient through a venting hole. A fixed ground electrode is located on the substrate at the bottom of the actuation chamber and coated with Parylene to isolate it from the environment. A top electrode is incorporated into the moving membrane and is sandwiched between two Parylene layers. Together, this composite structure forms the moving membrane. On top of the moving membrane, the fluid channel is created which runs through all three pumping chambers. When an actuation voltage is applied between the two electrodes, an electrostatic force will pull down the membrane and cause a volume expansion in the fluid channel on top. When the three pumping chambers are actuated using the 3-phase peristaltic sequence [14], the peristaltic motion will induce pumping of the fluid inside the channel.

A key feature of this design is that the electric field is confined inside the actuation chamber, which is filled with air, so it is separated from the liquid filled fluid channel. This pump design is advantageous in applications involving biological substances or chemical reagents, such as proteins and cells, which could be affected by the high electric field.

Electrostatic pull-in is a well-known instability in the behavior of an elastically supported parallel-plate electrostatic actuator. To achieve maximum volume compression/expansion ratio, the pump needs to operate around the pull-in mode so the membrane deflection can be at a maximum. We adopted a closed-form quantitative model [15] for the pull-in voltage of clamped circular diaphragms, which is approximately the case for the moving membrane. The model accounts for contributions

Table 2-1 The symbols and parameters used in the analysis.

Definition	**Symbol** (Value)
Constant or Material Property	
Permittivity of Free Space	ε_0
Viscosity of Liquid (Water or Ethanol)	μ
Dielectric Constant of Parylene	ε_p (3.1)
Density of Parylene	ρ (1.3 g/cm^3)
Poisson Ratio	ν (0.4)
Young's Modulus	E (3.2 GPa)
Residual Stress of Parylene Membrane	σ (20 MPa)
Model Parameters	
Thickness of Actuation Membrane	t_m (2 μm)
Thickness of Insulation Layer	t_i (2 μm)
Radius of Actuation Membrane	r (100 μm)
Height of Actuation Gap	d (3 μm)
Thickness of Fluid Film on Top	h (1 μm)
Effective Mass of Plate (Membrane)	M
Effective Stiffness of Plate (Membrane)	K
Area of Membrane	A
Pumping Load	R_L
Height of Load Channel	H (5 μm)
Width of Load Channel	W (100 μm)
Length of Load Channel	L (24 mm)
Electrostatic Pull-in Voltage	V_p
Applied Voltage	V or V_i
Plate Displacement	δ or δ_i
Electrostatic Force on Membrane	F_e
Hydrodynamic Force	F_h
Pressure up/downstream of Chamber	$p_{a,b}$ or p_i
Flow Rate in/out of Chamber	$q_{a,b}$ or q_i
Time	t
Period of Entire 3-Phase Cycle	T

of both bending stiffness and residual membrane stress to the overall membrane stiffness. The parylene insulation layers are also taken into account. Then, the equation for the pull-in voltage V_p becomes

$$V_P = \sqrt{\frac{1.55\sigma t_m (d + t_i/\varepsilon_p)^3}{\alpha \varepsilon_0 r^2}} \tag{2.1}$$

where α can be expressed as

$$\alpha = 1 + 2\frac{(1-\cosh\kappa)}{(\kappa \sinh\kappa)} \tag{2.2}$$

and κ is

$$\kappa = \frac{1.65r}{2t_m}\sqrt{\frac{12(1-\nu^2)\sigma}{E}} \tag{2.3}$$

where σ, E and ν are the residual stress, Young's modulus and Poisson's ratio of parylene, r and t_m are the membrane radius and thickness, d is the initial electrode gap thickness, t_i and ε_p are the thickness and relative permittivity of the parylene insulation layers between the electrodes, and ε_0 is the perimittivity of free space. The effect of parylene insulation layers is translated to an equivalent air gap with a thickness of t_i/ε_p and added to d. This equation is the basis on which we designed most physical dimensions of the micro pump. In choosing the parameters, many fabrication constraints have to be considered. Previous studies have shown that the electric field strength at which breakdown occurs in parylene is around 250 V/μm [16]. In order to achieve good electrical isolation and barrier against liquid or moisture around the electrodes, 1-μm parylene is considered necessary. Although thicker parylene increases the isolation, it also increases stiffness and results in unnecessary energy loss during actuation. For the composite moving membrane, two 1-μm parylene layers were chosen which means t_m

equals to 2 μm. t_i is also 2 μm because of the two 1-μm insulation layers between the two electrodes.

For safety and power consumption reasons, V_p should be minimized. A high actuation voltage also makes the pump prone to electrolysis because of current leakage through the parylene insulation layers. Based on Equation (2.1), to reduce the pull-in voltage, the height of the actuation gap d should be kept small, but a small actuation gap leads to a reduced volume expansion (approximately $(d+h)/h$), which will cause the pumping rate to be small. Moreover, stiction becomes a serious problem when the gap between two surfaces is too small. This can be explained by noting that, during drying, the surface tension force at the liquid/air interface indeed creates a differential pressure across the interface which then translates to the pressure drop on the flexible membrane. This pressure drop ΔP is given by Equation (2.4)[17]:

$$\Delta P = \frac{2\gamma \cos\theta}{d} \tag{2.4}$$

where γ is the surface tension and θ is the contact angle. The pressure drop is inversely proportional to the height of the channel gap. This stiction problem is addressed in detail in a later section.

Based on these considerations, d was designed to be around 3 μm. Since V_p is inversely proportional to r, a larger membrane offers a lower V_p, but this larger membrane is also more easily affected by stiction. Test structures were fabricated to determine the optimal value for r. The results will be presented in a later section. In the final fabricated micro pump, r is chosen to be 100 μm so V_p can be lower than 200 V. The fluid channel height h on top of the actuation membrane is related to compression/expansion ratio. While considering the capabilities of the sacrificial

photoresist process, *h* was designed to be around 1 μm to maximize the ratio. Channels that are connected to the pump have a typical cross section of 100 μm (W) × 5 μm (H).

2.3 FABRICATION

2.3.1 Fabrication Process

The fabrication process of the micro pump is shown in Figure 2-2. Four layers of Parylene were used as the mechanical material, photoresist and sputtered Si as the sacrificial materials, and chrome/gold as the electrode material.

To start, 1.5 μm thermal silicon oxide was grown on 4-inch silicon wafer with double-side alignment marks. The backside oxide was patterned using a 10 μm photoresist layer, and together they served as the mask for DRIE etching of the inlets and outlets for the fluidic channels. A standard Bosch DRIE process was used, and etching commenced until a 50 μm thick silicon membrane was left. The main purpose of the inlet and outlet are to provide access to the pump for characterization work. So they are not an essential part of the micro pump.

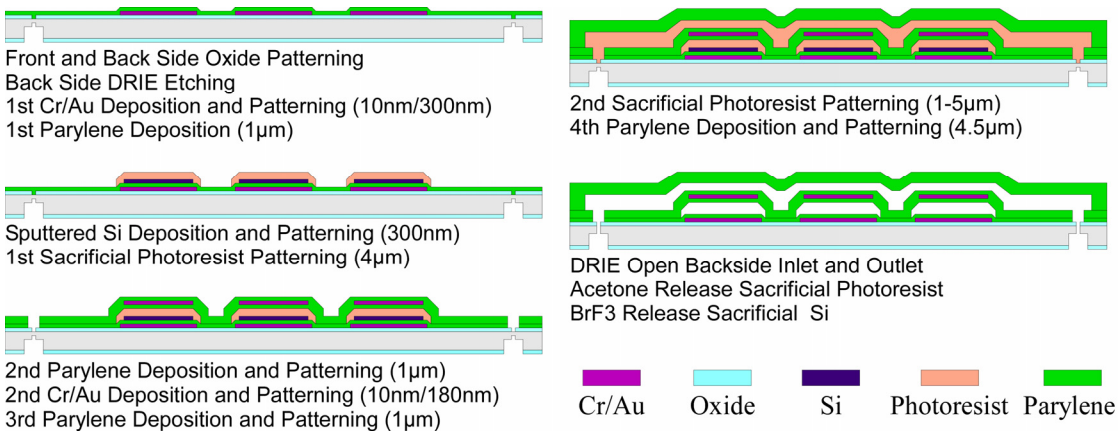

Figure 2-2 Multilayer parylene technology used in the fabrication process of the micro pump: 4 layers of parylene (structural); 2 layers of photoresist and 1 layer of sputtered Si (sacrificial); and 2 layers of Cr/Au (electrode).

The process was continued on the front side. The front side oxide was patterned to expose the inlet and outlet for the fluidic channels that were formed later in the process. After the wafers were cleaned in Piranha, a Cr/Au (10 nm/300 nm) layer was thermally evaporated and then patterned on the front side to form the bottom electrode. After the surface was cleaned using oxygen plasma, adhesion promoter A-174 from SCS was applied to the surface to ensure good adhesion between the Parylene and the substrate. To isolate the bottom electrode from the environment, a 1 μm parylene-C was then deposited using room temperature chemical vapor deposition (CVD). Next, a 300 nm sacrificial amorphous silicon layer was sputtered on the fresh parylene surface that had been roughened by a short oxygen plasma treatment. The amorphous silicon was patterned by using SF6 chemistry and photoresist as the mask. The reason of having this extra sacrificial layer is given later in the section. On top of the amorphous silicon layer, the first photoresist sacrificial layer (4 μm) was formed and patterned. The combination of the amorphous silicon and the first photoresist sacrificial layer together define the actuation gap. Next, the moving actuation diaphragm, consisting of a parylene/metal/parylene sandwich structure, was created. To do this, a second 1 μm parylene-C layer was deposited and patterned; the top electrode layer was formed by another evaporated Cr/Au (10 nm/180 nm) layer; and a third 1 μm parylene-C layer was deposited to encapsulate the top electrode. This encapsulation insured that the electrode was isolated from the liquid filled fluid channel. Patterning of the parylene was done using oxygen plasma with photoresist or Al as a mask. Once the moving membrane was finished, the fluid channel was formed by a second photoresist sacrificial layer and a 4.5 μm fourth parylene-C layer. The height of the fluid channel, as determined by the

thickness of the second photoresist sacrificial layer, varied as a result of the uneven step coverage of photoresist over the existing structures. A partial double exposure was carefully performed to reduce the channel height immediately above the actuation chamber as required by the design specifications.

The process resumed on the backside. The remaining 50 μm silicon membrane was etched away using DRIE to fully open the inlet and outlet of the fluid channel. Finally, the sacrificial photoresist was released using acetone. After releasing, the chips were rinsed with isopropanol rinse and allowed to dry.

Some process steps need special attention. To ensure sufficient adhesion of the parylene, before its deposition, either adhesion promoter or several cleaning steps, such as a short period O_2 plasma etching or a 5% HF dip for up to 30 seconds, were performed whenever necessary.

2.3.2 Stiction Problem

Stiction can happen during the drying process after the photoresist is dissolved away, especially if the membrane is thin or large. To solve the stiction problem and produce a freestanding membrane, two methods were tried and compared.

First, CO_2 supercritical point drying (SPD) was tested on several testing structures. As expected, large diameter membranes (~400 μm), are likely to have stiction during drying after photoresist releasing. On the other hand, SPD can produce a freestanding membrane. Figure 2-3 shows the comparison. The testing structures used in the SPD testing consist of the same structure as the pumping chamber but without the top fluid channel and amorphous silicon layer. Before SPD, the testing structures were submerged

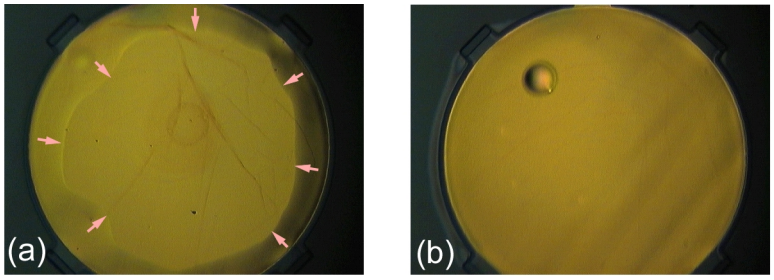

Figure 2-3 The effect of CO_2 supercritical point drying. (a) is a membrane that went through normal drying process. Arrows point to the boundary of the stiction. (b) is a freestanding membrane released by SPD. The membrane is 400 μm in diameter and 2 μm thick.

in methanol for several hours to replace the IPA or acetone that had been used to dissolve the photoresist.

However, SPD caused very serious delamination problems when adhesion between the multiple parylene layers was insufficient. This problem can be clearly seen in Figure 2-4. Figure 2-4 also indicates that the choice of solvent used in the SPD had an effect on the delamination too. One hypothesis for this phenomenon is that there are many nano-scale cavities between two parylene layers. Before the SPD, solvent can penetrate the parylene film and occupy those cavities. During the SPD, these solvents cannot be replaced by CO_2 completely, and hence result in a huge volume expansion when pressure is released near the end of the SPD process. Because of the delamination problem, an alternative method for preventing stiction was found.

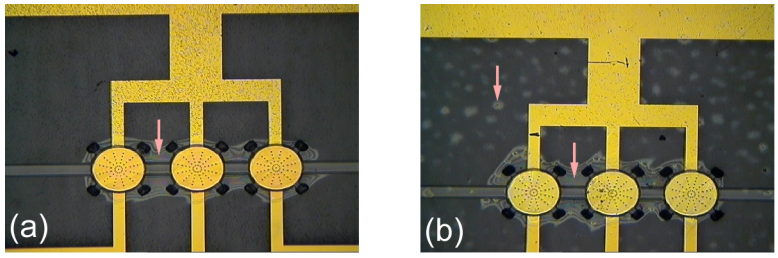

Figure 2-4 The delamination caused by the SPD. (a) The device was diped in acetone for 1 min then rinsed in methanol. (b) The device was diped in acetone for 1 min then submerged in methanol for 8 hours. Arrows point to the delamination site.

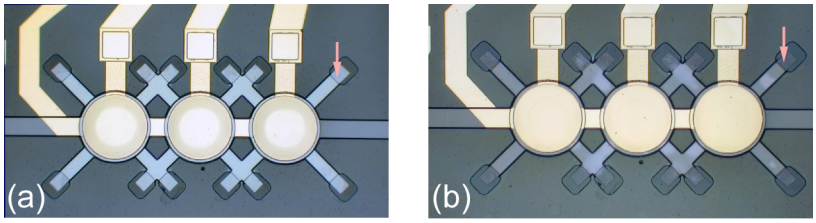

Figure 2-5 Anti-stiction by XeF_2 gas phase etching. (a) Center of the membranes had stiction. (b) The membranes became freestanding after XeF_2 etching. Arrows indicate a spot where the amorphous Si was etched away.

Previously gas-phase silicon etching has been used in creating large freestanding parylene structure [18]. So as described earlier in the final process, an extra sacrificial layer was introduced by sputtering amorphous silicon to partially define the actuation gap. When stiction occured after the photoresist sacrificial layer was dissolved away, the remaining sputtered Si layer was etched away using gas phase XeF_2 or BrF_3 etching to make the membrane freestanding. One example is shown in Figure 2-5. Although a 4 μm sacrificial layer was used to compensate for any membrane deformation caused by the stiction, the final actuation gap *d* was still less than the original design value of 3 μm.

2.3.3 Low Temperature Process

One important feature of this technology is that the whole process was carried out at low temperature once the silicon oxide was grown. All of the Parylene and photoresist process steps were done below 120 °C. Although exact temperatures during oxygen

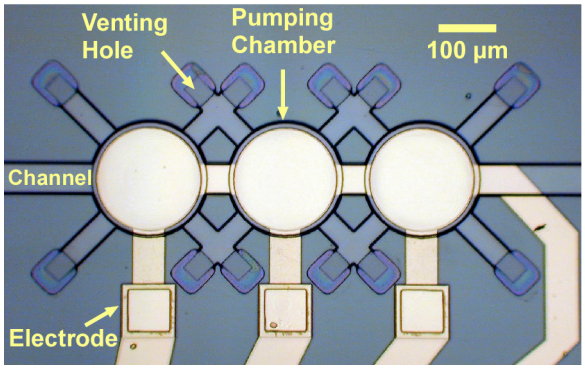

Figure 2-6 Photomicrograph of the fabricated device.

plasma etching, XeF_2 etching, and metallization were not measured, they are estimated to be less than 120 $^{\circ}$C as well. This opens up possibility of integrating electronics underneath the microfluidic network and doing post-CMOS surface micromachining. Figure 2-6 is a photomicrograph of a fabricated micro pump.

2.4 EXPERIMENTAL

2.4.1 Electrostatic Actuation

To test the electrostatic actuation of the moving membrane, a DC voltage was applied to the top electrode while the fixed electrode on the substrate was grounded. By varying the applied voltage and observing the actuation, the pull-in voltage can be determined. First, this testing was done on testing structures that had varying membrane diameters. There

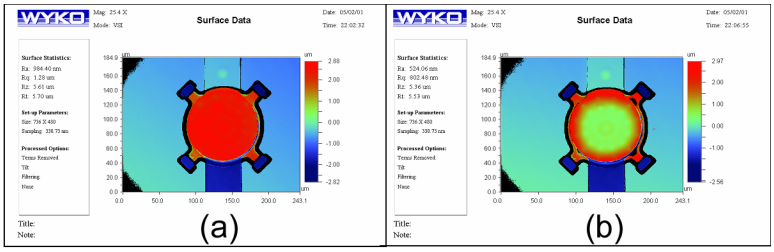

Figure 2-7 Wyko surface profile scan of the electrostatic actuation. (a) No voltage applied. (b) 400 V was applied to the electrodes. The center of the membrane was pull down.

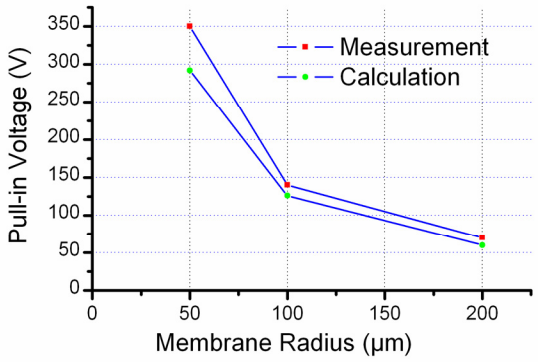

Figure 2-8 Pull-in voltages for membranes with different diameters.

test structures did not have a fluid channel above the membrane. These membranes were made freestanding by CO_2 SPD. Figure 2-7 shows scans from an optical surface profiler (WYKO NT1100, Veeco Instuments) that demonstrates the electrostatic actuation on a 100-μm diameter membrane. Figure 2-8 gives the measured pull-in voltages for membranes with different diameters and also the theoretical values that are calculated from Equation (2.1).

To calculate the theoretical pull-in voltage, the residual stress σ and the Young's modulus E was chosen to be 20 MPa and 3.2 GPa, respectively. This value is based on a previous study [19] and the temperature history of the parylene membrane during the fabrication process. The height of the actuation gap d is estimated to be 2 μm which is much less than the thickness of the sacrificial layers. As discussed before, the reduction in height is most likely due to stiction.

The variation of the pull-in voltage is around 20% for the same diameter membrane. This variation was expected since pull-in is very sensitive to the actuation gap d. Because stiction likely caused permanent deformation of the membrane, and since the degree of stiction can be affected by many factors (e.g. drying speed), final values of d were not well controlled. Based on these testing results, in the final design for the micro pump, the diameter of the membrane was chosen to be 100 μm.

The pull-in voltage of the membrane in the complete micro pump structure was also measured. It was typically around 110 V, but was found to vary from 80 V to 130 V between different chips. Large differences in pull-in voltage were especially observed between chips from different wafers. As suggested by Equation (2.1), a 25% variation in d can change the pull-in voltage by a factor of 2. Because of the more complicated

structures involved in the micro pump compared to the testing structures, the variation in *d* here is even larger. By comparing surface profile scans of the actuation membrane before and after actuation, *d* was estimated to be around 2 µm. For a 100-µm radius and 2-µm thick parylene membrane with 2-µm actuation gap, the theoretical pull-in voltage is 126 V, which is in close agreement to the measured average.

If the membrane was actuated for extended durations or at high voltages (~200 V), shifts in the pull-in voltage were observed. In some cases, the membrane would remain in the actuated state even after the applied voltage was released. This type of behavior has been observed on other electrostatically actuated parylene structures studied by our group. Parasitic charging of dielectric surfaces was believed to be the main cause [16, 20]. Besides inconsistent actuation, electrolysis of the liquid in the channel was a serious problem as well. To try and reduce the extent of electrolysis and charging of the dielectric interface, an AC actuation signal was used[20]. The principle of using AC actuation to counteract the parasitic charging is given by Figure 2-9.

For this study, a 5 kHz sinusoidal driving signal was used for the electrostatic actuation. The pull-in voltage using this AC signal was measured to be approximately 140 V_{peak} (100 V_{rms}). Even after extended periods of actuation, attenuation of the actuation magnitude was not observed. The AC actuation signal was made using a high-

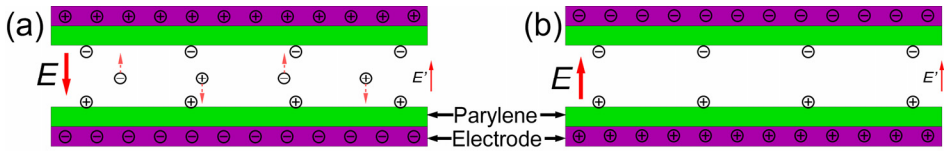

Figure 2-9 Dielectric charging and AC actuation. (a) Parasitic charges build up during actuation. E is the actuation electric field. E' is the electric field of parasitic charging. The effective electric field strength is E-E'. (b) After switching the polarity of the electric field and the relaxation of parasitic charging, the effective field is E-E'.

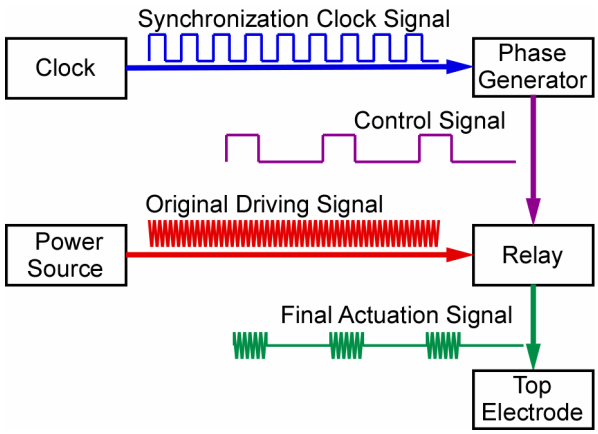

Figure 2-10 Various signals were used to realize peristaltic actuation of the micro pump. Here the diagram shows all the signals used for one pumping chamber.

voltage MOSFET op-amp (PA98 Apex Microtechnology, Tuscon, Arizona). The op-amp could output voltage swings from ±225 V and had a slew rate of 1000 V/μs. The signal to be amplified was produced using a Wavetek Model 275 signal generator. An HP 6209B and a Stanford Research Systems PS310 high voltage supply were used to provide the op-amp source voltages.

2.4.2 Peristaltic Actuation

3-phase peristaltic actuation was explored for the micro pump. For each actuation chamber, a control signal switched a solid-state relay that subsequently controlled the AC actuation voltage. Effectively, the control signal forms an envelope over the driving signal, as shown in Figure 2-10. To achieve peristaltic motion, the control signals of the three actuation chambers obeyed a 3-phase peristaltic sequence, which was generated by a logic circuit and driven by a 1-100 Hz clock as shown in Figure 2-10.

The digital circuit for controlling the 3-phase actuation sequences were made using conventional 7400 series CMOS based ICs. The circuit consisted of a counter which output the desired sequence of signals. The clock signal was produced using a HP 33120A function generator. Furthermore, the digital circuit was designed such that changing the duty cycle of the clock signal changed the duty cycle of the actuation sequence as well. The duty cycle could be varied from 20-80%. The digital circuit output switched optical isolation relays capable of switching up to 350 V (LCC110, Clare, Beverley, MA) with a switching time of approximately 0.1 ms. These relays controlled the high voltage actuation signal produced by the op-amp. The circuit was also designed such that when the digital output was low, both electrodes were grounded as opposed to being left floating, this helped reduce charging effects and led to more consistent actuation. Figure 2-11 shows the video snapshots of a 3-phase actuation sequence.

2.4.3 Pumping Measurement

Flow rate measurement in the range of several nL/min proved to be very difficult. Any off-chip measurements would be extremely difficult due to the huge dead volume resulting from the packaging and coupling. For flow visualization, 1 μm polystyrene beads (Duke Scientific, Palo Alto, CA,) were placed in the fluid at a concentration of tens

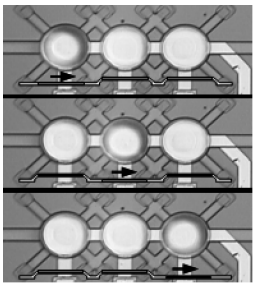

Figure 2-11 Video snapshots from a 3-phase actuation.

of beads per nL. These beads allowed us to visually measure the pumping rate while not interfering with pump operation. To measure the pumping rate, first, video was recorded using the microscope of a probe station (Micromanipulator, Model 6000, Carson City, NV) and a CCD video camera (Hitachi, Model KP-D20BU). Then, by analyzing the video of the moving beads, the flow rate could be deduced. During pumping, the beads were found to oscillate back and forth due to the pulse-like peristaltic actuation. It is the net movement that was translated into the calculated flow rate. This pump was tested with both ethanol and water. Ethanol proved a more suitable fluid for testing because even with an AC actuation signal, electrolysis of water was still observed in some cases.

Figure 2-12 shows sequential snapshots of a pumping test. The beads are highlighted in the photographs for clarity. The pump was actuated at 140 Vp (5 kHz AC), using a 20-Hz phase frequency for the 3-Phase sequence. Here, phase frequency refers to the frequency of the entire 3-phase-cycle, which is 1/3 of the clock frequency. Bead velocity was measured to be 100 μm/sec. Figure 2-12 also shows the pumping rate of ethanol vs. phase frequency. The actuation voltage used in this test was again 140 Vp (5 kHz AC). The pumping rate reaches a maximum of 1.7 nL/min at 20 Hz and decreases at higher frequencies. It can be clearly seen that at lower frequencies the pumping rate

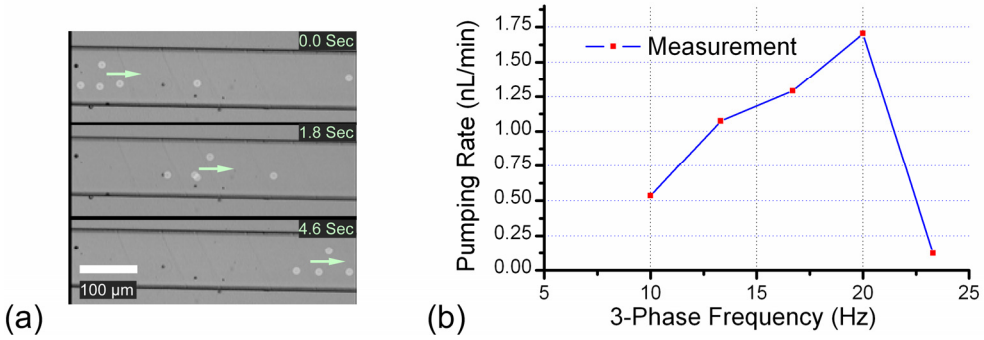

Figure 2-12 Measurement of the pumping rate. (a) The video snapshots from the pupmping test. (b) The pumping rate vs. phase frequency.

increases almost linearly with the increasing frequency. At higher frequencies, the moving membrane is not fast enough to keep up with the actuation signal, so the actuation magnitude decreases, thus reducing the pumping efficiency.

Due to the small pressures generated by this micro pump, we were not able to measure the pumping pressure directly using an off-chip pressure meter. The pumping pressure, at a pumping rate of 1.7 nL/min, was estimated to be 1.6 kPa. This pressure estimate was calculated by assuming that the channels connecting the pump to the inlet/outlet dominated the total flow resistance. The effective dimensions of these channels are 100 μm (W) × 5 μm (H) and have an effective length of about 24 mm.

2.5 MODELING AND ANALYSIS

To further understand the behaviour of the micro peristaltic pump, this section presents a model that considers the interactions of the vibrating membranes and the fluid flow. We first model each pumping chamber and the associated electrostatic membrane actuator, and then represent the pump as a system in which individual chambers and actuators interact with each other. The resulting lumped-parameter model will be solved numerically to yield insight into the peristaltic pump operation, especially the dependence of pumping flow rate on actuation frequency. Definitions of all the symbols used in this section can be found in Table 2-1.

2.5.1 Single Chamber Model

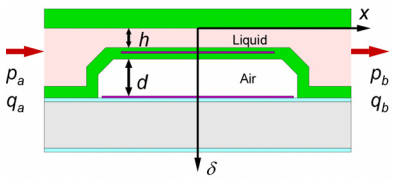

Figure 2-13 Model for a single pumping chamber.

As shown in Figure 2-13, each pumping chamber is modelled as a thin fluid film sandwiched between a stationary rigid plate (representing the chamber ceiling) and a flexible membrane that is actuated by electrostatic force. At zero actuation voltage, the fluid film has thickness h while the air gap separating the membrane from the ground electrode has height d. As the pump operates at frequencies (< ~100 Hz) much lower than the membrane's natural frequency (estimated to be ~600 kHz), the inertia of the membrane can be ignored. In addition, the membrane can be approximately represented by a rigid plate that is attached to an linear spring K and moves (quasistatically) with displacement δ. The effective spring constant is chosen in such a way that the pull-in voltage for a pair of parallel plates (one of which is spring-supported) [5, 15] is consistent with Equation (2.1). Thus,

$$K = \left(\frac{27}{8}\right)\left(\frac{1.55\pi}{\alpha}\right)\sigma t_m = \left(\frac{16.43}{\alpha}\right)\sigma t_m \tag{2.5}$$

As the membrane inertia is ignored, the forces on the membrane are in equilibrium. The equation of motion for the membrane is then given by Equation (2.6):

$$K\delta = F_h + F_e \tag{2.6}$$

where the electrostatic actuation force F_e due to an applied voltage V is given by Equation (2.7):

$$F_e = \frac{\varepsilon_0 V^2 A}{2(d + t_i/\varepsilon_p - \delta)^2} \tag{2.7}$$

To obtain a closed-form expression for the hydrodynamic force F_h, a first approximation is used where the fluid film, bounded by the pair of stationary and moving rigid plates as described above, is treated to be square in shape with area A. As the liquid film thickness is small compared with the membrane diameter, and membrane vibrations occur at low frequencies, it is reasonable to ignore fluid inertia and assume the pressure, p, to be uniform across the fluid film. The Reynolds equation in classical lubrication theory [21] then adequately describes the hydrodynamics of the liquid film. In the coordinate frame shown in Figure 2-13, this equation takes the form

$$\begin{cases} \dfrac{\partial}{\partial x}\left((h+\delta)^3 \dfrac{\partial p}{\partial x} \right) = 12\mu\dot{\delta} \\ p\big|_{x=0} = p_a \,,\; p\big|_{x=\sqrt{A}} = p_b \end{cases} \tag{2.8}$$

where μ is the liquid viscosity, and p_a and p_b are pressures immediately upstream and downstream of the chamber, respectively. The pressure on the membrane can be solved from this equation, and integrated to yield the hydrodynamic force which is given by

$$F_h = -\frac{\mu A^2}{(h+\delta)^3}\dot{\delta} + \frac{1}{2}(p_a + p_b)A \tag{2.9}$$

In addition, it can be shown that q_a and q_b, the rates of fluid flow into and out of the chamber, are related to the chamber inlet and outlet pressures by

$$q_{\substack{a \\ b}} = -\frac{(h+\delta)^3\sqrt{A}}{12\mu}\frac{\partial p_{\substack{a \\ b}}}{\partial x} = \pm\frac{1}{2}\dot{\delta}A + \frac{(h+\delta)^3}{12\mu}(p_a - p_b) \tag{2.10}$$

Continuity of fluid flow also requires

$$q_a - q_b = A\dot{\delta} \tag{2.11}$$

Thus, we have obtained a model for each pumping chamber, consisting of Equations (2.6) (with Equations (2.7) and (2.9) substituting for F_e and F_h), (2.10) and (2.11).

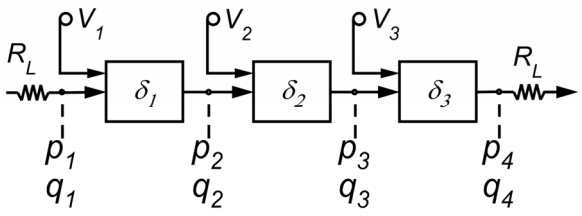

Figure 2-14 Representation of the pump as a system consisting of individual chambers and micro channels.

2.5.2 System Model

With the chamber model above, the pump can be represented as a system consisting of the three chambers and the inlet and outlet channels leading to and from the pump, as illustrated in Figure 2-14. Here, the deflection δ_i of the i^{th} membrane (actuated by voltage V_i), is related to the flow rates q_i and q_{i+1}, and pressures p_i and p_{i+1} by Equations (2.6), (2.7), and (2.9). Neglecting flow inertia, the inlet and outlet channels are each represented by a flow resistance given by

$$R_L = \frac{12\mu L}{WH^3} \tag{2.12}$$

where L, W, and H are the channel length, width and height, respectively. Then, assuming the reservoirs where the channels originate or terminate are at atmospheric pressure, the flow rate and pressures immediately upstream and downstream of the pump are related by

$$-p_1 = R_L q_1, \quad p_4 = R_L q_4 \tag{2.13}$$

The pump model hence consists of a system of nonlinear ordinary differential equations as the electrostatic and hydrodynamic forces (Equations (2.7) and (2.9)), and the chamber flow rates (Equations (2.10) and (2.11)) are nonlinear in membrane deflections, but can be readily solved numerically. Here we used the commercial numerical simulation software MATLAB (The Mathworks Inc., Natick, MA).

We now present calculations of pumping flow rates and pressures calculated from the pump model. Consistent with the experiment, a 3-phase voltage sequence is used:

$$V_i = V(t-(i-1)T/3) \quad i = 1,2,3 \tag{2.14}$$

Here $V(t)$ is a square wave of period T, such that $V(t)$ = 140 V if $0 < t < T/3$, and $V(t)$ = 0 V if $T/3 < t < T$. We choose nominal values d = 2 μm and t_i = 2 μm, and allow h to vary from 0.1 to 1.2 μm. The inlet and outlet channels each have effective length 24 mm, width 100 μm, and height 5 μm. The time-averaged pumping flow rate and pressure difference p_4-p_1 (Figure 2-13) obtained for various values of h are shown in Figure 2-15 and Figure 2-16. It can be seen that in general, for a given fluid film thickness h, the average flow rate and pressure difference initially increase with frequency, reaches a maximum (i.e. resonance), and then decrease with frequency. In particular, for h = 0.6 μm, the average flow rate achieves a maximum of 1.78 nL/min, and the average pressure difference achieves a maximum of 1.63 kPa, both at 18 Hz. This behavior is consistent with the experimental data (Figure 2-12).

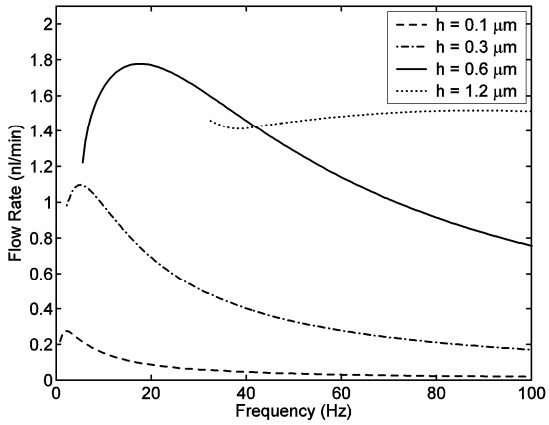

Figure 2-15 Calculated frequency dependence of the time-averaged pumping flow rate.

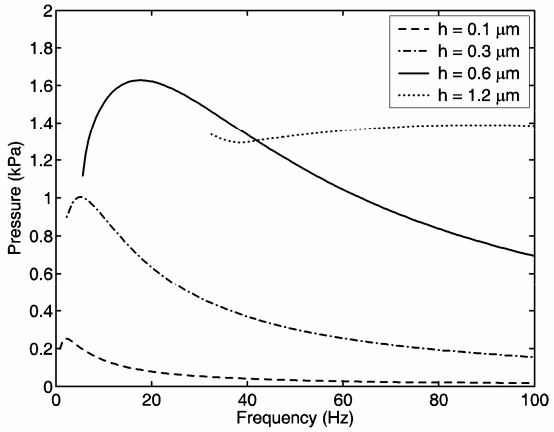

Figure 2-16 Calculated frequency dependence of the time-averaged pressure difference p_4-p_1.

Note that h = 0.6 μm, along with d = 2 μm, is considered to lie in the range of the actual parameter values for the device tested, which we were not able to accurately measure. It can also be seen from the figures that as h decreases, the frequency at which the flow rate and pressure reach the maximum steadily decreases, due to increasingly large damping of membrane vibrations (Equation (2.9)). The maximum flow rate and pressure difference initially increase, and then decrease with h. This is due to the competing effects, both resulting from the decrease in h, of increased damping on membrane vibrations, and reduced backward flow due to improved sealing of the fluid chambers.

In Figure 2-15 and Figure 2-16, the actuation voltage (140 V) exceeds the pull-in voltage (128 V), and the membranes therefore vibrate beyond the critical displacement $(d+t_i/\varepsilon_p)/3$ as given by static theory [5]. The vibration is adequately described by our model provided the excitation frequency is not too low to cause the touchdown of the membrane on the bottom electrode. Therefore, computations have been performed for each h only at frequencies that do not cause membrane touchdown. The frequency

dependence of the flow rate can be attributed to the complex interplay of the excitation frequency, and the amplitude and phase of membrane stroke vibrations. For example, as shown in Figure 2-15 and Figure 2-16, there is a local minimum in flow rate and pressure for h = 1.2 μm, although this minimum is quite insignificant. More importantly, the interplay between the frequency and membrane stroke volume is the cause for flow rate to reach a maximum. At low frequencies the tendency for an increase in frequency to increase the flow rate dominates over the tendency for the reduced membrane stroke volume to decrease the flow rate, and at frequencies beyond the maximum, the relative significance of these tendencies is reversed. Simulation also confirms that although the net pumping pressure and flow rate is not very high, the instantaneous flow rate and pumping pressure can be very high.

2.6 CONCLUSIONS

Based on a multiplayer parylene, surface-micromachining technology, an electrostatically actuated micro peristaltic pump has been developed. The electrostatic actuation of parylene structures was studied along with the problems associated with it, such as charging and electrolysis. An AC actuation voltage combined with a 3-phase peristaltic actuation sequence, were used to demonstrate fluid pumping. A reasonable flow rate (1.7 nL/min) and an estimated pumping pressure of 1.6 kPa were achieved. The relationship between pumping and phase frequency was also characterized. The pump dynamics and performance were then addressed further by an analysis based on a lumped-parameter model of the system. The analysis also yielded insight into the role that each design parameter plays. Due to its small footprint, large-scale integration becomes feasible. Moreover, since the micro pump shares the same platform technology as many other

devices we have previously developed (e.g. valve, electrospray ionization nozzle, filter and flow sensor, etc.), total integration for a μTAS becomes feasible.

REFERENCES:

[1] P. R. Selvaganapathy, E. T. Carlen, and C. H. Mastrangelo, "Recent progress in microfluidic devices for nucleic acid and antibody assays," *Proceedings of the IEEE*, vol. 91, pp. 954-975, 2003.

[2] N. Lion, T. C. Rohner, L. Dayon, I. L. Arnaud, E. Damoc, N. Youhnovski, Z. Y. Wu, C. Roussel, J. Josserand, H. Jensen, J. S. Rossier, M. Przybylski, and H. H. Girault, "Microfluidic systems in proteomics," *Electrophoresis*, vol. 24, pp. 3533-3562, 2003.

[3] N. T. Nguyen, X. Y. Huang, and T. K. Chuan, "MEMS-micropumps: A review," *Journal of Fluids Engineering-Transactions of the Asme*, vol. 124, pp. 384-392, 2002.

[4] L. X. Chen, J. P. Ma, F. Tan, and Y. F. Guan, "Generating high-pressure sub-microliter flow rate in packed microchannel by electroosmotic force: potential application in microfluidic systems," *Sensors and Actuators B-Chemical*, vol. 88, pp. 260-265, 2003.

[5] G. T. A. Kovacs, *Micromachined transducers sourcebook*. Boston, MA: WCB/McGraw-Hill, 1998.

[6] C. Cabuz, E. I. Cabuz, W. R. Herb, T. Rolfer, and D. Zook, "Mesoscopic Sampler Based on 3D Array of electrostatically activated Diaphragms," presented at The 10th International Conference on Solid-State Sensors, Actuators and Microsystems, (Transducers'99), 1999.

[7] J. W. Judy, T. Tamagawa, and D. L. Polla, "Surface-machined micromechanical membrane pump," presented at Proceedings of IEEE International Workshop on Micro Electro Mechanical Systems (MEMS '91), 1991.

[8] X.-Q. Wang and Y.-C. Tai, "A normally closed in-channel micro check valve," presented at The 13th Annual International Conference on Micro Electro Mechanical Systems (MEMS 2000), 2000.

[9] M. A. Unger, H. P. Chou, T. Thorsen, A. Scherer, and S. R. Quake, "Monolithic microfabricated valves and pumps by multilayer soft lithography," *Science*, vol. 288, pp. 113-116, 2000.

[10] T. Thorsen, S. J. Maerkl, and S. R. Quake, "Microfluidic large-scale integration," *Science*, vol. 298, pp. 580-584, 2002.

[11] M. Carmona, S. Marco, J. Samitier, and J. R. Morante, "Dynamic simulations of micropumps," *Journal of Micromechanics and Microengineering*, vol. 6, pp. 128-130, 1996.

[12] M. Q. Bu, T. Melvin, G. Ensell, J. S. Wilkinson, and A. G. R. Evans, "Design and theoretical evaluation of a novel microfluidic device to be used for PCR," *Journal of Micromechanics and Microengineering*, vol. 13, pp. S125-S130, 2003.

[13] R. Zengerle and M. Richter, "Simulation of Microfluid Systems," *Journal of Micromechanics and Microengineering*, vol. 4, pp. 192-204, 1994.

[14] C. Grosjean, X. Yang, and Y.-C. Tai, "A Thermopneumatic Peristaltic Micropump," presented at The 10th International Conference on Solid-State Sensors, Actuators and Microsystems, (Transducers'99), 1999.

[15] P. M. Osterberg and S. D. Senturia, "M-TEST: A test chip for MEMS material property measurement using electrostatically actuated test structures," *Journal of Microelectromechanical Systems*, vol. 6, pp. 107-118, 1997.

[16] T.-J. Yao, K. Walsh, and Y.-C. Tai, "Dielectric charging effects on Parylene electrostatic actuators," presented at The 15th IEEE International Conference on Micro Electro Mechanical Systems (MEMS 2002), Las Vegas, NV, 2002.
[17] N. Tas, T. Sonnenberg, H. Jansen, R. Legtenberg, and M. Elwenspoek, "Stiction in surface micromachining," *Journal of Micromechanics and Microengineering*, vol. 6, pp. 385-397, 1996.
[18] T. J. Yao, X. Yang, and Y. C. Tai, "BrF3 dry release technology for large freestanding parylene microstructures and electrostatic actuators," *Sensors and Actuators a-Physical*, vol. 97-8, pp. 771-775, 2002.
[19] T. A. Harder, T.-J. Yao, Q. He, C.-Y. Shih, and Y.-C. Tai, "Residual stress in thin-film parylene-C," presented at The 15th IEEE International Conference on Micro Electro Mechanical Systems (MEMS 2002), Las Vegas, NV, 2002.
[20] W. van der Wijngaart, H. Ask, P. Enoksson, and G. Stemme, "A high-stoke, high-pressure electrostatic actuator for valve applications," *Sensors and Actuators a-Physical*, vol. 100, pp. 264-271, 2002.
[21] A. Cameron and C. M. M. Ettles, *Basic lubrication theory*, 3rd ed. Chichester, New York: E. Horwood ; Halsted Press, 1981.

Chapter 3

Integrated Surface-Micromachined Micro Flow Controller

3.1 INTRODUCTION

Flow control is an essential function for most microfluidic systems. Active flow control with an integrated flow sensor for feedback has been a long sought goal in the microfluidic field [1]. While many micro flow control components (e.g. micro valves and flow sensors) have been demonstrated separately using a variety of technologies [2], incompatibility among different fabrication technologies still remains a huge challenge during total integration. To overcome this challenge, it has been a long-term goal for us to develop a technology that allows the total integration of an active micro valve and flow sensor for feedback flow control.

Various actuation mechanisms have been applied to micro valves [2], each having its own advantages and limitations. These limitations often make a particular valve only suitable for specific applications. For example, thermopneumatic actuation [3] produces large deflection with large force, but high power consumption and undesired heating limit its applications. Similar problems also apply to micro valves based on thermal expansion, such as biomorph and shape-memory-alloy actuated valves. Piezoelectric actuation can yield large forces, but cannot generate large displacements without the stacking of several piezoelectric layers, the fabrication of which can be difficult to integrate with other

processes. Silicone rubber micro valves with off-chip pneumatic actuation and impressive large-scale integration has been demonstrated [4]. However, pneumatic interfacing can prove to be an undetachable burden if highly portable systems are required.

Because of low power consumption and easy implementation, electrostatically actuated micro valves are attractive and have been widely explored [5-7]. These demonstrated valves are all based on either bulk micromachining or need multi-chip packaging. Unlike those micro valves, our new electrostatically actuated micro valve was entirely surface micromachined using parylene technology. Because of the versatility of the multilayer process, a thermal based flow senor can be easily integrated with the micro valve for flow measurement and feedback flow control. The integrated flow sensor is similar to other previously demonstrated hot-wire type flow sensors [8]. Moreover, this micro flow controller is based on the same technology presented in Chapter 2, and in fact, it was fabricated on the same chip with the peristaltic micro pump. This is a demonstration of the flexibility and capability that out developed multilayer parylene surface micromachining technology possesses.

3.2 DESIGN

3.2.1 Operation Principle

Figure 3-1 shows the structural design of the micro flow controller and its operation principle. The design takes advantages of the versatility and flexibility of the multilayer parylene technology. Valve actuation is realized by using electrostatic force to actuate a circular moving membrane. An opening in the center of the membrane provides a fluidic pathway between two channels. The moving membrane is a composite structure that

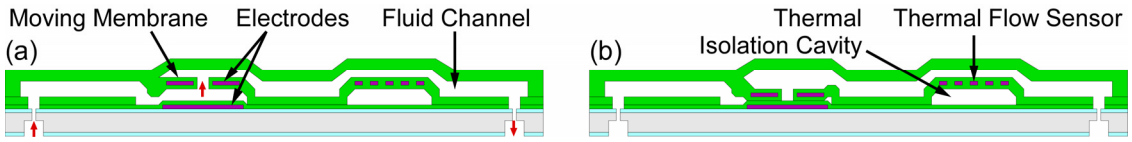

Figure 3-1 Structure design and operation principle of the micro flow controller. (a) Valve is open and the arrows indicate flow direction. (b) Valve is close when voltage is applied.

consists of a Cr/Au electrode sandwiched between two parylene layers, which provide good electrical insulation. A ground electrode is fixed on the substrate below the moving membrane. When a high voltage is applied between the two electrodes, the electrostatic force collapses the membrane onto the valve seat to close the fluid pathway. When the voltage is released, the restoring force of the membrane and hydraulic pressure push the membrane up and open the pathway. So this micro valve is a normally open valve. Unlike the design of the peristaltic micro pump in Chapter 2, the electric field in the valve actuation gap passes though the fluid that is being regulated. This limits the valve application mainly to gas and liquid not prone to electrolysis, such as organic solvents.

The integrated thermal flow sensor is basically a resistive temperature detector (RTD) which simultaneously is used as a heater. Its operation principle is based on hot-wire type flow sensor, where the fluid flow inside the channel affects heat transfer between heater of the heater and its environment and hence the overall temperature of the heater. Two modes are usually employed for these types of flow sensors: constant current mode and constant temperature mode. Here, constant current mode is preferred because it is more easily implemented than constant temperature operation. Constant current is passed through the heater, and the heater temperature is a function of the current and the flow rate. By measuring the voltage drop across the heater, the resistance can be deduced

and the temperature determined. By correlating the voltage drop with the flow rate, a flow sensor can be realized.

Heat loss to the substrate can reduce the sensitivity of the flow sensor and increase power consumption. A thermal isolation cavity is created underneath the heater to reduce the heat loss to the substrate. The cavity is filled with air whose thermal conductivity is three times smaller than parylene and at least two orders of magnitude smaller than silicon oxide. Since the fabrication of the flow sensor is very similar to that of the micro valve, incorporating the flow sensor with the valve does not add complexity into the fabrication process. This will be evident in the section discussing the fabrication process.

3.2.2 Parameter Design

The design of the moving membrane and the actuation gap is very similar to the design of the individual pumping chambers in Chapter 2. To provide good electrical insulation of the top electrode, it is encapsulated between two 1 μm thick parylene layers. And to try to prevent membrane stiction, the circular membrane was designed to have a 100 μm radius. The opening in the middle of the membrane has 25 μm radius. The height of the fluid channel on top of the valve membrane is not reduced via partial exporsure like it was in the case of the peristaltic pump. To estimate the operational pressure range that this valve can seal against, we can use a parallel-plate approximation. The pressure generated by the electrostatic force, P_e, is given by

$$P_e = \frac{\varepsilon_0 V^2}{2(d + \frac{2t_i}{\varepsilon_p})^2} \tag{3.1}$$

where d is the distance between the two electrodes, t_i is the thickness of the insulation parylene, V is the applied voltage, and ε_0 and ε_p are the permittivity of air and dielectric

constant of parylene. Based on the values given in Chapter 2, here d is approximately 2 μm and t_i is 1 μm. Then using 200 V voltage, roughly 26 kPa can be generated by electrostatic actuation on the membrane at initial open position.

The flow sensor is operated in the constant current mode. A constant current is applied to the heater and voltage drop cross the heater is monitored. Temperature sensitivity S_T of the flow sensor is defined by

$$S_T = \frac{\Delta T}{\Delta Q} \tag{3.2}$$

where ΔT is the temperature change corresponding to a flow rate change ΔQ. The sensitivity of the flow sensor S_V is given by

$$S_V = \alpha S_T V_0 \tag{3.3}$$

where V_0 is the bias voltage, α is the temperature coefficient of resistance of the heater electrode. Then for a given input power P_0 and resistance R_0 at the initial bias, S_V can be written as

$$S_V = \alpha S_T \sqrt{P_0 R_0} \tag{3.4}$$

It can be seen that to maximize the sensitivity, both the resistance and power need to be increased. Increasing the power too high can lead to undesirable heating of the fluid, which can be detrimental, especially when temperature sensitive biological or chemical substances are involved. So in order to increase the sensitivity we had to increase the heater resistance. For the 180 nm thick Au layer, the square resistance is very low, only 0.12 Ω/sq. In order to increase heater resistance, a long meandering geometry was used. The final design was a meandering line approximately 4 μm wide and 3000 μm long, with a total resistance of around 90 Ω.

To determine the optimal geometry of the micro channel on top of the heater, the results of a previous study [9] were used. In this study, the power consumption of the heater P was found to be related to the flow rate Q using through

$$P = T_{diff}\left(A\left(\frac{6\rho\mu}{h^2 w}Q\right)^{\frac{1}{n}} + B\right) \tag{3.5}$$

where A, B, and n are empirical parameters, ρ and μ are the density and viscosity of the fluid respectively, h and w are the height and width of the channel respectively, and T_{diff} is the temperature difference between the heater and the fluid. n is empirically determined to be > 2. For a given T_{diff} and Q, to maximize the heat exchange between the fluid and the heater, h and w need to be as small as possible. However, w cannot be reduced too much since the meandering heater must be accommodated spatially. So reducing h is a more effective way to increase the sensitivity, and h was designed to be around 1 μm.

3.3 FABRICATION

The fabrication process for the micro flow controller is very similar to that of the micro pump presented in Chapter 2. Some modifications were made to accommodate the design parameters of the micro flow controller. The fabrication process is shown in Figure 3-2. The devices are fabricated using a multilayer process where parylene is the structural material, photoresist as the sacrificial layer and chrome/gold as the heater and electrode material. The process starts with a 4-inch silicon wafer. Inlets and outlets for the fluidic channels were etched from the backside using a standard Bosch DRIE process until a 50 μm thick silicon membrane was left.

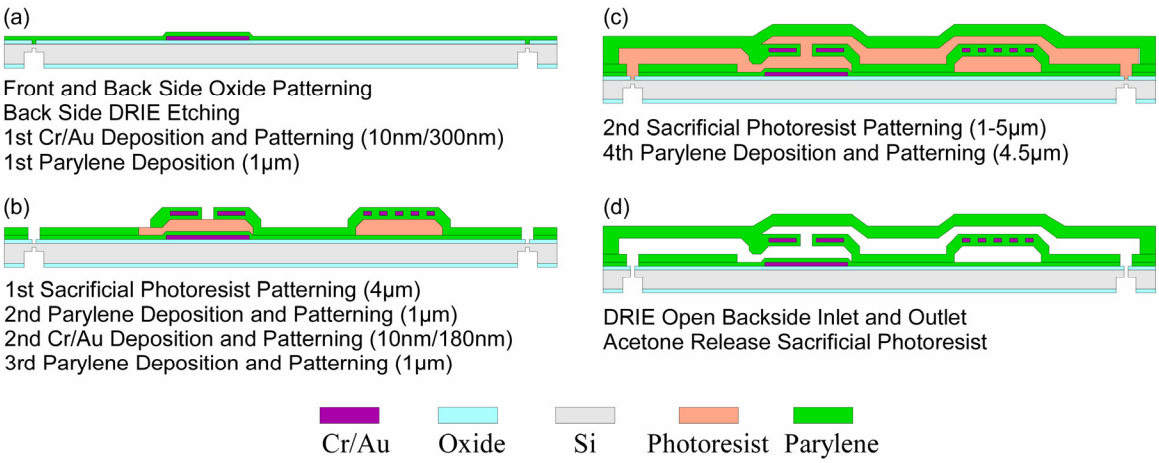

Figure 3-2 Fabrication process of the micro flow controller. It uses the same technology that is described in Chapter 2 with some modification.

The process was continued on the front side. The front side oxide was patterned to expose the inlet and outlet for the fluidic channels that were formed later in the process. A Cr/Au (10 nm/300 nm) layer was thermally evaporated and then patterned on the front side to form the bottom electrode. Then to isolate the bottom electrode from the environment, 1 μm parylene-C was deposited. A first photoresist sacrificial layer (4 μm) was formed and patterned to define the actuation gap and the thermal isolation cavity underneath the flow sensor. Next, the moving actuation membrane, consisting of a parylene/metal/parylene sandwich structure, was created. To do this, a second 1 μm parylene-C layer was deposited and patterned; the top electrode layer was formed by another evaporated 10 nm/180 nm Cr/Au layer; and a third 1 μm parylene-C layer was deposited to encapsulate the top electrode. This encapsulation insured that the electrode was isolated from the fluid channel. Patterning of the parylene was done using oxygen plasma with photoresist or Al as a mask. An orifice in the center of the membrane was patterned to provide the communication between the actuation gap which is part of the bottom channel and the top channel which is formed in a later step. The second electrode layer also defines the heater of the flow sensor. Once the moving membrane was finished,

the top fluid channel was formed by a second photoresist sacrificial layer and a 4.5 μm fourth parylene-C layer. The height of the fluid channel, as determined by the thickness of the second photoresist sacrificial layer, varied as a result of the uneven step coverage of photoresist over the existing structures. A partial double exposure was carefully performed to reduce the channel height immediately above the flow sensor as required by the design specifications. The process is then resumed on the backside. The remaining 50 μm silicon membrane was etched away using DRIE to fully open the inlet and outlet of the fluid channel. Finally, the sacrificial photoresist was released using acetone. After releasing, the chips were rinsed with isopropanol rinse and allowed to dry.

Like the micro pump, stiction can happen during the drying process. Because of the orifice that connects the top and bottom channels, the stiction is less severe than in the case of the micro pump. Unfortunately, gas-phase etching of amorphous silicon is not an option here; due to the long channels that gas etchant would have to diffuse through before it reaches the moving membrane region. So if stiction occurred, ethanol flow was forced through the valve to make it freestanding.

Figure 3-3 is a photomicrograph of the fabricated device.

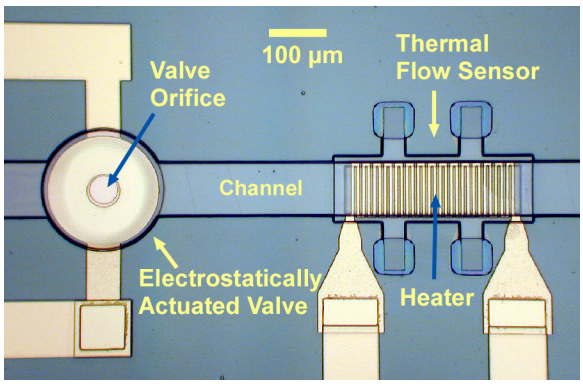

Figure 3-3 Photomicrograph of the fabricated device.

3.4 TESTING AND RESULTS

3.4.1 Flow Sensor Characterization

Very few commercially available flow meters can measure flow down to nL/min range. Packaging and interfacing with off-chip instruments also poses a big challenge. We utilized a flow sensor calibration setup that is similar to that in [8]. An Acrylic jig shown in Figure 3-4 was custom-made to hold the chip in position and allow us to couple the chip with tubing. For air flow calibration, a constant pressure was applied to the inlet and a precision 10 μL syringe was connected at the inlet. The volumetric flow rate was measured by recording the traveling speed of a bead of water in the syringe. For water flow calibration, a syringe pump (KD Scientific) was used to deliver a precise flow rate down to the nL/min range. Due to the dead volume associated with the Acrylic jig, this testing setup cannot calibrate flow rate down to sub nL/min, although the syringe pump specifications allows that.

The thermal sensor is operated in constant current mode. Temperature compensation is necessary because of fluctuations in ambient temperature as well as gradual heating of the substrate. The temperature fluctuations are in general large compared to the temperature change induced by the flow so the temperature

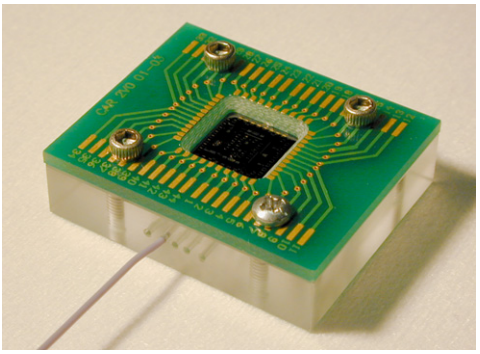

Figure 3-4 Testing jig: an acrylic base with an PCB cover.

compensation is absolutely necessary. To compensate for the effect of ambient or substrate temperature variations, outputs of two sensors with identical geometries were measured simultaneously. One of them was the actual flow sensor and the other was a compensation sensor located nearby. The differential output of these two sensors was taken as the final output for flow measurement. The temperature coefficient of resistance α of the gold heater was also calibrated using an environmental chamber. α was measured to be 0.33 %/^{o}C.

Figure 3-5 shows the flow sensor calibration for both air and water flow. When calibrating air flow, a 4-mA bias current was applied, which set the operating temperature of the heater to 6.3^{o}C above the ambient. Sensitivity S_V is 55 μV/(μL/min) and temperature-to-flow ratio S_T is 0.033 ^{o}C/(μL/min). The output voltage was measured with a HP34401A multimeter at a rate of 1 Hz. The resolution of the voltage measurements is around 10 μV. So the resolution of the flow rate measurements is roughly 0.2 μL/min. For water flow calibration, the bias current was again 4 mA. The sensitivity S_V is 12.2 μV/(nL/min) and the temperature-to-flow ratio S_T is 0.0073 ^{o}C/(nL/min). The water flow calibration proved to be more difficult than the air flow. Due to the relatively large volume of the off-chip testing setup compared to the small flow rate, stabilization of flow

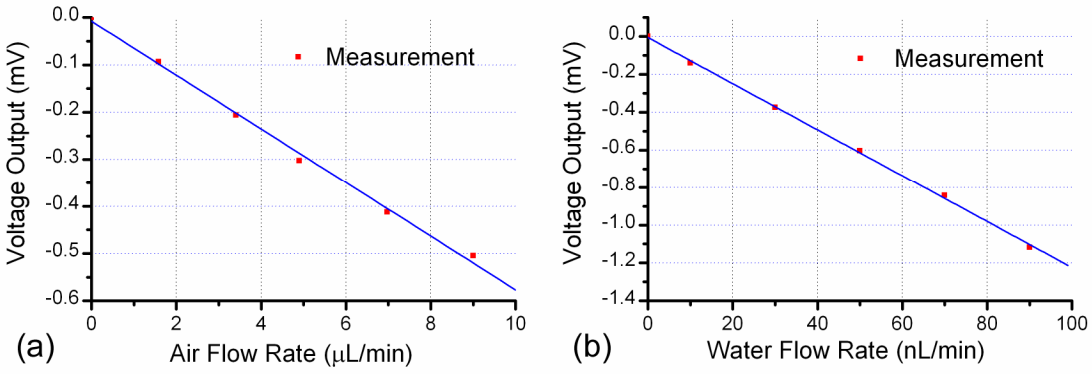

Figure 3-5 Flow sensor calibration for both air and water flow.

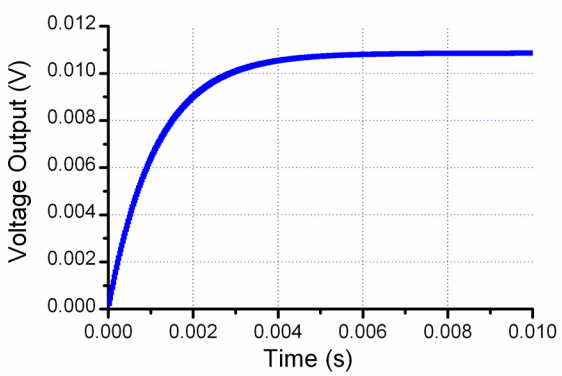

Figure 3-6 Time response of the flow sensor.

took longer than 60 min. This actually demonstrates the importance and advantage of on-chip flow measurement.

To study the dynamics of the thermal flow sensor, the time response of the heater is measured. This was done by switching on the bias current and recording the voltage output vs. time. After switching on the 4 mA bias current, there is a nearly instantaneous jump to a voltage corresponding to the zero-bias resistance. The voltage, or resistance, change as a function of time, due to the heating, is given in Figure 3-6. The response time of the heater is measured to be about 1.0 ms. Data was collected using a HP54645 digital oscilloscope.

3.4.2 Electrostatic Actuation

Similar to the characterization of the micro pump in Chapter 2, the pull-in voltage for the valve membrane was measured. The DC pull-in voltage is measured to be around 130 V. It is, as expected, larger than the DC pull-in voltage of the micro pump, because the center of the membrane where the maximum deflection and charge density are located in the micro pump membrane becomes the orifice for the valve membrane. If the membrane was actuated for extended durations or at high voltages (~200 V), shifts in the pull-in voltage or attenuation of the actuation strength were observed. The shifted pull-in

voltage can be as high as 180 V. To solve this problem, an AC actuation voltage was used. A 10 kHz sinusoidal voltage was applied to the top electrode while the bottom electrode was grounded. A high frequency is needed so there are no oscillations of the valve at the actuation signal frequency. Using AC voltage, the pull-in voltage is about 150 V_{peak} (106 V_{rms}). The AC actuation is clearly better for the valve because of the more stable and reliable actuation.

When water was used as the working fluid, serious electrolysis problems were observed regardless of whether DC or AC actuation was used. This occurred even though both electrodes were encapsulated with Parylene, which theoretically should provide good electrical insulation to restrict the current flowing through. With water as the fluid, the DC actuation voltage could be reduced to around 30 V because of the increased dielectric constant. But almost immediately, bubbles were generated. Due to the rapid volume expansion of the bubbles in such a small and confined space (<0.1 nL), there was severe, permanent damage to the valve membrane. The valve cannot reliably operate in water unless the electrolysis problem is solved. Anther problem with the liquid testing was that stiction would likely occur after the testing. The flow control of liquids which have a high resistance to electrolysis, such as Fluorinert, has been demonstrated. But not enough data were obtained due to the difficulty of measurement.

3.4.3 Micro Flow Controller

Two operation modes were investigated and compared to demonstrate the flow control capability of the micro flow controller. One mode uses using the actuation voltage amplitude to adjust the closing force on the valve membrane in order to adjust flow resistance across it. The other is to use Pulse Width Modulation (PWM) [7]. In both

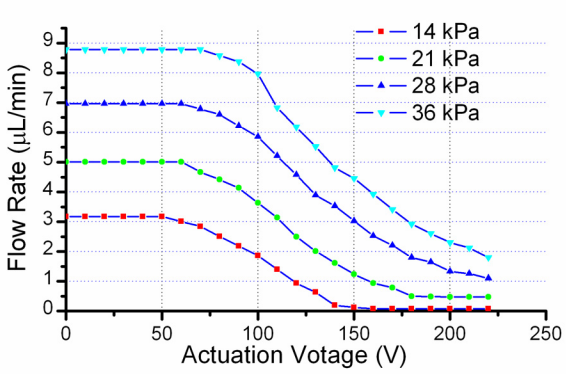

Figure 3-7 Flow rate vs. valve actuation voltage.

modes, the flow sensor output was used to measure the flow rate based on the calibrations presented in previous section. A constant pressure was applied to the channel inlet to induce flow. The valve actuation signal frequency was kept at 10 kHz.

Figure 3-7 shows the relationship between flow rate and actuation voltage amplitude. Here, the voltage is peak voltage. When the applied pressure increases, the voltage needed to counteract the pressure and close the valve increases accordingly. However, for the pressure that is higher than 28 kPa, the valve cannot be fully closed with voltages up to 220 V_p, which is the highest voltage we were able to produce. This is very close to the estimated capabilities based on Equation (3.1) which suggests that 26 kPa can be generated by a 200-V actuation voltage. It is also clear that due to the positive feedback characteristic of electrostatic actuation, the linear region of the control curve is small. The higher the pressure, the more non-linear the control curve becomes.

Since electrostatic actuation exhibits the pull-in phenomenon, it would be more beneficial to operate the valve in an on/off binary mode instead of the analog mode that is shown in Figure 3-7. In this situation, PWM can be utilized to control the flow rate by adjusting valve duty cycle which is defined as the ratio of durations between on and off. One requirement for the PWM operation is that the membrane has to switch fast enough

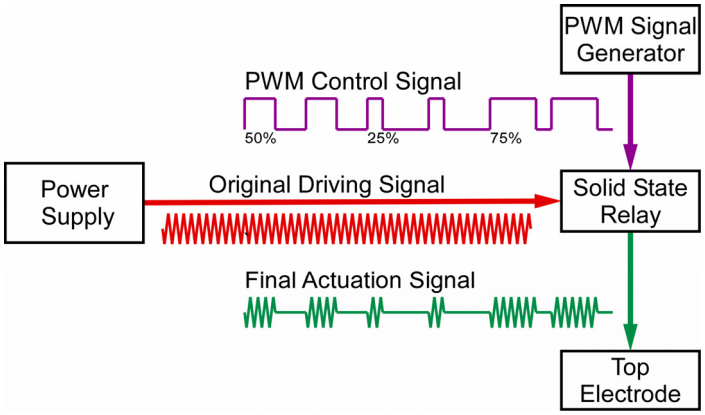

Figure 3-8 PWM control scheme for the flow cotnroller.

such that the downstream flow is not noticeably affected by the pulsation induced by the PWM. Figure 3-8 illustrates the control scheme of PWM. A 100-Hz PWM signal generated by HP 33120A function generator was applied to a solid state relay. The relay then switched the valve on and off by switching the 10 kHz actuation signal.

The flow sensor should be suitable for measuring the instantaneous flow rate because the swept volume between it and the valve outlet is less than 250 pL and its own response time is on the order of 1 ms. To test whether the valve membrane can respond to a 100-Hz PWM signal, the flow sensor output was measured using HP54645 digital oscilloscope. Figure 3-9 shows the system response to a 100-Hz and 50 % duty cycle control signal. The actuation voltage used in the test was 160 V_{peak} and the applied

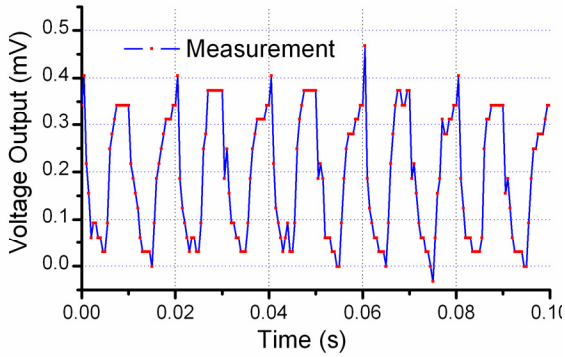

Figure 3-9 System time response to a 100 Hz control signal.

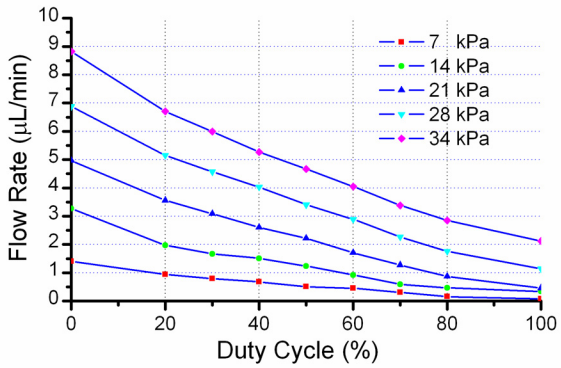

Figure 3-10 Flow rate vs. duty cycle in PWM control mode.

pressure was 34 kPa. System response time is estimated to be around 1.5 ms, which implies the valve actuation response time is likely on the order of 1 ms as well.

Figure 3-10 shows the flow control results using PWM mode under different applied pressures. The control was done by 100 Hz PWM control signal and 200 V_{peak} 10 kHz actuation voltage. For pressures lower than 21 kPa, the valve can be nearly completely closed. From 20% to 80% duty cycle, the control is quite linear. Non-linearity at both low (<20%, 2 ms) and high (>80%, 8 ms) duty cycles is likely to be caused by the fact that pulse durations of either on or off mode are approaching the valve speed limit which is around 1 ms. Thus PWM operation becomes less ideal at both ends. Even with this non-linearity, PWM control still exhibits more linearity than the control achieved by adjusting actuation voltage.

3.5 CONCLUSIONS

Based on the same fabrication technology that was used in the micro pump, an entirely surface micromachined electrostatically actuated valve has been demonstrated. Due to the flexibility and versatility of the technology, a thermal flow sensor was integrated with the valve which could be used for feedback control. The testing results shows that the flow

sensor has a sensitivity of 55 μV/(μL/min) for air and 12.2 μV/(nL/min) for water. The estimated resolution is about 0.2 μL/min for air and 1 nL/min. The time response of the flow sensor is on the order of 1 ms. Two modes, actuation voltage adjustment and PWM were investigated in characterizing the use of the valve to control air flow. Using the flow sensor to measure the regulated flow rate, the testing results show that PWM has better linearity and performance. At an actuation voltage of 200 V, pressures up to 21 kPa can be closed off.

REFERENCES:

[1] C. M. Ho and Y. C. Tai, "Micro-electro-mechanical-systems (MEMS) and fluid flows," *Annual Review of Fluid Mechanics*, vol. 30, pp. 579-612, 1998.

[2] G. T. A. Kovacs, *Micromachined transducers sourcebook*. Boston, Ma.: WCB, 1998.

[3] X. Yang, C. Grosjean, and Y. C. Tai, "Design, fabrication, and testing of micromachined silicone rubber membrane valves," *Journal of Microelectromechanical Systems*, vol. 8, pp. 393-402, 1999.

[4] T. Thorsen, S. J. Maerkl, and S. R. Quake, "Microfluidic large-scale integration," *Science*, vol. 298, pp. 580-584, 2002.

[5] W. van der Wijngaart, H. Ask, P. Enoksson, and G. Stemme, "A high-stoke, high-pressure electrostatic actuator for valve applications," *Sensors and Actuators a-Physical*, vol. 100, pp. 264-271, 2002.

[6] S. Messner, J. Schaible, J. Vollmer, H. Sandmaier, and R. Zengerle, "Electrostatic driven 3-way silicon microvalve for pneumatic applications," presented at Micro Electro Mechanical Systems, 2003. MEMS-03 Kyoto. IEEE The Sixteenth Annual International Conference on, 2003.

[7] P. Dubois, B. Guldimann, M.-A. Gretillat, and N. F. de Rooij, "Electrostatically actuated gas microvalve based on a Ta-Si-N membrane," presented at The 14th IEEE International Conference on Micro Electro Mechanical Systems, (MEMS 2001), 2001.

[8] S. Y. Wu, Q. Lin, Y. Yuen, and Y. C. Tai, "MEMS flow sensors for nano-fluidic applications," *Sensors and Actuators a-Physical*, vol. 89, pp. 152-158, 2001.

[9] Y. Xu, C.-W. Chiu, F. Jiang, Q. Lin, and Y.-C. Tai, "Mass flowmeter using a multi-sensor chip," presented at Micro Electro Mechanical Systems, 2000. MEMS 2000. The Thirteenth Annual International Conference on, 2000.

Chapter 4

Integrated Capacitive Sensors for Microfluidic Applications

4.1 INTRODUCTION

Microfluidic sensors, such as pressure, flow rate, volume, and fluid property sensors, are vital in achieving precise control and full automation of microfluidic systems. This becomes increasingly important as microfluidic systems get more sophisticated and move toward large-scale integration. For example, micro pump needs flow sensor to provide feedback for precise pumping rate control. Many devices and methods for microfluidic sensing have been developed [1, 2]. These include thermal flow sensors for flow rate measurement [3], and conductivity sensor for both flow rate and fluid composition measurements [4].

Due to their simple physical structure and temperature insensitivity, capacitive sensors have been widely used in many macro scale applications, such as proximity detectors, motion encoders, and pressure sensors [5]. Capacitive sensing has also been utilized in fluid sensing applications such as fluid level sensing, determination of ion concentration [6], and for measuring the makeup of mixtures (e.g. oil and water). Capacitive sensing has also been widely adopted in MEMS devices. One good example is the accelerometer that is commercially available from Analog Devices and is prominent in almost all vehicles made today for collision detection. There have also been some

instances where capacitive sensing has been applied into microfluidic systems. A micromachined pressure/flow sensor [7] used a capacitive differential pressure sensor to measure the pressure drop across a precise micromachined flow restriction. This pressure drop could then be used to deduce the flow rate. However, this particular device involved a three-chip packaging which could prevent it from being used for in-situ pressure measurement inside a microfluidic system. A liquid level sensor based on capacitive sensing integrated with a micro dosing system has also been demonstrated [8].

The capacitive based microfluidic sensors presented in this chapter exhibit all the functionality of the previously mentioned sensors (i.e. pressure, flow rate, volume, and composition), but with the added flexibility and ease of integration of our developed multilayer parylene surface-micromachining technology.

4.2 DESIGN

4.2.1 Operation Principle

For simplicity, a parallel-plate capacitor is used as an example to explain the design of the capacitive microfluidic sensors discussed in this chapter. The capacitance of a parallel-plate capacitor C is given by

$$C = \frac{\varepsilon A}{d} \tag{4.1}$$

where d is the distance between the two plates or electrodes, A is the area of the plates, and ε is the permittivity of the media between the two plates. A change in any one of these three parameters will change the measured capacitance. We will be investigating each of these three parameters and their applications to three different sensor configurations. These include a membrane based pressure sensor (varying d); a parallel-

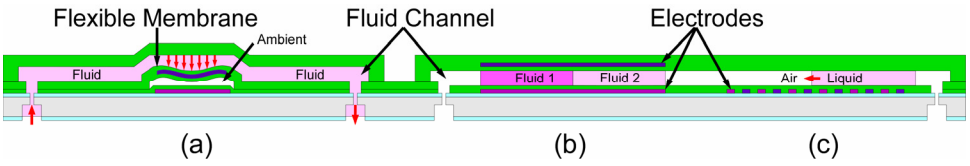

Figure 4-1 Structure designs and operation principles of the three sensors configurations. (a) The pressure/flow sensor. (b) The parallel-plate fixed-electrode configuration. (c) The interdigitated configuration.

plate fixed-electrode configuration for dielectric measurements (varying ε or A); and an interdigitated configuration for use in volumetric and dielectric measurements (varying ε or A). The operation principles of the three sensor configurations are shown in Figure 4-1.

The pressure sensor is basically a parallel-plate capacitor. The upper electrode of the capacitor is sandwiched between the floor of the fluid carrying channel and another parylene layer, forming a composite flexible membrane. The bottom electrode is fixed on the substrate. Between the two electrodes is a cavity created beneath the channel and connected to the ambient environment. Changes in the local channel pressure will cause a deflection of the composite flexible membrane. The capacitance therefore varies as a function of the local pressure in the channel. The air cavity is not sealed, making this a differential pressure sensor. Since the capacitive element is completely underneath the channel, the pressure reading should be largely independent of the fluid being carried. Effects such as leakage of the fringe field might into the fluid channel may cause the sensor to be slightly dependent on the working fluid in the channel. Assuming the outlet is at the ambient pressure and the flow resistance between the outlet and the pressure sensor is fixed, the flow rate in the channel can also be calculated from the reading given by the pressure sensor.

The parallel-plate fixed-electrode configuration consists of two electrodes, one placed in the roof of the channel and the other placed in the floor of the channel. The

fluid inside the channel becomes the dielectric media between the two electrodes. Change in the dielectric constant of the channel fluid will register as a capacitance change. Properties such as the mixing ratio of two liquids can be determined through appropriate calibration since the effective dielectric constant is a function of the mixing ratio. One target application will be gradient monitoring for reverse-phase HPLC. In RP-HPLC, the mobile phase generally consists of mixtures of aqueous buffer solutions with various water-miscible organic solvents. The mixing ratio changes over time to form a solvent gradient, where the polarity of the mobile phase decreases over time. Since the polarity of the mixtures is directly related to the effective dielectric constant of the mixtures, there is a gradual change in the effective dielectric constant that corresponds to the solvent gradient and can be easily detected using the proposed sensor. Also, pure liquids can be identified provided they have different dielectric constants. Besides determining fluid properties, such a sensor can be used to easily determine whether a particular channel is filled.

The interdigitated electrode configuration consists of two interlocking comb-shaped electrodes that are fixed beneath the floor of the channel. The fringing electric field reaches into the channel so changes in the dielectric constant of the channel fluid are registered as a capacitance change. Besides the same applications mentioned for the parallel plate configuration, the interdigitated configuration can also be used to monitor liquid front position. As a column of liquid flows into an empty channel and begins to pass over the electrode fingers of the sensor, a predictable increase in capacitance that is a function of the fluid front position can yield a direct measurement of volume.

Compared to the parallel-plate configuration, the interdigitated configuration is simpler to fabricate since only one layer of metal is needed. Also, the interdigitated configuration does not obscure the channel interior, therefore making it more desirable for calibration purposes. However, since the interdigitated sensor exploits the fringing electric fields, a weaker signal is expected.

4.2.2 Analysis and Parameter Design

The design details and equivalent circuits of the three sensors are discussed in this

Table 4-1 The symbols and parameters used in the analysis

Definition	**Symbol** (Value)
Constant or Material Property	
Permittivity of Free Space	ε_0
Dielectric Constant of Parylene	ε_p (3)
Dielectric Constant of Mixtures	ε_{mix} (20-80)
Dielectric Constant of Water	ε_w (80)
Dielectric Constant of IPA	ε_{IPA} (20)
Viscosity of Liquid	μ
Density of Parylene	ρ (1.3 g/cm^3)
Poisson Ratio	v (0.25)
Young's Modulus	E (4 GPa)
Residual Stress of Parylene Membrane	σ (13 MPa)
Model Parameters	
Thickness of Actuation Membrane	t_m (2 μm)
Thickness of Insulation Layer	t_i (1 μm)
Radius of Actuation Membrane	r (100 μm)
Height of Air Gap	d (1.5 μm)
Height of Sensor Channel	h_c (4 μm)
Width of Sensor Channel	w_c (100 μm)
Length of Sensor Channel	l_c (2 mm)
Spacing of Interdigitated Electrodes	s (6 μm)
Width of Interdigitated Electrodes	w (14 μm)

section. Definition of the symbols can be found in Table 4-1. In all the equivalent circuits diagram, the parasitic capacitances from below the electrodes (oxide, substrate) are ignored because they are in parallel with the capacitances from above the electrodes and don't contribute to the overall capacitance change. Also the capacitance of the electrical double layer on top the insulation parylene is also ignored because it is estimated to be around 100 pF which is much larger then the capacitance of the insulation parylene layer.

The equivalent circuit and diagram of the pressure/flow sensor, designated sensor A, are shown in Figure 4-2. From fabrication point of view, sensor A has an identical structure compared to the micro pump reported in Chapter 2. Although we can choose a completely different set of parameters for the sensor, in order to simplify the fabrication, the pressuer sensor dimentions are equivalent to those of an individual pumping chamber The total output capacitance C_{o1} is given by

$$C_{o1} = \frac{\frac{C_{p1}}{2} C_{gap}}{\frac{C_{p1}}{2} + C_{gap}} \tag{4.2}$$

where the capacitance of the parylene insulation layer C_{p1} is given by

$$C_{p1} = \frac{\varepsilon_p \varepsilon_0 \pi r^2}{t_i} \tag{4.3}$$

and based on the analysis in [9], the capacitance of the air gap C_{gap} is

$$C_{gap} = \frac{\varepsilon_0 \pi r^2}{d} \frac{tanh^{-1}(\sqrt{\frac{y}{d}})}{\sqrt{\frac{y}{d}}} \tag{4.4}$$

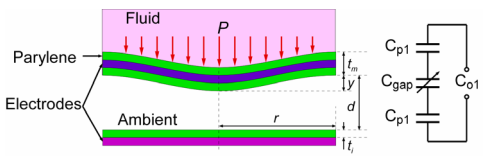

Figure 4-2 Diagram and equivalent circuit of the pressure/flow sensor.

where the center deflection y for an applied pressure P is

$$y = \frac{P}{\frac{16E}{3(1-\nu^2)}\frac{t_m^3}{r^4} + \frac{4\sigma t_m}{r^2}} \tag{4.5}$$

Here small deflections and clamped boundary conditions are assumed. Then for a given pressure P, the corresponding capacitance C_{o1} can be calculated using Equations (4.2) to (4.5).

To estimate C_{o1}, the material properties must be known. Based on a previous study and measurements done on the actual deflecting membrane, the Young's modulus E of parylene is found to be around 4 GPa and the residue stress σ is estimated to be 13 MPa. Although the original photoresist thickness that defines the gap is 4 μm, because of the stiction, the gap height d is reduced to 1.5 μm. Based on these values and Equations (4.2) to (4.5), the calculated output capacitance of the sensor is shown in Figure 4-3.

The sensitivity S_P of sensor A is defined by

$$S_P = \frac{\Delta C}{\Delta P} \tag{4.6}$$

where ΔC is the capacitance change corresponding to a pressure change ΔP. To maximize the sensitivity, the stiffness of the membrane needs to be reduced, but problems with

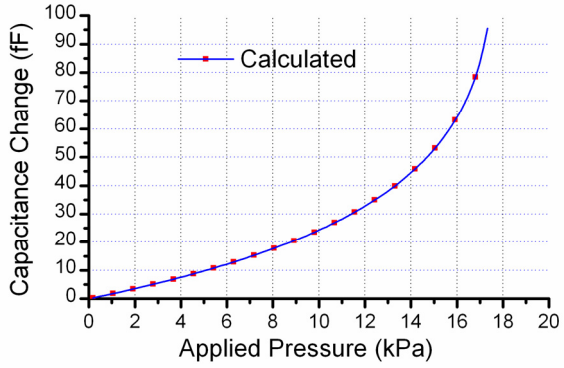

Figure 4-3 The estimated capacitance output of the pressure sensor at different applied pressure.

stiction put a lower limit on how much we can decrease the stiffness.

Sensor A can also be used as a flow sensor since the flow rate Q is related to the pressure drop P across certain fluid channel or restriction. The relationship for a rectangular channel with height << width is given by {Wu, 1998 #33}

$$Q = \frac{w_c h_c^3 P}{12\mu L}(1 + 2\alpha P) \tag{4.7}$$

where L is the channel length. The $1+2\alpha P$ accounts for bulging of the micro channel and comes from assuming that the channel height has a linear dependence on the pressure inside the channel.

The flow rate sensitivity S_Q of the sensor A is defined by

$$S_Q = \frac{\Delta C}{\Delta Q} \tag{4.8}$$

where ΔC is the capacitance change corresponding to a flow rate change ΔQ. If the bulging effect can be ignored, then S_Q becomes

$$S_Q = \frac{\Delta C}{\Delta P}\frac{\Delta P}{\Delta Q} = \frac{12\mu L}{w_c h_c^3} S_P \tag{4.9}$$

The equivalent circuit and diagram of the parallel-plate configuration, designated sensor B, are shown in Figure 4-4. Sensor B is similar to the sensor A, except that the membrane or electrode position is fixed and only the effective dielectric constant of the media is changing. The total output capacitance C_{o2} is given by

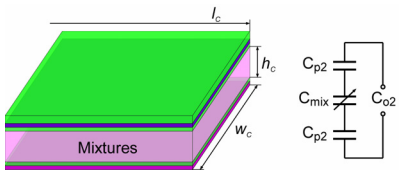

Figure 4-4 Diagram and equivalent circuit of the parallel-plate configuration.

$$C_{o2} = \frac{\frac{C_{p2}}{2} C_{mix}}{\frac{C_{p2}}{2} + C_{mix}} \tag{4.10}$$

where the capacitance of the parylene insulation layer C_{p2} and the capacitance of the mixtures C_{mix} are given by

$$C_{p2} = \frac{\varepsilon_p \varepsilon_0 w_c l_c}{t_i}; \quad C_{mix} = \frac{\varepsilon_{mix} \varepsilon_0 w_c l_c}{h_c} \tag{4.11}$$

where the length of the channel covered by the electrodes l_c is 2 mm, the width of the channel and electrodes w_c are 100 μm, the channel height h_c is 4 μm, and the thickness t_i of the insulation parylene that electrically isolates the electrodes from the fluid is 1 μm. The capacitance between air-filled channel and water filled channel is estimated to be 2.1 pF.

The main purpose of the interdigitated configuration, designated sensor C, is to detect liquid volume inside the channel. Shown in Figure 4-5, it can be treated as a capacitance network consisting of many capacitance units connected in parallel. Each capacitance unit corresponds to a pair of electrode fingers [10]. When liquid (e.g. water) passes over one finger pair, the capacitance associated with liquid C_w is switched on while the capacitance associated with air C_{air} is switched off. The resulting capacitance change $\Delta C^{'}$ can be expressed as

$$\Delta C^{'} = \frac{C_{p3} C_w}{C_{p3} + 2C_w} - \frac{C_{p3} C_{air}}{C_{p3} + 2C_{air}} \tag{4.12}$$

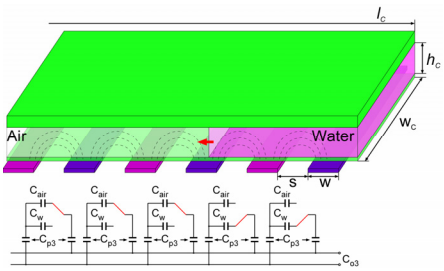

Figure 4-5 The detail design and equivalent circuit of the interdigitated configuration.

where the capacitance of insulation parylene on half of the finger C_{p3} is

$$C_{p3} = \frac{\varepsilon_p \varepsilon_0 \frac{w}{2} w_c}{t_i} \tag{4.13}$$

Using the analytical solution from[11] and considering the capacitance associated with the channel fluid, C_w can be expressed as

$$C_w = \frac{2\varepsilon_w \varepsilon_0 w_c}{\pi} \sum_{n=1}^{\infty} \frac{1}{2n-1} J_0^{\,2}\left(\frac{(2n-1)\pi s}{2(s+w)}\right) \tag{4.14}$$

where J_0 denotes the zeroth Bessel function of the first kind. The equivalent spacing between adjacent fingers s is 6 μm and the width of the finger w are 14 μm. Again, the electrodes are insulated from the channel with a 1 μm parylene layer and extended across the 2-mm long, 100 μm wide channel. C_{air} can be obtained by substituting ε_w, the dielectric constant of water, with the dielectric constant of air ε_0. The calculated capacitance change $\Delta C^{'}$ is 7.2 fF.

The capacitance change of the whole sensor is

$$\Delta C_{o3} = \frac{l_c}{s+w} \Delta C^{'} \tag{4.15}$$

When Sensor C is used as composition detector for a solvent mixture, we assume the effective dielectric constant of the mixture is a weighted average of the dielectric constant of each component. The weight is the concentration of the component. Based on

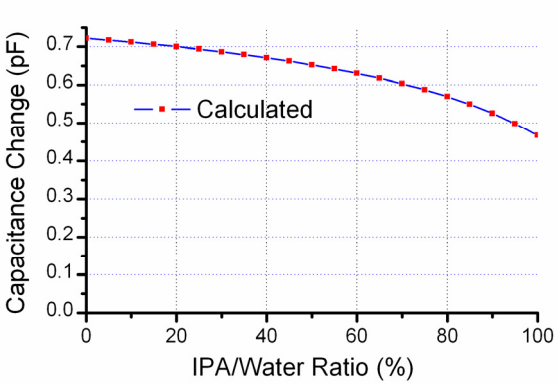

Figure 4-6 The output capacitance change of sensor C as a function of IPA/water mixing ratio.

Equations (4.12) to (4.15), the output capacitance at different mixing ratio can be calculated. Using IPA and water mixture as an example, Figure 4-6 shows the output capacitance at different mixing ratio. The capacitance is expressed as an increase over an empty channel.

4.3 FABRICATION

The sensors were fabricated using the same multilayer parylene surface micromachining technology described in Chapter 2. Four parylene structural layers and two sacrificial photoresist layers were used in the fabrication of these sensors. Two Cr/Au layers were used for the electrodes of the capacitors. Because of the way these sensors were designed, the sensors are automatically integrated into micro channels.

Based on the structural design shown in Figure 4-1, here are some process steps that are related to the fabrication of the sensors. Inlets and outlets for the fluidic channels were etched from the backside using DRIE. The front side oxide was patterned to expose the inlet and outlet for the fluidic channels. The first Cr/Au (10 nm/ 300 nm) layer metal layer defined the bottom electrodes of the pressure sensor and parallel-plate configuration. This layer was also used to define both electrodes in the interdigitated

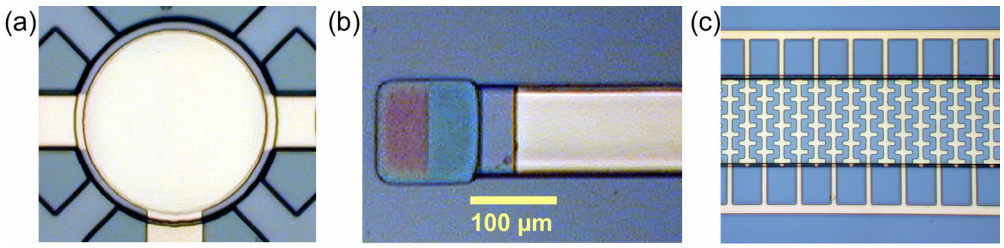

Figure 4-7 The photomicrographs of the fabricated sensors. (a) The pressure/flow sensor. (b) The parallel-plate fixed-electrode configuration. (c) The interdigitated configuration.

configuration. After the first parylene layer (1 µm) was deposited, the first photoresist sacrificial layer (4 µm) defined the capacitive air gap in the pressure sensor. This sacrificial layer also defined the micro channels in which the parallel-plate and interdigitated sensors were integrated. Also a sputtered silicon layer was patterned inside the capacitive air gap of the pressure sensor to ensure a freestanding pressure sensor membrane (process follows that used in chapter 2). After the second parylene layer (1 µm), the second Cr/Au layer (10 nm/ 180 nm) layer was deposited and patterned to produce the top electrodes of the pressure sensor and parallel-plate configuration. The third parylene layer (1 µm) was deposited and the second photoresist sacrificial layer (5 µm) was patterned to define the channel above the pressure sensor. Finally, DRIE was used to etch the fluidic ports completely through the wafer and the photoresist was released by acetone. Upon drying of the acetone, the pressure sensor membrane would often stick down because of stiction. Gas phase BrF_3 was used to etch away the sputtered silicon and produce a freestanding membrane. The inlets and outlets of some of the channels with the integrated sensors were opened at the front side to facilitate certain testing.

Figure 4-7 shows the photomicrographs of the fabricated devices.

4.4 TESTING AND RESULTS

4.4.1 Pressure/Flow Sensor

The pressure sensor was calibrated using a regulated pressure source. Pressure was applied to both ends of the channel simultaneously by means of the custom-built Acrylic jig that was used in the testing of the micro flow controller in Chapter 3, thus ensuring the channel pressure was at the desired value. The pressure was varied and the changing capacitance was recorded. Capacitances were measured using a commercially available IC (Microsensors UCR MS3110) which has a resolution of 4.0 aF/rtHz. Calibrations of the pressure sensor were done using both water and air as the channel fluid. The results are shown in Figure 4-8.

Two regions can be observed. In the low pressure region, designated region A, the response of the sensor shows a roughly linear increase in capacitance. The sensitivity is about 10 aF/Pa. Considering the capacitance readout IC resolution and bandwidth (8 kHz), the sensor resolution is estimated to be 30 Pa and the accuracy to be 1.0 kPa. At pressures higher than 19 kPa, designated region B, the sensitivity decreases to about 2.5 aF/Pa and the capacitance begins to plateau. This is likely caused by the membrane

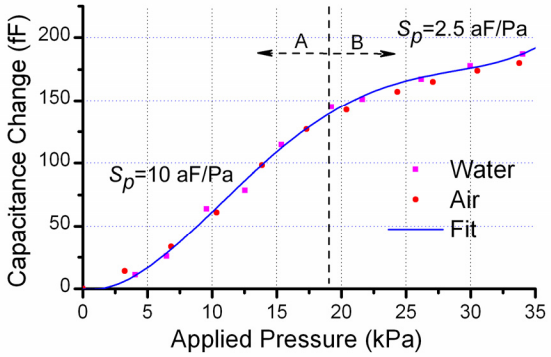

Figure 4-8 The pressure sensor calibration with water or air as the channel fluid.

bottoming out.

To investigate the pressure sensor behavior more thoroughly, the load and deflection characteristic of the composite membrane was measured using a WYKO NT1100 optical profiler. The membrane profile at different applied pressures is shown in Figure 4-9. Figure 4-9 clearly shows that the membrane touches the bottom substrate at the pressure higher than 17.5 kPa. This explains the two different regions in the measured sensor response shown in Figure 4-8. Based on Equation (4.5), the Young's modulus E of parylene is estimated to be around 4 GPa and residue stress σ to be 13 MPa. These measurements also indicate that the height of the air gap is about 1.5 μm, despite the use of a 4 μm photoresist layer to define the air gap. This discrepancy effectively decreases the pressure range of this sensor.

The initial shape of the membrane is not flat, as would be expected. Instead, the membrane exhibits a large downward deflection with the center of the membrane slightly bowed upward. This indicates that the membrane has been distorted during the fabrication process. After photoresist dissolution, stiction occurs betweens the membrane

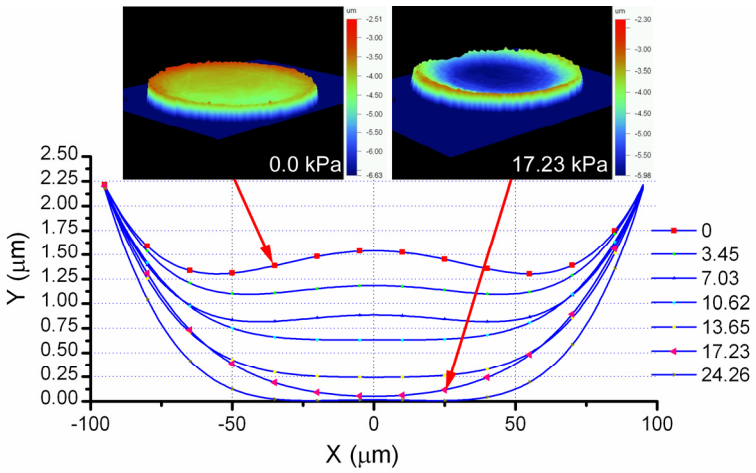

Figure 4-9 The WYKO surface profile scans under different applied pressure. Inlets show the WYKO scans at 0 kPa and 17.23 kPa.

and the floor of the capacitive air gap. The forces exerted on the membrane during drying might have been high enough to permanently deform the membrane, especially if the membrane was baked after stiction which could lead to build-up of a stress gradient in the membrane.

Although the capacitance measurements in region A of Figure 4-8 are roughly the same order of magnitude when compared to the theoretical response shown in Figure 4-3, the measured values are roughly 30% higher than the calculated values. The measurements also show a more linear response at the high end of region A when compared to the theoretical predictions. These discrepancies can be caused by several factors. First, the theoretical values can only be correct if an accurate estimation of material properties can be obtained. This is extremely difficult since multiple layers of different materials were involved and they went through complicated process conditions that are very different from simplified processes and structures from which those material properties were normally obtained. Second, the assumptions for the modeling are too simple. For example, the fixed-edge flat circular membrane is assumed and that is not the real scenario. Also the Cr/Au layer is ignored in the calculation of stiffness.

The pressure sensor was also tested as a flow sensor. This was done by applying pressure to the inlet of the micro channel and leaving the outlet open to the ambient. The pressure sensor is located in the center of this channel. By varying the applied pressure and at the same time recording the local pressure inside the channel and flow rate, the capability of this sensor to function as flow sensor based on a differential-pressure principle was demonstrated.

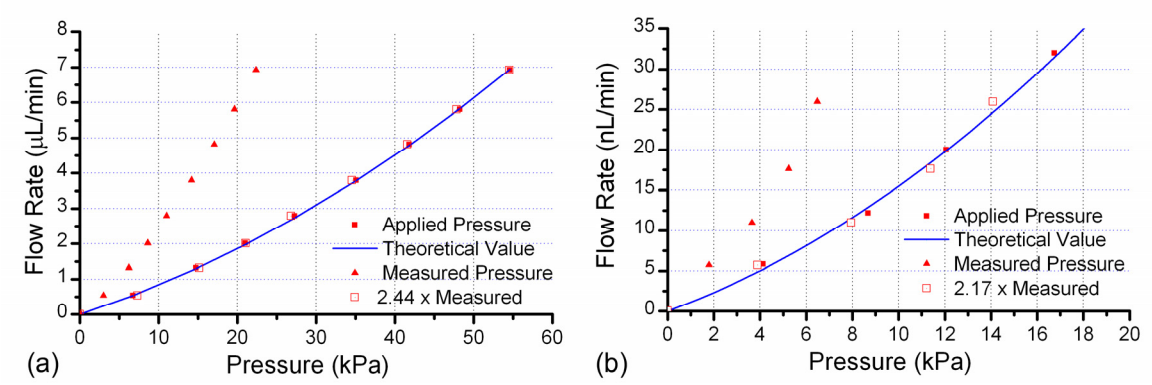

Figure 4-10 The calibration of the in-channel local pressure and the flow rate relationship. (a) Air flow. (b) Ethanol flow.

The applied pressure and the measured local channel pressure are shown in Figure 4-10, and are both related to the corresponding flow rate. The flow rate vs. applied pressure data was fit using Equation (4.7).

The measured data was fit assuming an air viscosity of 1.73e-5 kg/s-m. By fitting the data, α is found to be 0.0065 /kPa. The measured pressure in the center of the channel is found to be precisely 0.41 of the applied pressure. The line corresponding to 2.44 (1/0.41) times of the measured pressure is shown in Figure 4-10(a). The sensitivity S_Q of air flow is 40 fF/(μL/min) for flow rates less than 5 μL/min.

A similar test was done using ethanol as the channel fluid. The results are shown in Figure 4-10(b). The measured pressure at the center of the channel is found to be approximately 0.46 of the applied pressure in this test. The line corresponding to 2.17 (1/0.46) times of the measured pressure is shown in Figure 4-10(b). The measured data was fit assuming an ethanol viscosity of 1.2e-3 kg/s-m. By fitting the data, α is found to be 0.031 /kPa. The sensitivity S_Q of ethanol flow is 3 fF/(nL/min) for flow rate less than 100 nL/min.

4.4.2 Volumetric Sensor

The volumetric sensor is calibrated by introducing water into the interdigitated sensor. Figure 4-11 shows the output capacitance change related the water/air interface movement. The interface movement was captured on video and correlated with the capacitance measurements.

Figure 4-11(a) shows the sensor output as the water was introduced into the channel as a velocity of 5 mm/s which is equivalent to a flow rate of 120 nL/min. The measurement shown in Figure 4-11(b) corresponds to the sensor output as the water front passes over each successive finger. Since the cross section of the channel is fixed, this fluid front position corresponds directly to a volume. The distance between two adjacent fingers is 20 μm which corresponds to 8 pL. The sensor shows very high linearity in this short section of the sensor. The capacitance change corresponded to the water front passing over one pair of adjacent fingers is 8.2 fF. This is very similar to our calculated value of 7.2 fF. This discrepancy can be easily explained, since the electrodes are not the same geometry as the electrode configuration on which our theoretical model was based upon. Also a theoretical model of the actual electrode configuration would be extremely difficult. The final fabricated electrodes actually have prongs extending parallel to the

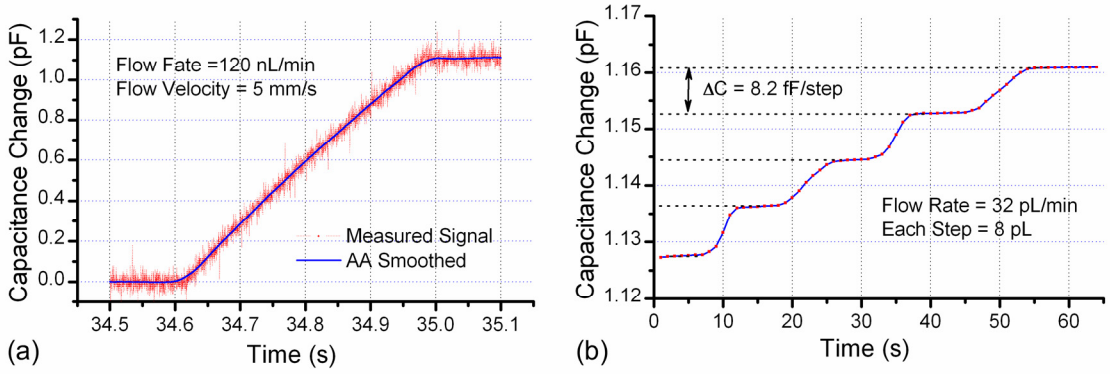

Figure 4-11 The volume sensing using interdigitated sensor configuration. (a) The sensor output as water front passes through the 2 mm long channel. (b) The sensor output as water front passes over each individual electrode.

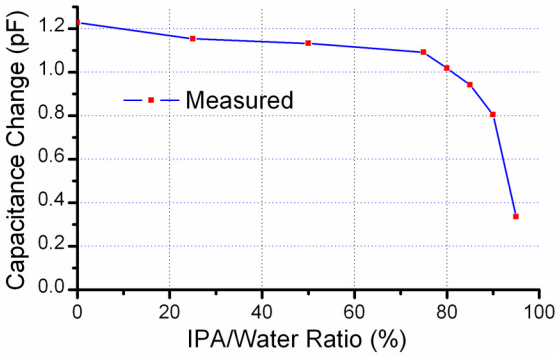

Figure 4-12 The capacitance change as a function of IPA and water mixing ratio.

channel, which lead to a higher than expected capacitance value. Based on the resolution of capacitance measurement, a volume resolution of < 5 pL should be easily attainable.

4.4.3 Dielectric Measurements

One simple use of the parallel plate and interdigitated sensors is to detect the presence of a fluid in a channel. For example, the capacitance of the sensors would increase significantly if there is water in the channel as opposed to air. For the parallel plate configuration the increase in capacitance was measured to be 3.38 pF. Since different fluids have different dielectric constants, it is also possible to distinguish a large variety of fluids, provided their dielectric constants are different.

A proof of concept was done using mixtures of isopropyl alcohol and water. The measured interdigitated capacitance increase for varying mixtures is shown in Figure 4-12. Except for the absolute values, the order of magnitude and the general trend that were measured are predicted very well by previous analysis.

4.5 CONCLUSIONS

Three types of capacitive fluidic sensors were demonstrated in several microfluidic applications. These include sensors for fluid pressure, flow rate, volume, and composition

measurement. The sensors show great promise for microfluidic applications because of their high sensitivity and easy integration. The versatility of the parylene/photoresist surface micromachining technology allows for the integration of these sensors with other demonstrated devices for the creation of entire microfluidic systems.

REFERENCES:

[1] G. T. A. Kovacs, *Micromachined transducers sourcebook*. Boston, MA: WCB/McGraw-Hill, 1998.

[2] C. M. Ho and Y. C. Tai, "Micro-electro-mechanical-systems (MEMS) and fluid flows," *Annual Review of Fluid Mechanics*, vol. 30, pp. 579-612, 1998.

[3] S. Y. Wu, Q. Lin, Y. Yuen, and Y. C. Tai, "MEMS flow sensors for nano-fluidic applications," *Sensors and Actuators a-Physical*, vol. 89, pp. 152-158, 2001.

[4] R. Rocklin, H. Yin, D. Sobek, C. Pavel, and K. Killeen, "Use of conductivity electrodes as on-chip sensors in chromatogaphic microfluidic devices," presented at Seventh International Conference on Miniaturized Chemical and Biochemical Anaylsis Systems (MicroTAS 2003), Lake Tahoe, CA, 2003.

[5] L. K. Baxter and IEEE Industrial Electronics Society., *Capacitive sensors : design and applications*. New York: IEEE Press, 1997.

[6] A. B. M. Ismail and K. Shida, "Non-contact multi-sensing technique for the precise measurement of concentration of electrolytic solution," *Sensors and Actuators, A: Physical*, vol. 69, pp. 152-155, 1998.

[7] R. E. Oosterbroek, T. S. J. Lammerink, J. W. Berenschot, G. J. M. Krijnen, M. C. Elwenspoek, and A. van den Berg, "Micromachined pressure/flow-sensor," *Sensors and Actuators, A: Physical*, vol. 77, pp. 167-177, 1999.

[8] G. Waibel, J. Kohnle, R. Cernosa, M. Storz, M. Schmitt, H. Ernst, H. Sandmaier, R. Zengerle, and T. Strobelt, "Highly integrated autonomous microdosage system," *Sensors and Actuators a-Physical*, vol. 103, pp. 225-230, 2003.

[9] S. P. Chang, J. B. Lee, and M. G. Allen, "Robust capacitive pressure sensor array," *Sensors and Actuators a-Physical*, vol. 101, pp. 231-238, 2002.

[10] W. Olthuis, W. Streekstra, and P. Bergveld, "Theoretical and Experimental-Determination of Cell Constants of Planar-Interdigitated Electrolyte Conductivity Sensors," *Sensors and Actuators B-Chemical*, vol. 24, pp. 252-256, 1995.

[11] M. W. den Otter, "Approximate expressions for the capacitance and electrostatic potential of interdigitated electrodes," *Sensors and Actuators a-Physical*, vol. 96, pp. 140-144, 2002.

Chapter 5

Electrochemical Pumping for On-Chip Gradient Generation

5.1 INTRODUCTION

5.1.1 Background

Liquid Chromatography (LC) has proven to be one of the most important analytical tools in proteomics. Miniaturization of LC is essential to meet the demands of fast growing proteomic research and development [1]. Although there have been many attempts to create an on-chip LC system, a complete on-chip LC system has yet to be realized. Among the various difficulties, the requirement of high-pressure on-chip fluidic pumping still remains as a daunting challenge [2]. Conventional LC pumps generally operate at pressures greater than 1000 psi. For on-chip LC systems though, a flow rate of 100 nL/min at 200 psi should be adequate, due to a shorter separation column.

Micro pumps can be classified as either mechanical or non-mechanical [3, 4]. Mechanical pumps often have moving parts and are based on actuation mechanisms such as electrostatic, thermo-pneumatic, piezoelectric, and electromagnetic actuation, etc. As mentioned in Chapter 2, mechanical pumps are difficult to be integrated into microfluidic systems. Also, because of complicated structures, the performance and reliability of micro-scale mechanical pumps cannot meet the general requirements of an integrated LC

system. With the exceptions of some published micro pumps that used piezoelectric actuation [5, 6], mechanical micro pumps are incapable of generating pressure differentials greater than 1 atm. However, piezoelectric actuators are known for their difficulty of fabrication and integration. For example, the device reported in [5] involves complicated multi-chip (9 layers) packaging.

In contrast to mechanical pumps, non-mechanical micro pumps directly convert electrical energy into fluid flow through various mechanisms including thermopneumatic electroosmotic, electrohydrodynamic, ultrasonic, magnetohydrodynamic, and electrochemical actuation. Thermopneumatic actuation has been demonstrated as an on-chip pump [7]. But the main problem is the temperature since the device needs to be heated to tens of degree in order to get just 7 kPa pressure. Much high temperature has to be sustained in order to reach just 1 atm. This limits application of thermopneumatic actuaion in the on-chip high pressure pumping for HPLC. Because of the simple fabrication and operation, electroosmosis has become the popular choice in chip-based systems [8-10]. Instead of relying on hydraulic pressure to pump the fluid, the fluid pumping is achieved and controlled by adjusting the electric field applied along the micro channels. Because of this, electroosmotic pumps can pump continuously from an open reservoir and be relatively easily integrated onto a chip. A broad range of flow rates and pressures have been demonstrated. Despite all these advantages, electroosmotic pumps have their drawbacks and limitations. Usually very high electric fields (100s of V/cm) or high voltages (1000s of V) are required to achieve appreciable flow rates. The nature of both the solvent composition [11] and the electrolyte [12] can have a strong effect on the performance of the pump. Gas formations from electrolysis or via joule heating can

effectively cause the pump to stop functioning. These problems can be alleviated by having a special membrane coated on the electrode [10, 13], however, this complicates the design and fabrication of the devices. Pressure driven reverse flow limits the pumping rate that can be achieved at high back pressures. Special modifications, such as arrays of very narrow channels [10] or channels packed with small diameter particulate supports [11, 14], are necessary for achieving the practical pressure and pumping rate that commonly used in HPLC. Although pressures as high as 8000 psi have been obtained in capillaries [15], a chip-based pumping system that utilizes the same method hasn't been developed yet mainly due to the difficulty of fabrication and integration.

5.1.2 Electrochemical Pump

Pneumatic pressure from gas formation in liquid has been utilized as the driving force in many micro pumps. Generally, there are two ways of generating gas: phase change by thermal heating of the liquid [16] and by electrochemical processes [17]. For most aqueous solutions, electrolysis is the more attractive choice because side effects due to heating of the fluid can be avoided and also the amount of power necessary is much lower. This is especially important for applications involving chemical or biological substances that are sensitive to heat or portable devices that requires low power consumption. The theoretical pressure limit for electrolysis based actuation is 200 MPa [18]. Practically and commercially, electrolysis of water has been used to generate hydrogen at pressures greater than 10 MPa. Moreover, the implementation of electrolysis pumps is very simple. All these advantages make electrolysis a very promising choice of actuation mechanism for an on-chip LC pump.

In microfluidic devices, electrolysis has been demonstrated as an actuator to deform either silicon nitride [17], parylene [19], or silicone rubber [20] membranes. For fluid pumping, a microdosing system where electrolysis generated gas was used to directly displace a sample fluid has been demonstrated [21]. By incorporating an additional electrode they were able to measure the impedance of the gas/liquid mixture and use that to accurately determine and control the volume of liquid delivered. A three-electrode nanosyringe was described by [22] that was capable of accurate and reproducible deliveries of aqueous solutions.

5.1.3 Integrated LC-ESI System

During the past few years, we have developed a multilayer parylene surface micromachining technology platform that has proven to be very versatile and flexible. Here the same technology was used again to build an integrated LC gradient pump based on the electrochemical actuation. The developed electrolysis pumps are capable of delivering aqueous and mixed aqueous-organic based solvents over a range of flow rates and pressures. The on-chip capacitive sensing that was developed previously was integrated to provide feedback for pumping. High pressure pumping capability was demonstrated. The formation of solvent gradients and the integration with an electrospray ionization source for mass spectrometry analyses were also demonstrated. To fabricate or package the various microfluidic components, such as an ESI nozzle, a mixer, and solvent chambers, into a system, several polymer micromachining technologies were utilized. Methods were developed to seamlessly integrate these different polymer materials and technologies together. Since this is the first step towards a totally

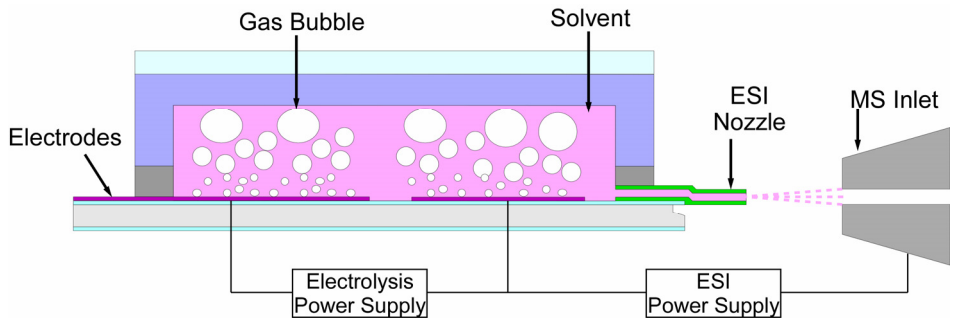

Figure 5-1 Operation principle of the electrolysis pump. An ESI nozzle is also integrated in the system.

integrated LC-ESI system, a separation column is not included in the devices described in this chapter to simplify the design, fabrication and testing.

5.2 Design and Analysis

5.2.1 Operation Principle

Figure 5-1 shows the operation principle of the electrolysis pump and its integration with an electrospray nozzle. First the pumping chamber is filled externally with solvent and sealed. A low voltage power supply provides electrical energy to electrodes located inside the pumping chamber. As current flows, gas is generated via the electrochemical reaction and raises the pressure in the chamber. This generated pressure provides driving force for the solvent pumping. For coupling our pump to a MS, an integrated ESI nozzle is integrated into the system. A high voltage power supply is applied between the ESI nozzle and the MS inlet, so the solvent being pumped out can be electrosprayed directly into the MS.

5.2.2 Electrolysis

The electrochemical reactions that occur at the surface of the electrodes of an electrochemical cell can be complex, depending on the solution components, composition

of the electrodes and the applied potential [23]. However, for cells having noble metal electrodes like Pt and aqueous working solutions, the principal process is the electrolysis of water, which produces oxygen at the anode and hydrogen at the cathode.

$$\begin{aligned} &Anode: 4OH^- - 4e^- \rightarrow 2H_2O + O_2(g) \\ &Cathode: 4H^+ + 4e^- \rightarrow 2H_2(g) \end{aligned} \tag{5.1}$$

The voltage drop V_{cell} between the two electrodes or across the whole cell can be expressed as

$$V_{cell} = E_{cell} + IR_{cell} + \eta_a + \eta_c \tag{5.2}$$

where E_{cell} is the electromotive force (emf) or the minimum voltage for the redox reaction, R_{cell} is the resistance of the bulk electrolyte in the cell, and I is the net current flowing through the cell. η_a and η_c are the activation overpotential at both electrodes and concentration overpotential due to the mass transport respectively.

For example, for a given redox reaction:

$$X + ve \rightleftarrows Y \tag{5.3}$$

E_{cell} can be obtained by Nernst equation:

$$E_{cell} = E^0 + \frac{RT}{vF}\ln\frac{C_X}{C_Y} \approx E^0 + \frac{60mV}{v}\log\frac{C_X}{C_Y} \tag{5.4}$$

where E^0 is the redox potential under standard conditions. v is the number of moles of electrons per mole of reactant reacted, F is the Faraday constant, R is the gas constant, and T is the temperature. C_X and C_Y are the activity of reactant X and product Y. At room temperature (298 K), RT/F is 25.7 mV.

For pure water, E^0 is 1.23 V. From Equation (5.4), it can be seen that E_{cell} is not very sensitive to concentration changes of X and Y in the solution. So unless the

conditions inside the cell are drastically different from standard conditions (e.g. pH <2, pH > 12, or pressure > 100 atm), E_{cell}-E^0 is normally less than ±0.6 V.

Because of the activation energy or the activation overpotential, the electrochemical cell can be treated as a switching device [24]. Unlike phase changes caused by heating, where energy has to be supplied constantly to maintain the pressure, electrical energy is needed only during pressure change in the electrolysis. This is because, in general, it is easy to design a gas-sealing chamber than a thermal-insulating chamber.

The amount of gas generated is directly determined by the amount of charge that is injected into the cell. The net current flowing through the cell, I, is the sum of the cathodic and the anodic current on each electrode, and is related to the activation overpotential through the Butler-Volmer equation:

$$I = I_0\{e^{\frac{(1-\alpha)F\eta_a}{RT}} - e^{\frac{-\alpha F\eta_a}{RT}}\} \tag{5.5}$$

where I_0 is called the exchange current and α is the transfer coefficient which is typically assumed to be around 0.5. Since the net current I is an exponential function of the activation overpotential and the gas evolution rate is proportional to I, it is preferably to use current (galvanostatic) instead of potential (potentiostatic) to control the gas generation rate.

Based on Equation (5.1), the numbers of gas molecules generated N_{H2} and N_{O2} for a given current I is given by

$$N_{H_2} = 2N_{O_2} = \frac{It}{2F} \tag{5.6}$$

where I is the current and t is the time. Then based on ideal gas law, the product of the pressure and volume of the gases, $(pV)_{H2}$ and $(pV)_{O2}$, can be obtained by

$$(pV)_{H_2} = 2(pV)_{O_2} = \frac{RT}{2F} It \tag{5.7}$$

If the hydrogen and oxygen gases are not separated, then the pressure p and volume V of the gases in the whole cell can be expressed as

$$pV = \frac{3RT}{4F} It \tag{5.8}$$

Assuming that there are no other losses or side reactions which also generate gas, the volume of liquid that is pumped out is equal the volume of evolved gases. If the pumping chamber is operated at constant pressure, then the pumping rate Q is

$$Q = \frac{dV}{dt} = \frac{3RT}{4F} \frac{I}{p} \tag{5.9}$$

If a current of 1 mA is applied, then based on Equation (5.9), the theoretical value for the maximum pumping rate at 100 atm (10 MPa) is about 100 nL/min. That would be sufficient for most LC pumping requirements. Total power consumption can be as low as 5 mW because the total voltage drop can be as low as 5 V.

One of the important figures of merit for a pump is its thermodynamic efficiency ε. It can be defined as the ratio between the work done pumping the liquid and the total electrical energy consumed:

$$\varepsilon = \frac{pQ}{IV_{cell}} \tag{5.10}$$

5.2.3 Gas Consumption

Beside leakage caused by inadequate chamber sealing, there are three ways that the generated gases can be consumed without contributing to the pressure buildup in the pumping chamber. They are: gas dissolution in solution, gas permeation through the sealing material, and gas recombination. Normally, gases have to be saturated in the

solution before bubbles can be formed. The amount of gases that can be dissolved in an ideal dilute solution follows Henry's law:

$$C_{gas} = K_{gas} p_{gas} \tag{5.11}$$

where K_{gas} is the Henry's law constant for the gas, p_{gas} is the partial pressure of the gas, and C_{gas} is the concentration of the gas in the solution. At room temperature, K_{gas} for hydrogen and oxygen are 0.0013 mol/(kg·atm) and 0.00078 mol/(kg·atm) respectively. The volume ratio of hydrogen and oxygen dissolved in water under 10 atm pressure are 0.30 and 0.18 respectively.

Gas permeation depends on the material used in the structure. To study the effect of different materials on the gas permeation, the gas permeabilities for each of these materials needs to be known. The gas permeability P_{per} for a sealing material is defined by

$$P_{gas} = \frac{\Delta V}{\Delta t}\frac{L}{pA} \tag{5.12}$$

where p is the pressure difference across the sealing, L is the permeation length of the sealing, A is the area, $\Delta V/\Delta t$ is the volume permeation rate.

Possible material candidates include parylene, SU-8, and PDMS. Parylene is known to be a good gas and moisture barrier. SU-8, a type of expoxy, is similar to parylene in terms of gas permeability. On the other hand, PDMS is known for its large gas permeability. The permeabilities of PDMS for O_2 and H_2 under room temperature are around 15 nL·mm/mm^2·min·atm. This is roughly two orders of magnitude larger than those of parylene and SU-8, so in our chip, where PDMS is used as a gasket to provide sealing, the gas permeation will be mostly dominated by diffusion of gas through PDMS.

When considering the electrolysis of water, there is always recombination of hydrogen and oxygen gas into water, especially in the presence of Pt which is a very good catalyst for the recombination. Like any chemical reaction, the recombination rate is directly related to the concentrations of gases inside the solution which increase with pressure according to Henry's law. Unfortunately, so far, no simple analytical model has been found in the literature that can describe the recombination rate, especially in the presence of catalyst.

5.2.4 Electrolysis Pump Design

A typical nano-LC binary solvent gradient has a total flow rate of 100 nL/min and a duration of 30 min. This results in a total solvent volume of 3 μL, split evenly between our aqueous and organic solvent. To accommodate such a volume on a chip, both PDMS and SU-8 structures are used. A 200 μm recess in the PDMS mold combined with 100 μm high SU-8 structure will give 300 μm depth as shown in Figure 5-1. The area of the pump on the chip surface will be 1 mm wide and 10 mm long. Thus, it was possible to have two 3 μL pumps on a 1 cm x 2 cm chip and still leave room for other components.

For the electrodes design, an interdigitated configuration is chosen. The main reason for this is to reduce the bulk resistance, R_{cell}, thereby also reducing the voltages necessary for electrolysis. Decreasing the bulk resistance also reduces undesired joule heating of the fluid, which decreases pumping efficiency. R_{cell}, the resistance of the bulk electrolyte in the cell, is given by

$$R_{cell} = \rho\kappa \tag{5.13}$$

where ρ is the specific resistivity of the electrolyte and κ is the cell constant. For interdigitated electrodes that have equal finger space s and finger width w and the number of the figures >> 1, the cell constant κ is given by

$$\kappa = \frac{2(s+w)}{w_c l_c} \tag{5.14}$$

where l_c is the total length of the interdigitated electrodes, w_c is the length of each finger. Here, s and w are 50 μm. If l_c is 5 mm and w_c is 1 mm, then κ becomes 0.4 cm^{-1}.

Usually, in HPLC, the mobile phase consists of water, an organic solvent, and an electrolyte such as formic acid. The specific resistivity of a mixed aqueous/organic solution is higher than that of aqueous solution for the same electrolyte concentration. ρ for water/acetonitrile/formic acid (50:50:0.1 by volume) solution, like those commonly used in RP-HPLC, is about 8 kΩ·cm. Then the estimated R_{cell} is 3.2 kΩ and IR_{cell} is 3.2 V for 1 mA current. These values can be easily handled by common IC circuit with a power supply less than 15 V.

On the other hand, typical thickness of the Nernst diffusion layer is on the order of 0.1 mm. With the space between the cathode and anode approximating that thickness, mass transport is greatly enhanced which leads to the reduction of the concentration overpotential η_c. Although this will also enhance the recombination since H_2 and O_2 gases are not separated, it can be beneficial. A binary solvent gradient requires one of the solvents pumping rate to decrease while the other increases. Besides the gas permeation and the liquid pumping itself, there is no other way to bleed the pressure inside the pumping chamber. The enhanced recombination can speed up the pressure releasing while compromising the electrolysis efficiency.

The ESI nozzle is very similar to the one that was previous demonstrated by our group [25]. Overhanging distance of the nozzle is about 1 mm. The tip orifice is about 5 μm high and 20 μm wide, and the curvature of the very end is about 1-2 μm. The channels that connect both pumping chambers and the nozzle are 5 μm high and 100 μm wide.

5.3 FABRICATION

The diagram of the integrated system is shown in Figure 5-2. There are three main components. First, an ESI nozzle, a mixer, and electrolysis electrodes are integrated on a silicon substrate. The silicon substrate is planarized using a thick SU-8 layer which creates a flat surface for the PDMS piece to sit on. The second component is a molded PDMS piece that serves as the solvent chamber and sealing gasket. The recessed PDMS and SU-8 together define the total volume of each pumping chamber. The third piece is a glass cover, which is used to clamp the PDMS piece in place. To use the chip, first the PDMS cover is placed on the SU-8 planarized chip substrate. The adhesion between the PDMS and the SU-8 is adequate for filling the chambers with solvent using a syringe. Once the solvent chambers are filled, the PDMS piece is clamped down using the glass

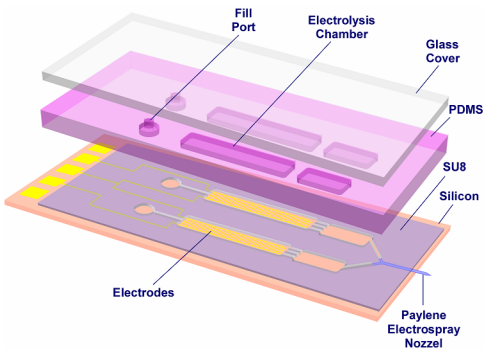

Figure 5-2 The diagram of the integrated system having various components made from several polymers.

cover to ensure the solvent chambers are sealed. Clamping force and electrical connection to the chip are provided by a custom-made jig.

5.3.1 Fabrication Process

The detail fabrication process is shown in Figure 5-3. The process began with a 4-inch silicon wafer with 1.5 µm of thermally grown oxide. Electrolysis electrodes were made of thermally evaporated gold/titanium (200 nm/10 nm). Initially, gold/chrome was tried. But testing showed the chrome adhesion layer could be easily attacked during the electrolysis.

After patterning the electrodes, the front side oxide was patterned using buffered HF. In order to promote adhesion between the silicon substrate and the succeeding parylene layer, short XeF_2 (10 sec, 0.6 Torr) (Pelchem, Pretoria, South Africa) dry etching was performed to roughen the exposed silicon surface. Two layers of 4.5-µm parylene (Uniglobe Kisco, Inc., San Jose, CA) with a 5.5-µm sacrificial photoresist in between formed an ESI nozzle, a passive mixer, as well as the channels that connect the mixer to the solvent chambers. A 150 nm sputtered aluminum layer was used as a mask for parylene etching to define the shape of the nozzle. The Al was later removed by wet

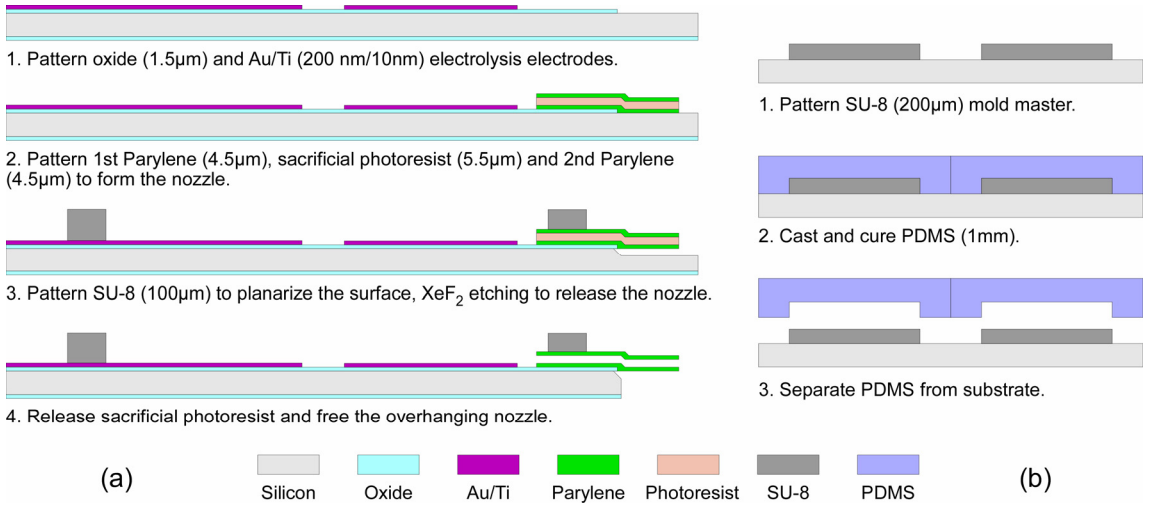

Figure 5-3 The fabrication process of the devices. (a) Process flow of the chip with ESI nozzle. (b) PDMS cover process.

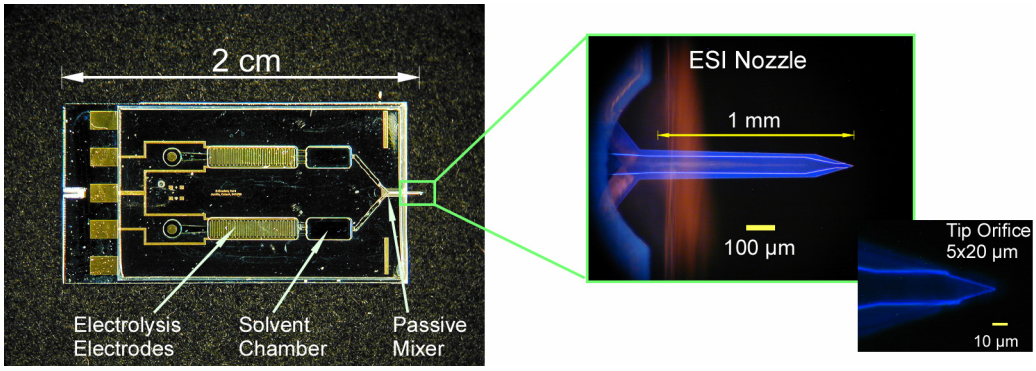

Figure 5-4 The photomicrograph of the fabricated electrolysis pump integrated with ESI nozzle.

etching. Wafers then went through a 5% HF dip and oxygen plasma cleaning before a 100 µm SU-8 layer (Microchem, Newton, MA) was spin-coated on. The SU-8 layer was patterned and served to provide a flat overall chip surface to support the PDMS gasket. After SU-8 developing, wafers were left inside the SU-8 developer (propylene glycol monoether acetate, PGMEA) for two days to release the photoresist. After the photoresist had been dissolved, a 100 µm deep anisotropic XeF_2 (five to six 1.5 min 3 Torr loops). Etching was used to undercut the nozzle and make it freestanding. Wafers were then diced into 1 × 2 cm chips. A photomicrograph of the fabricated device is shown in Figure 5-4

Au, Ti and Al metals were purchased from Williams Advanced Materials (Brewster, NY). Au and Al etchants and buffered HF were purchased from Transene Inc. (Danvers, MA). All photoresist materials were purchased from Clariant (Somerville, NJ).

The pump chamber was formed using a 1-mm gasket with indentations corresponding to the pattern SU-8. These were made using poly(dimethylsiloxane) (PDMS) (Sylgard® 184 from Dow Corning, Midland, MI). To create these, PDMS was poured onto a 200 µm high master mold fabricated from SU-8 to create the indentations

that also increased the volume of the pump chambers. The total volume of each pumping chamber is 3 μL.

To facilitate characterization of electrochemical pumping, a testing chip that replaced the ESI nozzle with a meandering metering channel was also fabricated. For this chip, a glass substrate was chosen and the steps related to the Parylene structural layer and photoresist sacrificial layer were omitted. E-beam evaporated Platinum/Titanium (200 nm/ 30 nm) is used for the electrolysis electrodes instead of Gold/Titanium. Heated (~70°C) Aqua Regia (HNO_3:HCl=1:6) was used for Pt/Ti etching. The Pt/Ti electrodes extended the length of the chamber. An additional pair of electrodes was placed between the cathode and anode. It could be used to measure the change in capacitance due to changing gas/liquid ratio as solvent was pumped from the chamber. A serpentine channel (250 μm(H) x 500 μm(W) x 15 mm(L)) extending from the junction of the pump channels to the edge of the chip was patterned in the SU-8 layer and PDMS cover. Pt/Ti lines spaced 200 μm apart were patterned under the metering channel. These marks were used to determine flow rates by observing the movement of the air-liquid interface. Picture of the fabricated testing chip is shown in Figure 5-5.

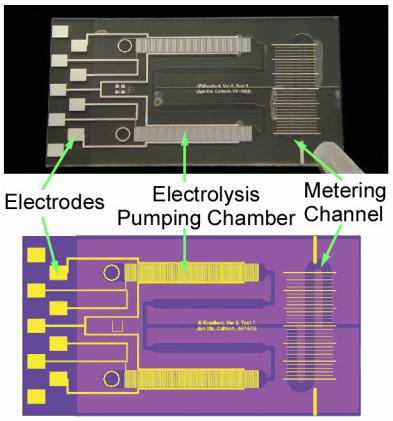

Figure 5-5 The photomicrograph of the fabricated testing chip with electrolysis pump and metering channel.

5.3.2 Issues with SU-8 Process

Several process steps required extra attention. First, since cross-linked SU-8 films are highly stressed, serious cracking in the underlying parylene structures can occur if these structures coincide with the edge of the SU-8 layer. SU-8 shrinkage was measured to be around 2% after post exposure baking (PEB). To solve this, baking steps for the SU-8 are carried out under much lower temperatures (10 min at 60-70 °C) and slower ramping speeds (2 °C/min) than the manufacturer guidelines suggested values (10 min at 90 °C, ramping > 10 °C/min). Figure 5-6 gives some pictures that show the effect of changing PEB baking temperature on the parylene cracking at the SU-8 edges.

The presence of SU-8 also limited the solvents that could be used in photoresist releasing. Acetone, which is generally used to dissolve away sacrificial photoresist, caused large volume change of the SU-8 layer. This resulted in serious problems such as cracks or delamination of the SU-8 from the substrate. So instead of acetone, mild solvents such as PGMEA, isopropanol, or ethanol were used. One side effect of this substitution was a longer photoresist dissolution time.

This may be due to weaker solvent strength and/or slower diffusion of the dissolved photoresist. For a spherical particle of radius a in a solvent of viscosity η, according to Stokes-Einstein relation and Stokes relation, the diffusion constant of the particle in the

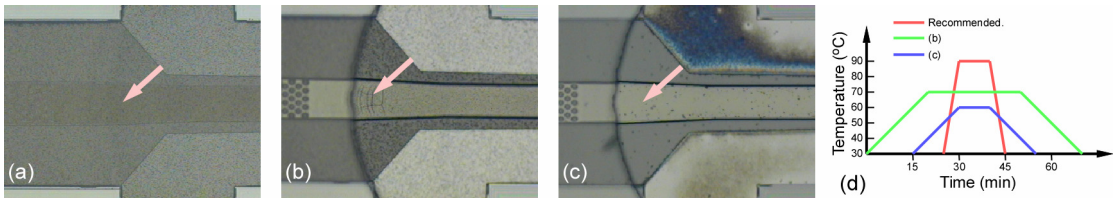

Figure 5-6 The effect of different SU-8 PEB on the parylene structure. (a) Picture after PEB and before developing. (b) Picture of parylene cracking after 30 min 70 °C PEB. (c) No parylene cracking after 10 min 60 °C PEB. (d) PEB temperature profiles that used. Baking profile recommended by manufacturer is also included.

solvent, D, can be expressed as

$$D = \frac{kT}{6\pi a\eta} \tag{5.15}$$

where k is the Boltzmann constant and T is the temperature. At 298 K, viscosities of isopropanol and ethanol are 2.3 and 1.2 mPa·s respectively while the viscosity of acetone is 0.32 mP·s [26]. For the same molecule, the diffusion constant can be 4 times smaller in ethanol than in acetone.

5.4 EXPERIMENTAL RESULTS

5.4.1 Testing Setup

To prepare the chip for use, the chip and PDMS gasket were manually aligned and placed in a custom-made Acrylic holder. Filling/venting ports located at either end of the pump and solvent chambers were punched through the PDMS gasket. Stainless steel syringe needles (400 μm O.D., Hamilton Co., Reno, NV) were inserted through the holes in the PDMS layer and fluid was injected into the pump. The gas venting holes at the opposite end of the chamber ensured complete filling. After filling, a glass cover was placed and clamped on top of the PDMS cover to seal the chamber. An array of Pogo® contacts (Everett Charles Technologies, Pomona, CA) mounted inside the top piece of the acrylic holder provided robust electrical contact to the electrode pads on the chip. After use, both the PDMS gasket and the chip could be cleaned with IPA and reused several times.

Electrolysis pumps were galvanostatically controlled using output currents from custom-built voltage to current converters. Full-scale current range was normally 1 mA and it was adjustable. The voltages were programmed in LabView and were fed to the

converters through a DAQPad-6020E interface board from National Instruments (Austin, TX).

To measure pumping flow rates in the testing chip equipped with the metering channel, the assembled structure was placed under a microscope of a probe station (Micromanipulator, Model 6000, Carson City, NV) equipped with an Hitachi (Model KP-D20BU) CCD video camera. Movement of the air-liquid interface through the metering channel was recorded. The time required to displace a given volume, as measured by the marks of the metering channel, provides the data needed to calculate a flow rate.

5.4.2 Pumping Testing

The performance of the electrochemical pumps was first characterized under low back pressure (<1 kPa) using the chip that doesn't have nozzle. Measurements of the pumping rate as a function of applied current were obtained and the results are shown in Figure 5-7. A common LC solvent composition (water/acetonitrile/formic acid, 95:5:0.1 by volume) was used as the electrolyte. Pumping rates ranging from 40 to 190 nL/min were observed for currents between 16 and 41 μA with power consumptions less than 100 μW. Operation in the current range of 27 and 41 μA yields almost linear response in displaced volume, as shown in Figure 5-7. At lower currents, 16.1 and 22.1 μA, the rate of gas generation increases with time. For example, the observed flow rate at 16.1 μA ranged from 25-60 nL/min over the 50 min the test was conducted.

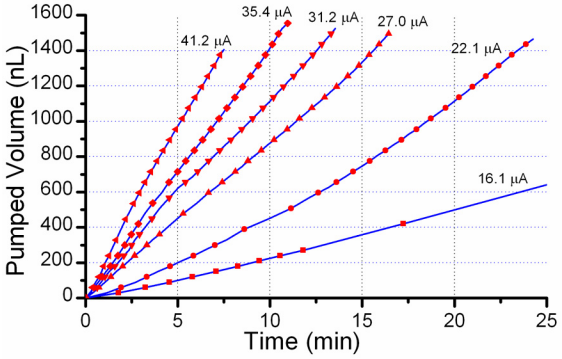

Figure 5-7 The pumped volume vs. time under different current. The pumping rate is a function of applied current.

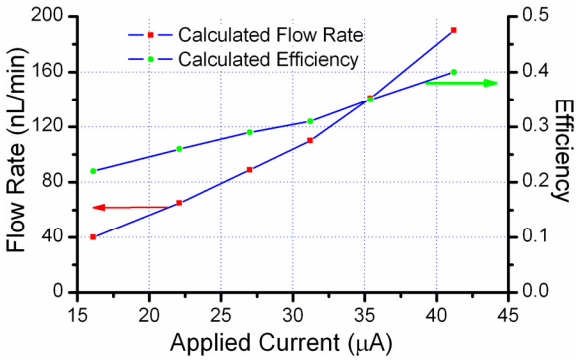

Figure 5-8 Calculated flow rate and electrolysis efficiency as a function of applied current.

In an ideal electrolysis system, the volume of gas produced is proportional to the applied current. In reality there are losses due to recombination of hydrogen and oxygen, joule heating, gas dissolution in the liquid, gas permeation through the PDMS layer, and other electrochemical reactions besides electrolysis. The relationship between the pumping rates and applied currents, as can be seen in Figure 5-8, is decidedly non-linear. An efficiency value was calculated by dividing the volume of the liquid displaced with the calculated volume of gas that would be generated from the electrolysis of pure water without any losses according to Equation (5.9). The calculated efficiency increased from 0.22 to 0.40 going from 16.1 µA and 41.2 µA.

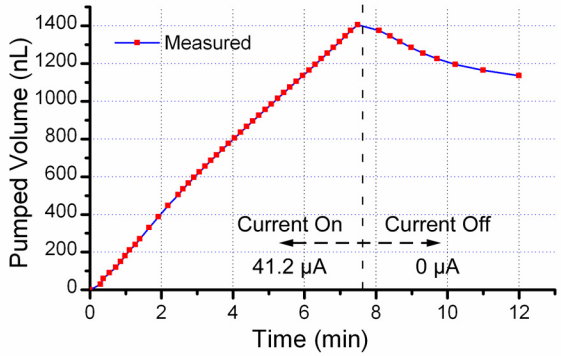

Figure 5-9 Loss of gas after the applied current was turned off at min 8.

Loss of gas by leakage from the chamber or from recombination was clearly evident when the current was turned off. The gas bubbles began to shrink and liquid was pulled back into the chamber as indicated by Figure 5-9. Because the end of the channel is open to atmosphere, solvent evaporation makes it difficult to measure very small flow rates accurately. For currents <10 µA, little or no gas bubble formation was observed so that the corresponding flow rates are too small to be measured accurately.

Tests were also done to show how the pumping rate responds to changing applied current. The results are shown in Figure 5-10. A linear current profile was applied and current dropped from 41 µA to 0 µA in 10 min. Figure 5-10 also shows the corresponding

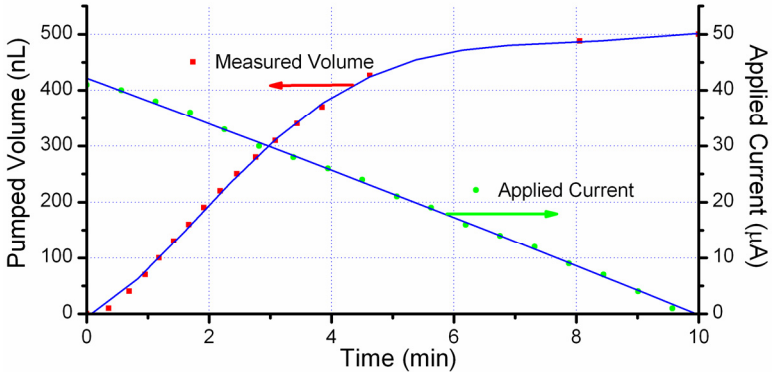

Figure 5-10 Pumped volume as a function of time when a linearly decreasing current was applied to the electrolysis pump.

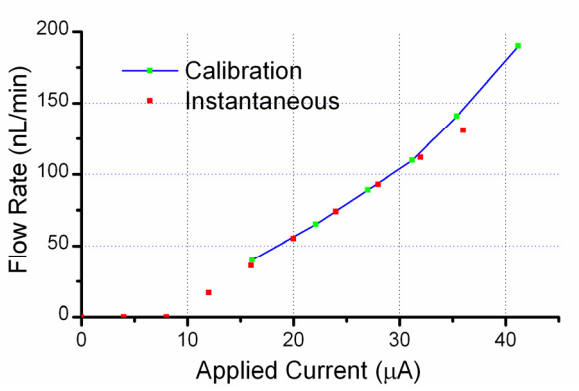

Figure 5-11 Instantaneous flow rate vs. applied current. The calibration curve is also plotted here.

pumped volume.

Instantaneous flow rate was calculated from the slope on the pumped volume vs. time curve. The instantaneous flow rate vs. the instantaneous current was plotted in Figure 5-11 against the calibration curve that was obtained previously. Except for the high current which was applied in the very beginning of the pumping, and the currents that are lower than 10 μA, the middle section overlapped very well. This indicates that it is feasible to use calibration data to deduce a control current profile for a given solvent gradient.

5.4.3 Pumping under Back Pressure

Since most LC separations are done under high pressure due to the densely packed column, it is very important to test the capability of the pump at elevated back pressure. The testing setup is illustrated in Figure 5-12 is different than that of the low pressure testing. Some of the testing chips were fabricated without SU-8 on the top surface. A 1 mm thick PDMS gasket with an 8 mm×8 mm square hole in the center was used to create a chamber above the testing chip. The chamber was filled with a solution of water/acetonitrile/formic acid (90:10:0.1 by volume) and sealed with an acrylic cover

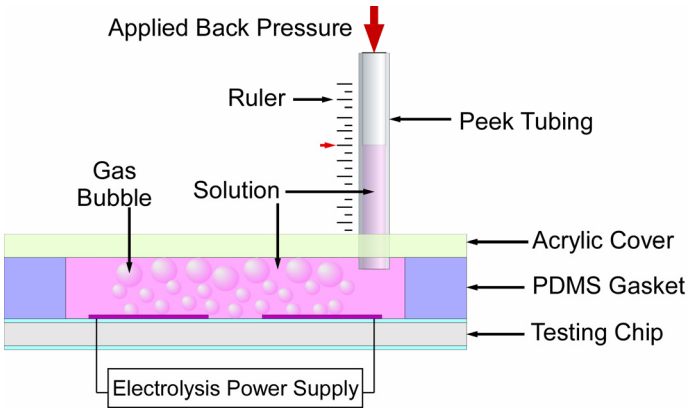

Figure 5-12 Testing setup for high back pressure pumping.

plate (2.5 mm thick). To make the measurement easier, green food color was added in the solution. A PEEK tube (510 µm O.D. × 255 µm I.D.) was connected to the chamber through the cover at one end and to an air pressure source equipped with a control valve and pressure regulator at the other end. The wall of the PEEK tubing was sufficiently translucent that movement of the colored liquid out of the pump chamber could be monitored.

Pumping rates were measured at back pressures ranging from 138 to 552 kPa and with electrode currents ranging from 50 to 200 µA. The results are shown in Figure 5-13. As expected, the current needs to increase to get the same flow rate when the back

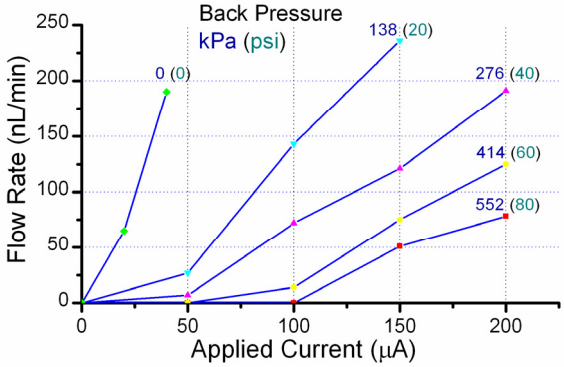

Figure 5-13 Flow rate vs. applied current at various back pressures.

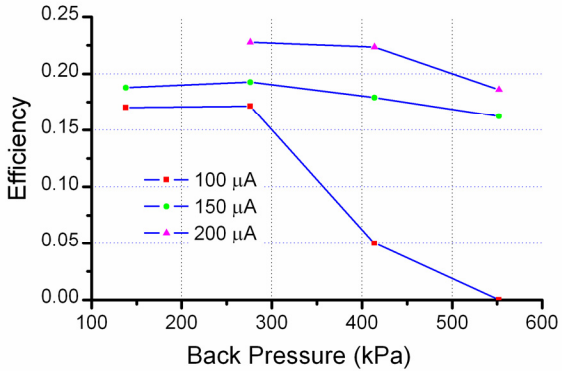

Figure 5-14 Efficiency of electrolysis at high back pressures.

pressure increases. Similarly, for a constant current, the flow rate drops as the back pressure increases.

An electrolysis efficiency value was calculated by dividing the measured flow rate with the flow rate calculated from Equation (5.9). The result is shown in Figure 5-14. The observed trend is very similar to previous result of low back pressure. For the same back pressure, the efficiency increases as the current increases. For the same current, the efficiency decreases as the back pressure increases. This is expected because, according to the Henry's law, the dissolved gas concentrations increases with the elevated pressure. Then, like any chemical reaction, the recombination of H_2 and O_2 into H_2O becomes faster when the gas concentrations are larger. This counteracts the pressure buildup from gas generation of electrolysis.

Tests were also performed using another modified setup where the chip was sealed in a solvent filled 1.5-mL plastic sample vial with epoxy. This setup allowed us to increase the back pressure up to 14 atm before it finally failed. The number of gas bubbles generated in a given duration was counted and bubble sizes were estimated. Although this is not an accurate way to measure flow rate, it serves the purpose of a

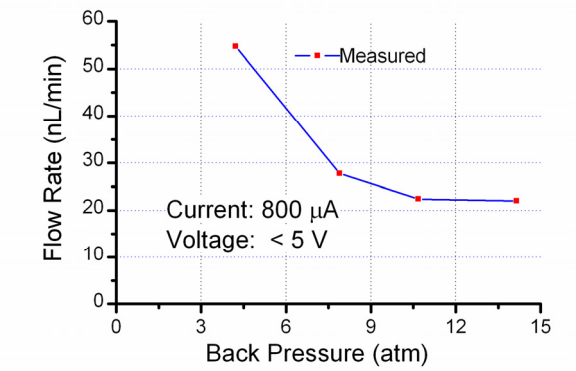

Figure 5-15 Electrolysis calibration at a constant current of 800 uA at various backpressures.

rough estimation. The result is shown in Figure 5-15. A flow rate of 20 nL/min was achieved at 14 atm with an 800 μA current and a voltage less than 5 V. Since the total power consumption is still rather small, we expect that high flow rates can be achieved by simply increasing the current. Also, these tests confirm that the electrolysis pump can meet the pumping specifications (e.g. flow rate and pressure requirements) normally required for capillary or micro-scale HPLC. Previously good chromatography on both monolithic and particulate reverse phase supports was demonstrated at pressures < 50 psi [27].

Based on Equation (5.10), the thermodynamic efficiency ε of the pump was calculated. For the pumping rate of 75 nL/min at a pressure of 80 psi that was obtained with 200-μA current and less than 5-V voltage, ε is 0.069%. It is two times bigger than the thermodynamic efficiency of the planar electroosmotic pump of Chen and Santiago reported [28], which is 0.035%. Their pump used a single channel 0.9 μm deep 38 mm wide and 1 mm long. It was operated at a 3,000 V and 7 μA and had a maximum pressure capacity of only 1.5 atm, although measured flow rates at lower pressures were quite high (~830 nL/min at 1 atm). The multiple open-channel pump of Lazar and Karger reported

[10] yielded a flow rate of 17 nL/min at a pressure of 80 psi using an array of one hundred 2.5 μm × 3 cm channels and an applied potential of 3000 V. It can be clearly seen, the performance of the electrochemical pump compares favorably with previously reported chip-based electroosmotic pumps.

Recent work done in capillaries suggests that adequate performance can be achieved using electroosmotic pumps if the fabrication challenges can be met. For example, in the electroosmotic pump reported by Chen [11], a 17.5 cm x 100 μm ID capillary packed with 2-3 μm porous silica spheres yielded a flow rate of 100 nL/min with an applied potential of 5000 V and a pressure of 500 psi. However, the required high voltage could seriously limit its application.

The electrochemical pump shown here required less than 5 V while operating at 200 μA, which means the power consumed was only about 1 mW. The overall heating effect caused by this amount of power consumption on the chip system is not significant. The estimated temperature increase of the system compared to the ambient is less than 1 °C. Of course, the local heating effect can still impose problems if not considered carefully. In the pump design, the electrolysis electrodes are uniformed distributed around the chamber to facilitate the heat dissipation.

5.4.4 Gradient Generation

The capability of gradient formation was first demonstrated using the testing chip. To visualize the gradient composition, one pump chamber (A) was filled with a solution containing green dye to distinguish it from the colorless solution in the other pump chamber (B). The base solution was water/acetonitrile/formic acid (90:10:0.1 by volume). As the applied current ratio between the two pump chambers was varied, the

corresponding change in the amount of fluid flowing into each arm of the T junction from each pump chamber was monitored with a microscope equipped with a video camera. The captured images were then analyzed to obtain quantitative information about the gradient.

The image processing and analysis process are illustrated in Figure 5-16. The original colored image, Figure 5-16(a), was converted to 8-bit (256-level) grayscale image. Then the grayscale image was converted to binary (B&W) image Figure 5-16(b) using a middle value as threshold. The middle value was the average of intensities of region A (solution A) and region B (solution B) in Figure 5-16(a). Following the conversions, the converging region of the two streams was extracted for image analysis. One example is shown in Figure 5-16(c). The average intensity of the green window is proportional to the flow rate ratio between two streams. The average intensity of the confluent region was determined using software Scion Image (Scion Corporation, Frederick, MD). Results were expressed as the concentration of each solution in the confluent flow.

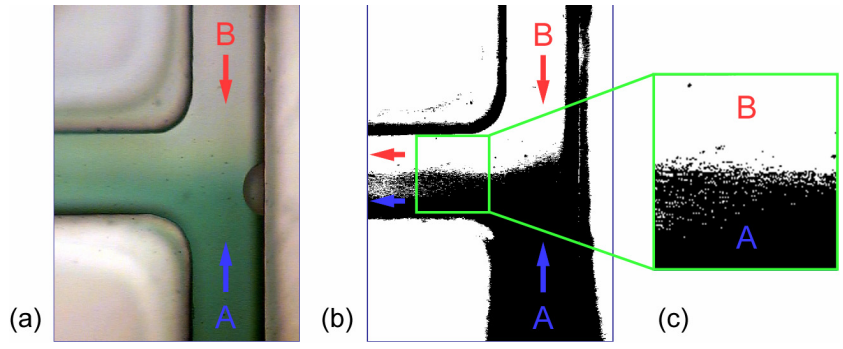

Figure 5-16 Image processing and analysis for the composition measurement of the gradient formation. (a) Original color image. (b) Converted black & white image. (c) Zoom-in image.

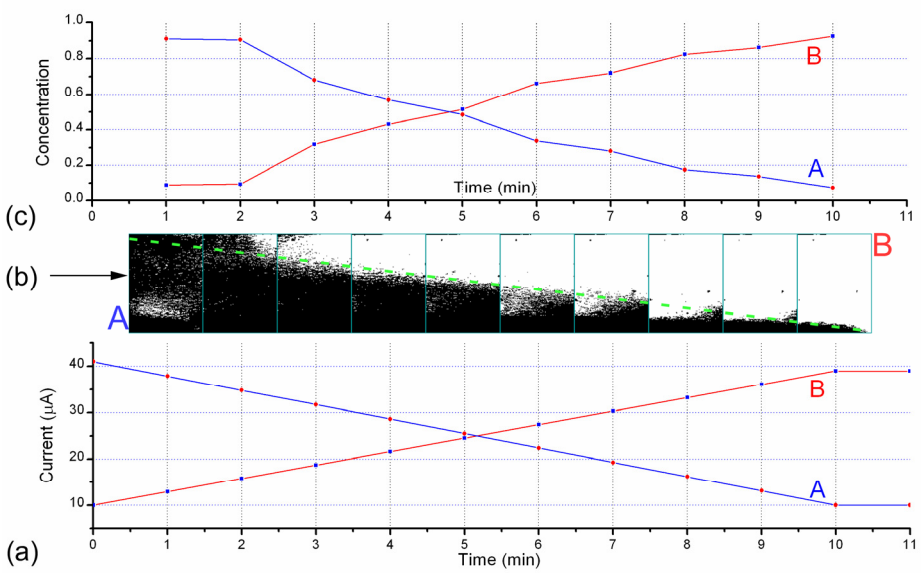

Figure 5-17 Results for the gradient formation. (a) Applied current profile. (b) Final processed images of confluent junction at indicated moment. (c) Measured result of the gradient formation.

The measurement results for the gradient formation are shown in Figure 5-17. Figure 5-17(a) shows the linear gradient profile of the applied currents to both pump chambers. Figure 5-17(b) and (c) are the final processed images of confluent junction. These images were taken at 1-min intervals. Also plotted is the concentration of each component corresponding to these analyzed images. As expected, the concentration of each component in the gradient follows the profile of the corresponding control current closely except for the beginning.

The results also illustrate some of the difficulties of forming gradients on this scale. It is difficult to establish initial conditions because pressurizing pump A results in some movement of fluid into the channel connected to pump B. This has to be cleared before the effect of flow from pump B is evident in the junction where the two solvent streams come together. Thus, there is a delay evident in the curves shown in Figure 5-17(c). A pump current of approximately 10 μA is needed to overcome gas losses resulting from

leakage or recombination. So the baselines of the control currents are set to 10 μA, instead of zero.

5.4.5 MS Analysis

After the gradient was successfully demonstrated using the testing chip, a similar experiments was performed on the chip that has the integrated ESI nozzle. The integrated ESI nozzle allows for direct MS analysis of the sample solution pumped out of the chip. All measurements utilized an Agilent LC/MSD ion trap mass spectrometer operating in the positive ion mode. A platform equipped with a three-axis stage was mounted in front of the instrument to replace the standard electrospray assembly. The chip electrospray nozzle was positioned on axis to within a few mm of the faceplate of the atmospheric pressure ion source. A Zeiss Stemi SV8 microscope equipped with a Hitachi HV-C20 video camera was used to monitor bubble formation, fluid flow, and electrospray from the chip. Video data was recorded using a Pinnacle Systems (Mountain View, CA) AVDV capture card.

For electrospray stability measurements, a 25 pmole/μL solution of gramicidin S in water/acetonitrile/formic acid (90:10:0.1 by volume) was infused using the on-chip ESI nozzle and electrolysis pump. The flow rates ranged from 50 to 1000 nL/min and were estimated by monitoring the size of the bubbles in the pump chambers. For comparison purposes, the same sample solution was infused at a flow rate of 150 nL/min using a commercial pulled fused silica nanoelectrospray nozzle (8 μm tip opening, New Objective, Woburn, MA) connected to a syringe pump (Model 100, KD Scientific, New Hope, PA).

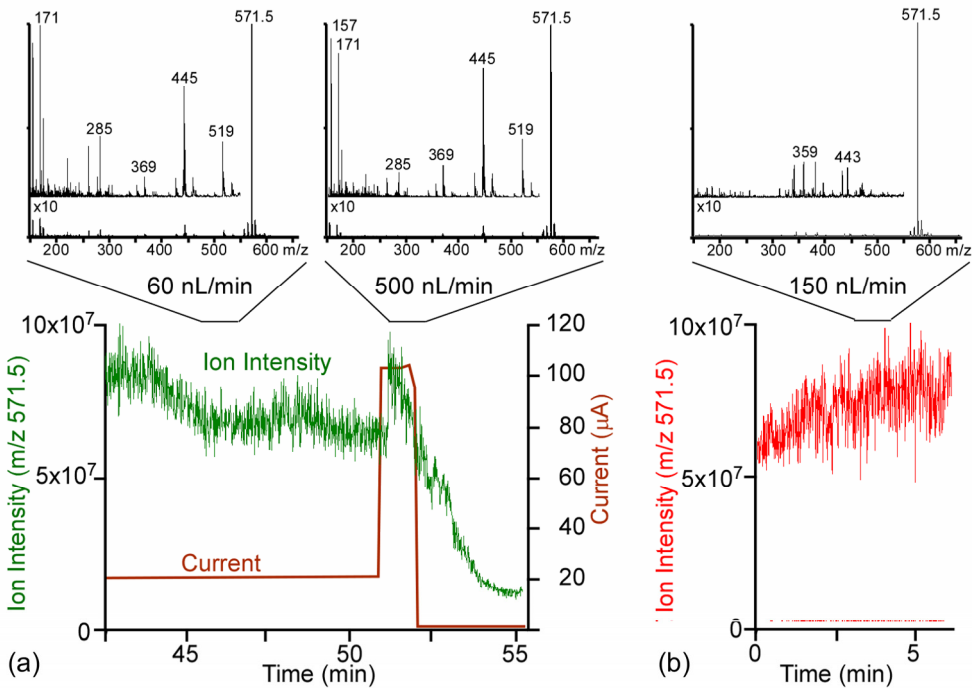

Figure 5-18 Electrospray stability testing results. (a) Data from the chip with ESI nozzle. (b) Data from the commercial ESI nozzle.

Figure 5-18 shows the results. When a solution of gramicidin S (m/z = 571.5) was infused using the on-chip ESI nozzle and electrolysis pump, stable emission was obtained for extended times over a broad range of flow rates (50 – 1000 nL/min). The details including the current profile of the last 12 min of a run lasting about one hour are shown in Figure 5-18(a). Under normal electrospray conditions, signal intensity is a function of sample concentration not flow rate, and the very similar spectrum was obtained at either 60 nL/min or 500 nL/min. Equivalent results, shown in Figure 5-18(b), were obtained with a standard syringe pump infusing the same sample solution through a pulled fused silica nozzle.

A characteristic set of background ions was present in the low mass (< 550 m/z) regions of the spectra obtained using the electrochemical pump. We have determined that these components were derived from the SU8 and PDMS layers of the chip by

extracting bulk material with acetonitrile and analyzing the solution by electrospray MS with clean fused silica nozzle. The solvent compatibility of PDMS has been studied in some detail [29], but no similar study has been made with respect to SU8. It should be possible to eliminate the contamination by coating those surfaces with an additional layer of Parylene or thoroughly extract the contamination, mainly oligomers or additives, by solvent rinse. PDMS and SU-8 were chosen here mainly due to their fast prototyping capability. Other materials can be utilized if contamination issue is utterly important, as might be the case in HPLC.

For gradient formation experiments, two pump chambers were filled with different samples, so that the MS can differentiate the flow from each pump. One pump chamber was filled with a solution of 25 pmole/μL angiotensin in water:methanol:formic acid (95:5:0.1) and the other pump was filled with a 10 pmole/μL solution of tetrabutylammonium iodide in water/acetonitrile/formic acid using either 90:10:0.1 or 50:50:0.1 solvent ratios. The relative concentrations of the two components spraying from the chip were determined from the ion intensities at m/z 242.1 (tetrabutylammonium ion) and 432.8 (MH_3^{3+} of angiotensin). The results are shown in Figure 5-19. As the current delivered to each pump was changed according a profile shown in Figure 5-19(a), there was a corresponding change in the intensity of MH_3^{3+} of angiotensin (m/z 432.8) and the tetrabutylammonium ion (m/z 242.1) shown in Figure 5-19(b). Three representative spectrums at the time indicated were shown in Figure 5-19(c). The control current profile was set to be parabolic based on the calibration results. Ion intensities were normalized to relative abundance in the final results.

There were three gradient sections in Figure 5-19 and the average flow rate was about 100 nL/min. To prime the system, at the beginning of the run, pump B was activated briefly to pressurize the system and remove any solvent from pump A that might have been in the channel to pump B as a result of filling the pump chambers. Pump A was then turned on at the maximum current chosen for the experiment while pump B

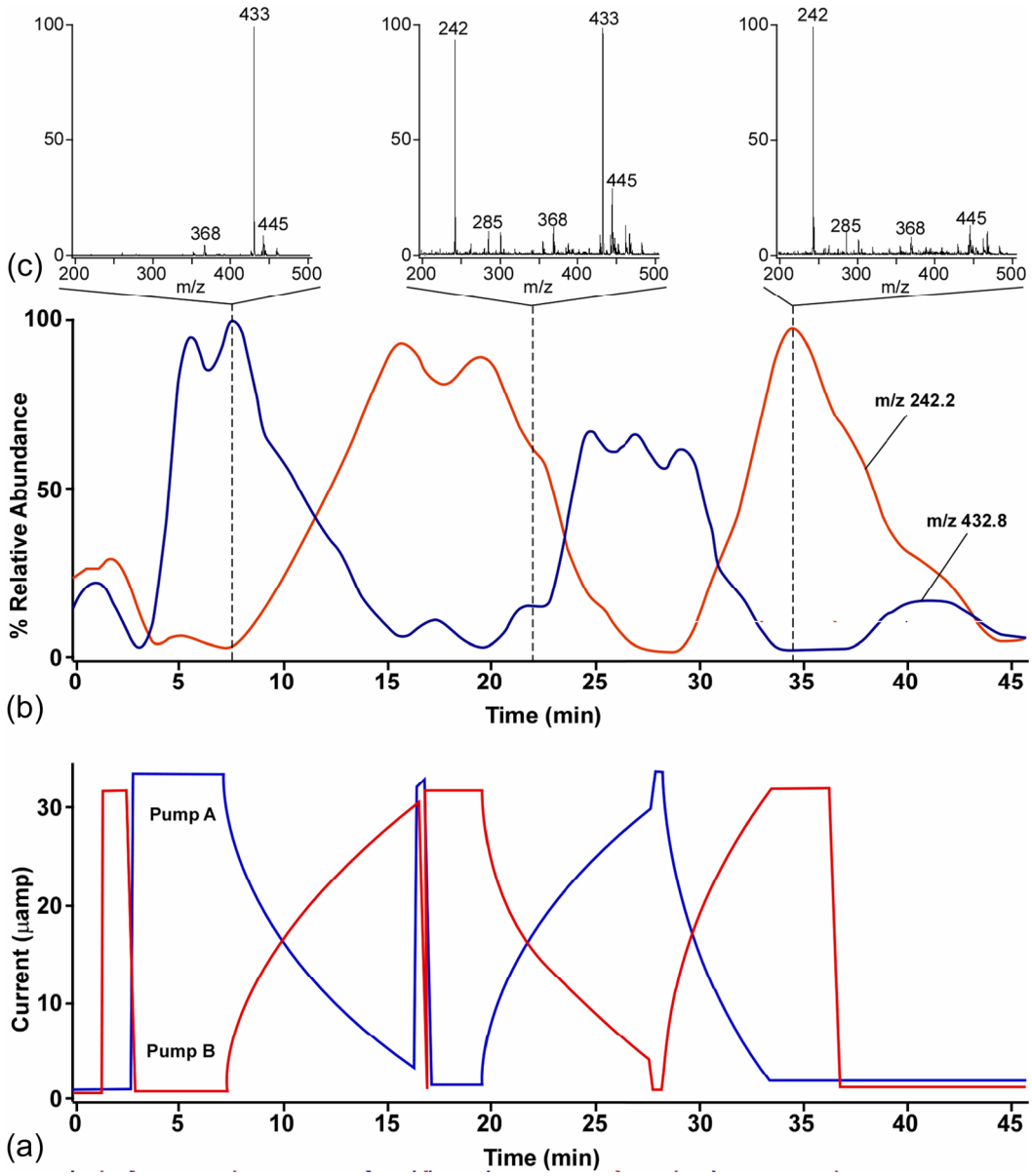

Figure 5-19 Results for the gradient formation. (a) Applied current profile. (b) Final processed images of confluent junction at indicated moment. (c) Measured result of the gradient formation.

was set to zero. When the contribution from solvent B was no longer evident in the mass spectra (7.5 min), the current to pump A was decreased with a corresponding increase in the current from pump B. This is the first gradient section. At 19.5 min when solvent A was no longer evident in the spectrum, the current in pump B was decreased with a corresponding increase in the current to pump A. This is the second gradient section. A final gradient going from 100% A to 100% B was formed after which both pumps were turned off. Residual pressure in each pump chamber continued to push sample into the electrospray nozzle for several minutes.

Although the control of the gradient formation is not very precise and the inherent instability of the electrospray source makes it difficult to accurately track the solvent composition, the data is sufficient to show that the solvent composition is responsive to the programming of the pumps over a time frame and flow rate relevant to LC separations. Similar results were obtained when one of the pump chambers contained 50% acetonitrile. In the future, more precise gradients can be achieved by feeding back either the signal from the capacitive sensors in the pump chambers, or from microscale flow sensors presented in Chapter 4 that could be built into the outlet channel for each pump.

5.5 CONCLUSIONS

The electrochemical pump presented in this chapter offers several advantages for microfluidic applications. It can deliver aqueous and mixed aqueous-organic solvents at a broad range of flow rates. Also this pump is able to deliver significant flow rates at very high back pressures, a necessity for applications in HPLC. The highest pressure, under which pumping was demonstrated, is 200 psi and this was limited by the capabilities of

the testing setup. With a more robust setup and packaging, pumping at higher pressures should be easily attainable. Most importantly, the demonstrated pumping capabilities are sufficient for many chromatographic separations. By combining the output of two pumps, solvent gradients can be formed. The pumps operate at low currents (< 1 mA), low voltages (< 5 V) and consume little power (< 5 mW) even when pumping at higher pressures.

The pumps can be integrated with other microfluidic components, especially those that are made from multilayer parylene technology, and the fabrication process is suitable for mass production. One disadvantage that should be noted is that each pump is a closed system so recirculating flow or suction is hard to achieve, if not impossible. Further work is needed to improve flow rate regulation and to reduce the chemical background that might limit application in biological and chemical analysis.

REFERENCES:

[1] T. Laurell and G. Marko-Varga, "Miniaturisation is mandatory unravelling the human proteome," *Proteomics*, vol. 2, pp. 345-351, 2002.

[2] C. M. Harris, "Shrinking the LC landscape," *Analytical Chemistry*, vol. 75, pp. 64a-69a, 2003.

[3] D. R. Reyes, D. Iossifidis, P. A. Auroux, and A. Manz, "Micro total analysis systems. 1. Introduction, theory, and technology," *Analytical Chemistry*, vol. 74, pp. 2623-2636, 2002.

[4] N. T. Nguyen, X. Y. Huang, and T. K. Chuan, "MEMS-micropumps: A review," *Journal of Fluids Engineering-Transactions of the Asme*, vol. 124, pp. 384-392, 2002.

[5] D. C. Roberts, H. Li, L. Steyn, O. Yaglioglu, S. M. Spearing, M. A. Schmidt, and N. W. Hagood, "A piezoelectric microvalve for compact high-frequency, high-differential pressure hydraulic micropumping systems," *Journal of Microelectromechanical Systems*, vol. 12, pp. 81-92, 2003.

[6] K.-P. Kamper, J. Dopper, W. Ehrfeld, and S. Oberbeck, "A self-filling low-cost membrane micropump," presented at Micro Electro Mechanical Systems, 1998. MEMS 98. Proceedings., The Eleventh Annual International Workshop on, 1998.

[7] K. Handique, D. T. Burke, C. H. Mastrangelo, and M. A. Burns, "On-chip thermopneumatic pressure for discrete drop pumping," *Analytical Chemistry*, vol. 73, pp. 1831-1838, 2001.
[8] P. Selvaganapathy, Y. S. L. Ki, P. Renaud, and C. H. Mastrangelo, "Bubble-free electrokinetic pumping," *Journal of Microelectromechanical Systems*, vol. 11, pp. 448-453, 2002.
[9] Y. Takamura, H. Onoda, H. Inokuchi, S. Adachi, A. Oki, and Y. Horiike, "Low-voltage electroosmosis pump for stand-alone microfluidics devices," *Electrophoresis*, vol. 24, pp. 185-192, 2003.
[10] I. M. Lazar and B. L. Karger, "Multiple open-channel electroosmotic pumping system for microfluidic sample handling," *Analytical Chemistry*, vol. 74, pp. 6259-6268, 2002.
[11] L. X. Chen, J. P. Ma, F. Tan, and Y. F. Guan, "Generating high-pressure sub-microliter flow rate in packed microchannel by electroosmotic force: potential application in microfluidic systems," *Sensors and Actuators B-Chemical*, vol. 88, pp. 260-265, 2003.
[12] D. S. Reichmuth, G. S. Chirica, and B. J. Kirby, "Increasing the performance of high-pressure, high-efficiency electrokinetic micropumps using zwitterionic solute additives," *Sensors and Actuators B-Chemical*, vol. 92, pp. 37-43, 2003.
[13] P. K. Dasgupta and S. Liu, "Electroosmosis - a Reliable Fluid Propulsion System for Flow-Injection Analysis," *Analytical Chemistry*, vol. 66, pp. 1792-1798, 1994.
[14] S. L. Zeng, C. H. Chen, J. C. Mikkelsen, and J. G. Santiago, "Fabrication and characterization of electroosmotic micropumps," *Sensors and Actuators B-Chemical*, vol. 79, pp. 107-114, 2001.
[15] P. H. Paul, D. W. Arnold, and D. Rakestraw, J., "Electrokinetic Generation of High Pressure using Porous Microstructures," presented at Micro Total Analysis Systems (microTAS'98), Banff, Canada, 1998.
[16] J. H. Tsai and L. W. Lin, "A thermal-bubble-actuated micronozzle-diffuser pump," *Journal of Microelectromechanical Systems*, vol. 11, pp. 665-671, 2002.
[17] C. R. Neagu, J. G. E. Gardeniers, M. Elwenspoek, and J. J. Kelly, "An electrochemical microactuator: Principle and first results," *Journal of Microelectromechanical Systems*, vol. 5, pp. 2-9, 1996.
[18] C. G. Cameron and M. S. Freund, "Electrolytic actuators: Alternative, high-performance, material-based devices," *Proceedings of the National Academy of Sciences of the United States of America*, vol. 99, pp. 7827-7831, 2002.
[19] T. Stanczyk, B. Ilic, P. J. Hesketh, and J. G. Boyd, "A microfabricated electrochemical actuator for large displacements," *Journal of Microelectromechanical Systems*, vol. 9, pp. 314-320, 2000.
[20] S. W. Lee, W. Y. Sim, and S. S. Yang, "Fabrication and in vitro test of a microsyringe," *Sensors and Actuators a-Physical*, vol. 83, pp. 17-23, 2000.
[21] S. Bohm, B. Timmer, W. Olthuis, and P. Bergveld, "A closed-loop controlled electrochemically actuated micro-dosing system," *Journal of Micromechanics and Microengineering*, vol. 10, pp. 498-504, 2000.
[22] H. Suzuki and R. Yoneyama, "A reversible electrochemical nanosyringe pump and some considerations to realize low-power consumption," *Sensors and Actuators B-Chemical*, vol. 86, pp. 242-250, 2002.

[23] A. J. Bard and L. R. Faulkner, *Electrochemical methods : fundamentals and applications*, 2nd ed. New York: Wiley, 2001.
[24] C. Neagu, H. Jansen, H. Gardeniers, and M. Elwenspoek, "The electrolysis of water: an actuation principle for MEMS with a big opportunity," *Mechatronics*, vol. 10, pp. 571-581, 2000.
[25] L. Licklider, X. Q. Wang, A. Desai, Y. C. Tai, and T. D. Lee, "A micromachined chip-based electrospray source for mass spectrometry," *Analytical Chemistry*, vol. 72, pp. 367-375, 2000.
[26] V. Meyer, *Practical high-performance liquid chromatography*, 3rd ed. Chichester ; New York: Wiley, 1998.
[27] R. E. Moore, L. Licklider, D. Schumann, and T. D. Lee, "A microscale electrospray interface incorporating a monolithic, poly(styrene-divinylbenzene) support for on-line liquid chromatography tandem mass spectrometry analysis of peptides and proteins," *Analytical Chemistry*, vol. 70, pp. 4879-4884, 1998.
[28] C. H. Chen and J. G. Santiago, "A planar electroosmotic micropump," *Journal of Microelectromechanical Systems*, vol. 11, pp. 672-683, 2002.
[29] J. N. Lee, C. Park, and G. M. Whitesides, "Solvent compatibility of poly(dimethylsiloxane)-based microfluidic devices," *Analytical Chemistry*, vol. 75, pp. 6544-6554, 2003.

.

Chapter 6

Integrated LC-ESI on a Chip

6.1 INTRODUCTION

As shown in Chapter 5, on-chip high pressure pumping and gradient generation using electrochemical actuation was successfully demonstrated. The pumps could also be integrated with an ESI nozzle using the same fabrication process, and then the next task will be to integrate the pump and nozzle with an on-chip column so a complete LC-ESI system can be realized on chip. The fabrication process in Chapter 5 is so flexible and versatile that only a few small modifications are needed to incorporate a column on the chip.

Main motivations behind the total integration and miniaturization of LC-ESI on a chip can be found in Chapter 1. Some specific reasons are listed here. First, total integration eliminates cumbersome interconnections between discreet components as currently practiced in analytical laboratories. Dead volume inside the LC-ESI chip can almost be ignored because of close vicinity of those components and micro channels that are used for the interconnections. Time for analytes or solvents passing through those connection channels is also greatly reduced which can leads to fast analysis. The integration with on-chip nano-flow pumps means no splitting is required, and during

operation, the chip doesn't need any fluid or pneumatic connection to the outside world. The operation of the chip is electrically controlled by circuits and computer, and automation becomes much simpler and straightforward. Of course, microfabrication also opens up the possibilities of mass production which is the key to low cost.

6.2 DESIGN AND ANALYSIS

6.2.1 LC-ESI Chip

Figure 6-1 shows the schematic diagram of the LC-ESI chip. All the essential components of a LC-ESI system are integrated into chip format. These components include: solvent gradient pumps, a passive mixer, a sample injector, a reversed-phase (RP) column and an ESI nozzle. Except for solvent and sample reservoirs, all these components are integrated onto a single silicon chip.

6.2.2 Gradient Pump and Sample Injector

Gradient elution, mixture of aqueous (polar) and organic (non-polar) solvents, is usually used in reversed-phase chromatography. In most cases, elution starts at high aqueous

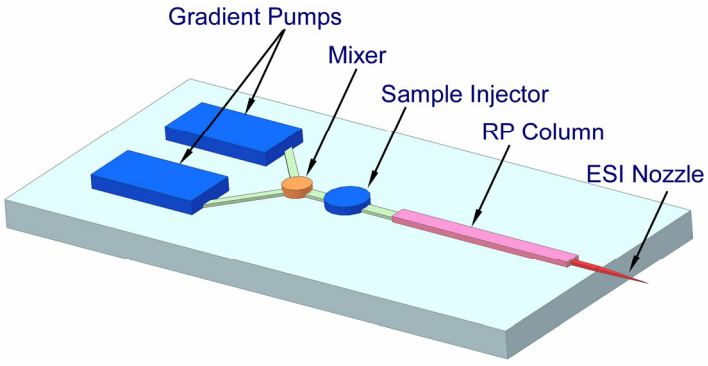

Figure 6-1 All the essential components of a LC-ESI chip are integrated on a chip.

concentration and gradually changes to high organic concentration.

A typical nano-LC binary solvent gradient has a total flow rate of 100 nL/min and a duration of 10s minutes to several hours. A typical sample injection also requires a sample volume around 1 μL. Besides the gradient elution, the pumps must be able to perform other functions, such as rinsing. To realize all these functions, a total solvent volume larger than 10 μL is necessary. This volume constraint prevents the solvent and sample reservoirs to be integrated into a single silicon chip. To accommodate such a volume, the reservoirs are mainly built into a separate reservoir chip (500 μm thick silicon). On each side of the reservoir chip, a 300 μm PDMS is used as gasket. The area of each reservoir on the chip surface will be 1 mm wide and 10 mm long. After packaging, the height of the reservoirs is expected to be 1 mm. Thus, it is possible to build two 10 μL solvent reservoirs and one 3.5 μL sample injector on a 1 cm × 2 cm chip and still leave room for other components. Details of the fabrication are presented later in the fabrication section.

For the electrodes design, the same interdigitated configuration as that in Chapter 5 is chosen. The main reason for this is to reduce the bulk resistance and undesired joule heating of the fluid, which decreases pumping efficiency. The total length of the interdigitated electrodes and the length of each finger are 5 mm and 1 mm respectively. The spacing between fingers and the width of each finger are both 50 μm.

Even at high organic solvent concentration, the bulk resistance is estimated to be less than 10 kΩ. That means voltage drop on the electrodes is less than 10 V for 1 mA current. These values can be easily handled by common IC circuit with a power supply less than 15 V.

The other purpose of the interdigitated electrode design is to enhance the recombination since H_2 and O_2 gases are not separated. A binary solvent gradient requires one of the solvents pumping rate to decrease while the other increases. Besides the gas permeation and the liquid pumping itself, there is no other way to bleed the pressure inside the pumping chamber. The enhanced recombination can speed up the pressure releasing while compromising the electrolysis efficiency.

6.2.3 Passive Mixer

Solvents in the gradient elution need to be well mixed together before entering the separation column to avoid causing any negative effect on the chromatography. Due the laminar flow in the microfluidic devices, mixing is mostly done by diffusion. The passive mixer here is basically a mixing channel. To enhance mixing, the diffusion length needs to be reduced. A channel with a 20 μm × 20 μm cross section is used as passive mixer. Diffusion constant D of small molecules in water is on the order of 10^{-9} m^2/s. Time needed for mixing t_{mix} is approximately $t_{mix} = L_{diff}^2 / D$. L_{diff} is the diffusion length which is 20 μm. t_{mix} is estimated to be around 0.4 s. For a flow rate of 100 nL/min, the flow velocity in the mixing channel is about 5 mm/s. Then the length of the mixing channel has to be at least 2 mm. The sweep volume of the mixer is 0.8 nL.

6.2.4 Reversed-phase Column

Solid phase in the reversed-phase separation column is C_{18}-coated 5 μm fused silica beads with a pore size of 30 nm. The beads were purchased from Vydac. Commercial nano-LC capillary column is available in diameters < 100 μm with an optimal flow velocity around 1 mm/s. In the chip, column is chosen to have a cross section of 20 μm (H) × 100 μm (W) whose area is equivalent to a 50 μm I.D. capillary. Then the optimal

flow rate for separation is around 100 nL/min. As proof of concept, the column length is reduced to 10 mm compared to the typical 50 to 250 mm. Thus, the separation can be performed under relatively low pressure which is around 3 bar.

6.2.5 ESI nozzle

The ESI nozzle is very similar to the one that was previous demonstrated by our group. Overhanging distance of the nozzle is about 1 mm. The tip orifice is about 5 μm high and 20 μm wide, and the curvature of the very end is about 1-2 μm. The channels that connect both pumping chambers and the nozzle are 5 μm high and 100 μm wide. Structural materials for the ESI nozzle are two parylene layers. An integrated platinum electrode is located in the nozzle channel to provide electrical contact for electrospray.

6.3 FABRICATION

6.3.1 Chip Design and Packaging

The schematic diagram of the chip design and packaging is shown in Figure 6-2. There are three main components. First, an ESI nozzle, a column, a mixer, a sample injector, and gradient pumps (electrodes) are integrated onto a main chip which is a silicon substrate. On top of the main chip is a solvent and sample reservoir chip which is a

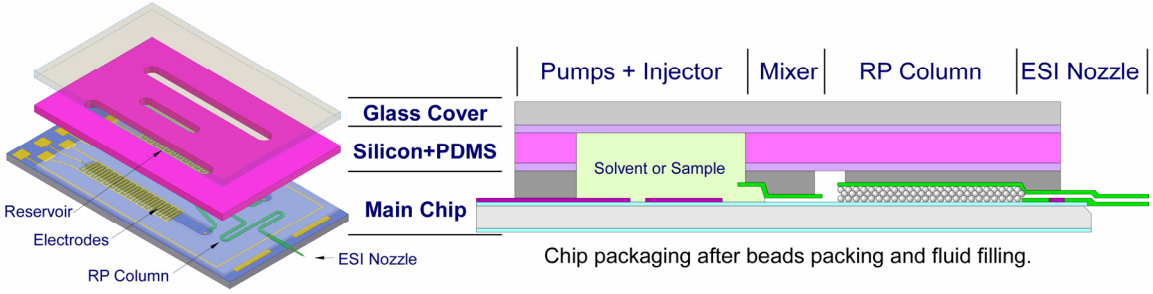

Figure 6-2 LC-ESI chip design and packaging.

silicon substrate bonded with PDMS gaskets. On the main chip, top surface is planarized using a thick 50 µm SU-8 layer which creates a flat surface for the reservoir chip to sit on. To use the chip, the reservoir chip is placed on the SU-8 planarized main chip. The adhesion between the PDMS and the SU-8 or silicon is adequate for filling the chambers with solvent using a syringe. Once the solvent chambers are filled, the two chips are clamped down using the glass cover to ensure the solvent and sample reservoirs are sealed. Clamping force and electrical connection to the chip are provided by a custom-made jig.

6.3.2 Fabrication Process

The detail fabrication process is shown in Figure 6-3. The process began with a 4-inch silicon wafer with 1.5 µm of thermally grown oxide. Electrolysis electrodes were made of E-beam evaporated platinum/titanium (200 nm/30 nm). Heated (~80°C) Aqua Regia (HNO_3:HCl=1:6) was used for Pt/Ti etching. After patterning the electrodes, the front side oxide was patterned using buffered HF. Before first parylene deposition (4.5 µm) , adhesion promoter (A-174 from Specialty Coating Systems) was applied to the substrate.

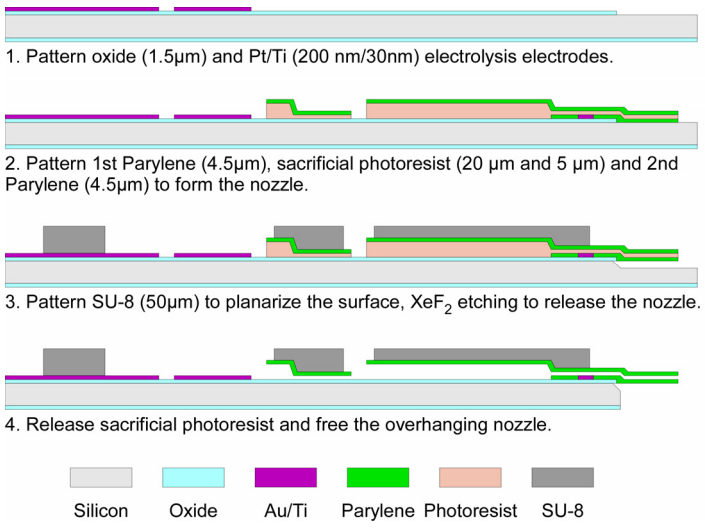

Figure 6-3 The fabrication process of the main chip.

Then 20 µm sacrificial photoresist was spun on the wafer to define fluid channels. A partial exposure was performed to reduce the height of the channels in the mixer and nozzle regions. These regions also serve as filter structures to prevent beads flowing through. Second parylene layer (4.5 µm) was deposited and pattern to form channel ceiling. In order to promote adhesion between the silicon substrate and the second parylene layer, short XeF_2 dry etching was performed to roughen the exposed silicon surface. A 150 nm sputtered aluminum layer was used as a mask for parylene etching to define the shape of the nozzle. The Al was later removed by wet etching.

Wafers then went through a 5% HF dip and oxygen plasma cleaning before a 50 µm SU-8 layer was spin-coated on. The SU-8 layer was patterned and served to provide a flat overall chip surface to support the reservoir chip. After SU-8 developing, wafers were left inside the SU-8 developer (propylene glycol monoether acetate, PGMEA) to release the photoresist. After the photoresist had been dissolved, an 80 µm deep anisotropic XeF_2 etching was used to undercut the nozzle and make it freestanding. Wafers were then diced into 1 × 2 cm chips. A photomicrograph of the fabricated device is shown in Figure 6-4.

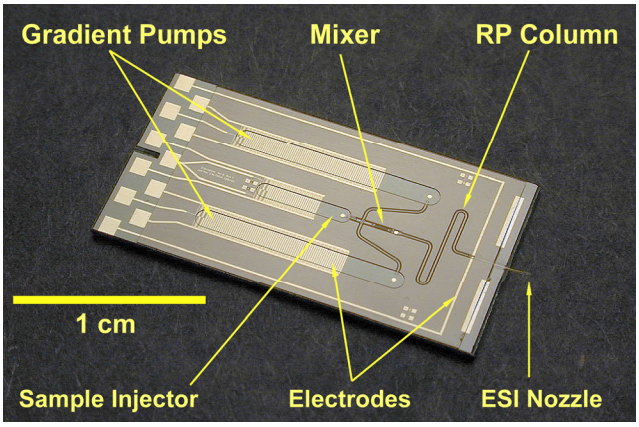

Figure 6-4 The photograph of the fabricated main chip

The reservoir chip was fabricated by using DRIE to etch through a 500 μm thick silicon wafer. 300 μm PDMS gaskets were formed by spinning it on a silicon wafer, and then peel them off after curing. The PDMS gaskets were bonded to both sides of the reservoir chip. The bottom PDMS gasket was cut to the shape of the reservoir chip.

Au, Ti and Al metals were purchased from Williams Advanced Materials (Brewster, NY). Au and Al etchants and buffered HF were purchased from Transene Inc. (Danvers, MA). All photoresist materials were purchased from Clariant (Somerville, NJ). SU-8 was manufactured by Microchem (Newton, MA). Parylene was provided by Uniglobe Kisco (San Jose, CA). XeF_2 was purchased from Pelchem (Pretoria, South Africa). PDMS was Sylgard® 184 from Dow Corning (Midland, MI).

6.4 Experimental Results

6.4.1 Testing Setup

Solvents and samples are pre-injected into the reservoirs before testing. Filling/venting ports located at either end of the solvent and sample reservoirs were punched through the PDMS gasket. Stainless steel syringe needles from Hamilton Co. (Reno, NV) were inserted through the holes in the PDMS layer and fluid was injected into the reservoirs.

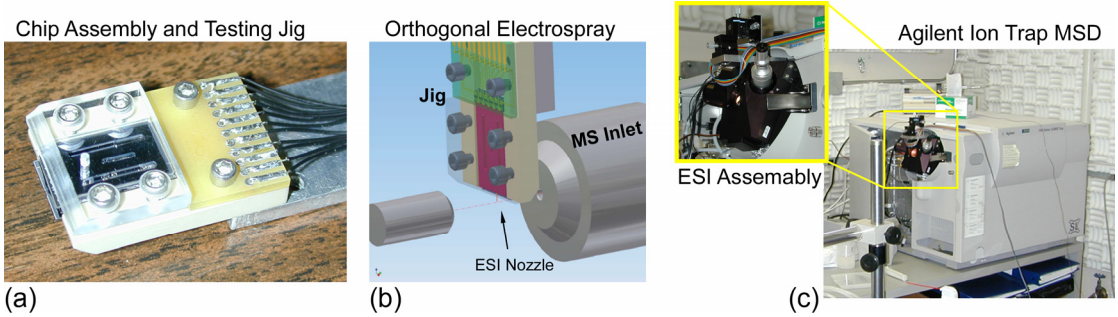

Figure 6-5 LC-ESI chip testing setup. (a) Assembled chip in the testing jig. (b) Orthogonal electrospray configuration. (c) Testing jig was mounted inside ESI assembly of Agilent Ion Trap MSD.

The gas venting holes at the opposite end of the reservoirs ensured complete filling. After filling, a glass cover was placed and clamped on top of the reservoir chip to seal the reservoirs. Elastomeric connector from ARC-USA (Grand Prairie, TX) was used to provide robust electrical connection to chip. This method is more convenient than wire bonding since bonding wire can be damaged easily during handling of the chips, while at the same time, requires much less space than probes. Limitations of elastomeric connector are higher contact resistance and low current capacity (~1 mA/m^2). However, for the most experiments, it is sufficient.

The three chips were manually aligned and placed in a custom-made jig shown in Figure 6-5(a). Orthogonal electrospray configuration used in Agilent Ion Trap MSD, shown in Figure 6-5(b) was adopted. The ESI assembly come with the MSD, shown in Figure 6-5(c), was modified to accommodate the testing jig.

Electrolysis pumps were galvanostatically controlled using output currents from custom-built voltage to current converters. Full-scale current range was normally 1 mA and it was adjustable. The voltages were programmed in LabView and were fed to the converters through a DAQPad-6020E interface board from National Instruments (Austin, TX).

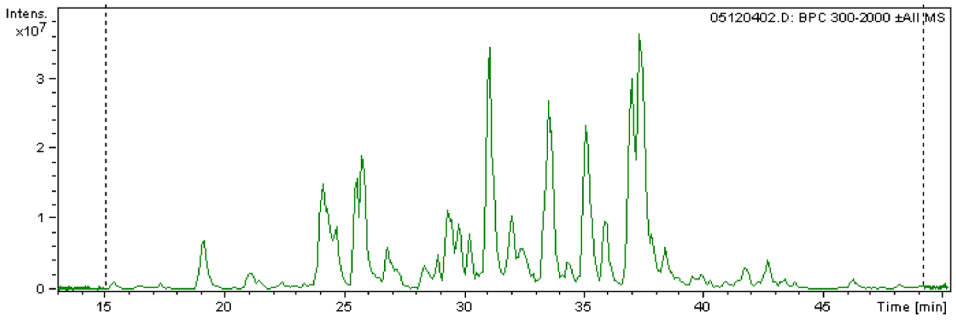

Figure 6-6 A typical peptide separation done by Agilent 1100 LC-MS system.

6.4.2 Commercial LC-MS System

As a comparison for the chip performance, a typical peptide separation was performed using a commercial system. Sample was 1 pmol/μL peptide mixture from tryptic digested bovine serum albumin (BSA). Gradient elution was provided by Agilent 1100 LC pumps. Column used was a 75 μm I.D. and 15 cm long capillary. Packing material in the RP column was 3.5 μm Agilent Zorbax 300 SB-C_{18} beads. Aqueous solvent was (water/acetonitrile/formic acid, 95/5/0.1 by volume) and organic solvent was (water/acetonitrile/formic acid, 40/60/0.1 by volume). During the separation, a 500 nL sample (500 fmol) was injected and flow rate was set to be 100 nL/min with gradient change from 100% aqueous to 100% organic. Total separation took 55 min and the result is shown in Figure 6-6.

6.4.3 Chip Performance

Similar separation was performed using the LC-ESI chip. The sample used here is the

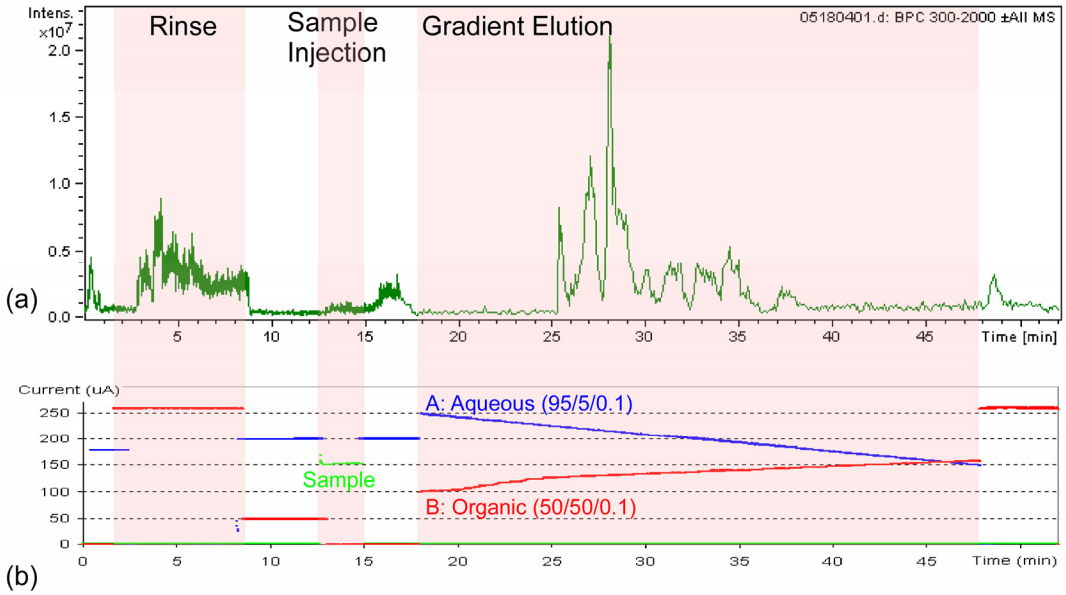

Figure 6-7 A peptide separation done by the LC-ESI chip. (a) Chromatography. (b) Control current profile.

same as in the capillary case. Packing material used was 5 µm Vydac C_{18} beads. The 1 cm on-chip column has a cross section equivalent to a 50 µm I.D. capillary. The aqueous solvent was (water/acetonitrile/formic acid, 95/5/0.1 by volume) and organic solvent was (water/acetonitrile/formic acid, 50/50/0.1 by volume).

The result is shown in Figure 6-7. First, the organic solvent pump was turned on to rinse the column. Then the aqueous solvent was pumped through to regenerate the column. The injected sample volume was 500 nL (about 500 fmol sample). The gradient changed from 100% A to 100 % B and lasted about 30 min with an estimated flow rate of 100 nL/min. The control current profile that was applied to the electrolysis pumps was also given in Figure 6-7(b).

6.4.4 Comparison

Figure 6-8 compares the separation done by the commercial system and the chip. In Figure 6-8, 9 ions are extracted and listed for both experiments. Except for ion No. 3 and

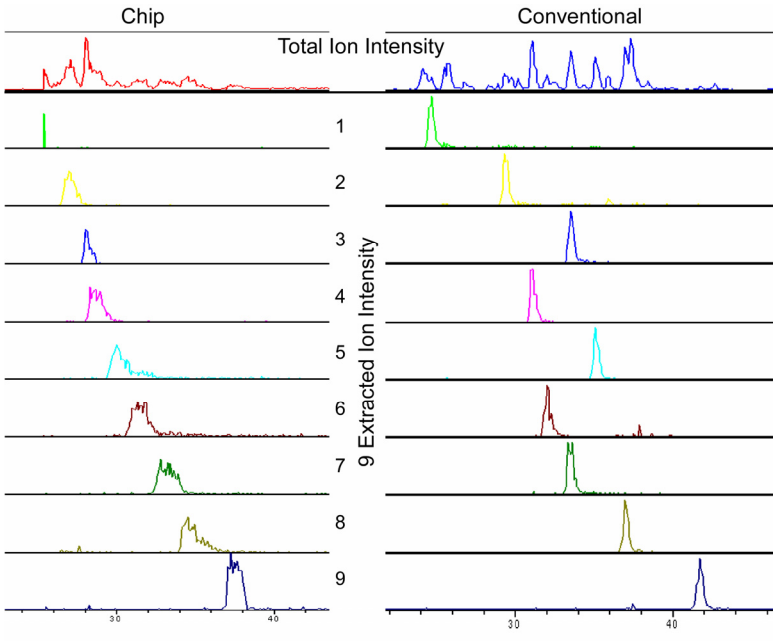

Figure 6-8 Separation comparison between the commercial system and the LC-ESI chip.

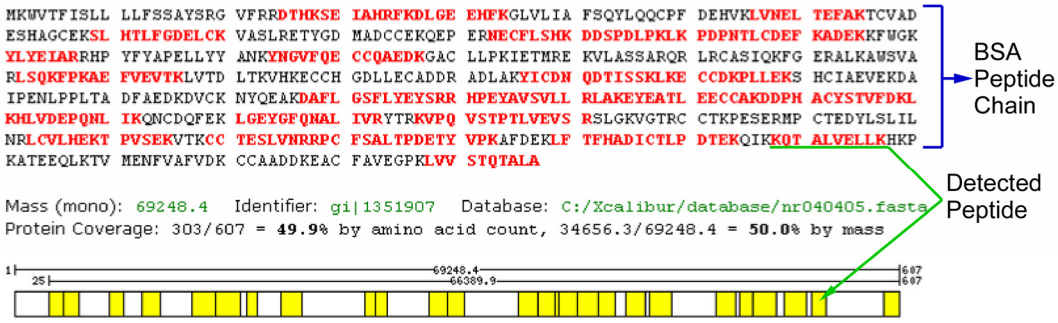

Figure 6-9 Peptide coverage from the database search in the separation done by the chip.

5, the elution orders and times are very similar for both cases. The difference in ion No.3 and 5 could caused by the relatively high temperature of the chip due to its close placement to the heated MS inlet. Based on the MS data, a database search was carried out to identify peptides associated with those ion signals. The result for the chip is listed in Figure 6-9. The peptide coverage of the experiments done by the chip was 50 % which is comparable to the 60 % achieved by the Agilent 1100 LC-MS system.

6.4.5 Other Chip Testing

Other types of experiments were tested on the chip. For example, multiple separations with re-filling the reservoirs were demonstrated. Other types of organic solvents, such as methanol, were also tested. Usually, the chip can be reused several times by rinse it carefully after experiments.

6.5 CONCLUSIONS

A complete LC-ESI system was integrated in a chip format. Typical nano-LC reversed-phase gradient elution was demonstrated using on-chip electrolysis pump. Separated analytes from on-chip column were then sprayed into MS for analysis through an integrated ESI-nozzle. Separation results are comparable to those of commercial system.

Peptide identification performance using the LC-ESI chip with MS was also very close to those achieved by the commercial system.